2019

Investigation of the photophysical properties of energy-relevant inorganic nanocrystals

Brett Boote
Iowa State University

Investigation of the photophysical properties of energy-relevant inorganic nanocrystals

by

Brett William Boote

A dissertation submitted to the graduate faculty

in partial fulfillment of the requirements for the degree of

DOCTOR OF PHILOSOPHY

Major: Chemistry

Program of Study Committee:
Emily A. Smith, Major Professor
Jacob W. Petrich
Javier Vela-Becerra
Jared D. Anderson
Aaron J. Rossini

The student author, whose presentation of the scholarship herein was approved by the program of study committee, is solely responsible for the content of this dissertation. The Graduate College will ensure this dissertation is globally accessible and will not permit alterations after a degree is conferred.

Iowa State University

Ames, Iowa

2019

DEDICATION

This dissertation is dedicated to my wife, Emily, and my sons John and Maxwell, who give me such pride and joy that it makes all the hours worthwhile. Thank you for the support, love, and understanding through these 5 years. Emily, thank you for the support and patience while I have gone to school for essentially the last 9 years.

John, who aspires to be a scientist (for now), thanks for all the fruitful discussions about music and video games and your enthusiasm for nearly everything I enjoy.

Maxwell, whose vocabulary is exponentially increasing, thanks for the hugs and waves when I get home every day, and for reading *Curious George* with me before bed.

You are all the best.

TABLE OF CONTENTS

Page

ACKNOWLEDGEMENTS v

ABSTRACT vii

CHAPTER 1. GENERAL INTRODUCTION – ENERGY-RELEVANT INORGANIC NANOCRYSTALS 1
Thesis Organization 5
References 6

CHAPTER 2. GERMANIUM–TIN/CADMIUM SULFIDE CORE/SHELL NANOCRYSTALS WITH ENHANCED NEAR-INFRARED PHOTOLUMINESCENCE 10
Abstract 10
Introduction 11
Experimental Section 16
Materials. 16
Preparation of Ge and $Ge_{1-x}Sn_x$ (core) nanocrystals. 16
Preparation of Ge/CdS and $Ge_{1-x}Sn_x$/CdS (core/shell) nanocrystals. 17
Optical Characterization. 18
Results and Discussion 20
Synthesis and Characterization of $Ge_{1-x}Sn_x$ Core Nanocrystals. 20
Synthesis and Characterization of $Ge_{1-x}Sn_x$/CdS Core/Shell Nanocrystals. 25
X-Ray Photoelectron Spectroscopy of Ge/CdS and $Ge_{1-x}Sn_x$/CdS Core/Shell Nanocrystals. 28
Luminescence Properties of $Ge_{1-x}Sn_x$ Core and $Ge_{1-x}Sn_x$/CdS Core/Shell Nanocrystals. 31
Conclusion 34
Acknowledgements 35
References 35
Supplemental Information 43

CHAPTER 3. UNVEILING THE PHOTO- AND THERMAL-STABILITY OF CESIUM LEAD HALIDE PEROVSKITE NANOCRYSTALS 51
Abstract 51
Introduction 52
Results and Discussion 55
General Characterization and Photophysical Properties of $CsPbX_3$ Nanocrystals 56
Photostability of $CsPbX_3$ Nanocrystals 60
Thermal Stability of $CsPbX_3$ Nanocrystals 63
Conclusions 67
Experimental Section 68
Materials 68

Preparation of the Nanocrystals 68
Optical Characterization 69
Photostability Study 70
Thermal Stability Study 70
Acknowledgements 71
References 71
Supplemental Information 79

CHAPTER 4. SUBDIFFRACTION MICROSCOPY BY SATURATED LUMINESCENCE OF INORGANIC QUANTUM DOTS 88
Abstract 88
Introduction 89
Experimental Section 90
Materials 90
Saturated Luminescence Instrumentation 91
Sample Preparation 92
Results and Discussion 92
Conclusions 98
Acknowledgements 99
References 99

CHAPTER 5. GENERAL CONCLUSION 102

ACKNOWLEDGEMENTS

I would like to thank my major professor, Dr. Emily Smith, for her guidance, insights, professionalism, commitment to detail, and understanding the time commitments which come with a family of four. Thank you for all the support and helpful discussions.

I would also like to thank Dr. Jacob Petrich and Dr. Javier Vela for the many collaborations as part of the Chemical Analysis of Nanodomains team and beyond, and for supporting my research goals. My thanks to Dr. Jared Anderson, Dr. Keith Woo, Dr. Aaron Rossini for serving on my PhD committee and helpful insights along the way. A special thanks also goes to Dr. Matt Panthani for serving as a substitute for my final oral defense.

I would also like to thank the many student collaborators I have worked closely with over the years, including Dr. Bryan Rosales, Dr. Long Men, Dr. Himashi Andaraarachchi, Dr. Ujjal Bhattacharjee, and Dr. Kalyan Santra. I learned from each one of you in your fields of expertise.

I would also like to thank my Smith group lab mates for their camaraderie and support through all the office discussions, group meetings, and Slack conversations. A special thanks to previous members Dr. Aleem Syed, Dr. Jonathan Bobbitt, and Daniel Freppon for showing me the ropes and for their friendship during our time at Iowa State. My thanks to Jingzhe Li for her help with my projects as well, and for keeping the materials research going in the Smith Group. Lastly thanks to Dr. Avinash Singh—as a team we were able to decipher the code of saturated excitation and put it to use in our

respective fields. You helped me as much or more than I helped you through these 2 years.

I would also like to thank the US Department of Energy through Ames Laboratory for supporting this research through funding.

ABSTRACT

Environmental concerns over use of fossil fuels to generate power and the finite supply of these resources have driven major efforts for alternative energies. At the same time, the development of nanotechnology has blossomed to propose strategies and materials for renewable and less energy-intensive end-user devices, such as solar cells and LED lighting. Two examples of promising candidates for energy applications are germanium-based nanocrystals and lead halide perovskite nanocrystals.

Germanium-based materials have limited absorption efficiency due to their indirect band gap. To address this, germanium-tin alloy nanocrystals were synthesized to promote direct band gap character. A full characterization demonstrated tin incorporation, but a direct band gap was not observed. Addition of a cadmium sulfide shell typically results in improved photoluminescence, and the incorporation of tin into germanium-tin/cadmium sulfide core/shell nanocrystals resulted in up to 15× improvement over pure germanium/cadmium sulfide nanocrystals. This is likely due to improved epitaxy (smaller lattice mismatch) between the core and shell material.

Lead halide perovskite nanocrystals have demonstrated amazing potential for solar energy capture but are hampered by stability concerns. All-inorganic cesium lead halide perovskite nanocrystals have been prepared to impede the typical degradation pathways (ambient moisture and oxygen). To assess nanocrystal stability the photophysics of cesium lead halide nanocrystals were measured as a function of halide content under ambient conditions, solar simulated light, and heating. We observed several phenomena including crystal growth (liberation of ligands), photoannealing, crystalline phase changes, and shifting time constants for single crystal photoluminescence data. All

of these observations lead to a more realistic picture of the stability of these nanocrystals, which will still likely require encapsulation or surface protection to be effective in long-term device use.

In addition to materials synthesis and characterization, new instrumental techniques are critical for the next generation of energy capture and storage solutions. To this end we constructed a saturated excitation microscope in order to measure the photoluminescence of inorganic semiconductor quantum dots, capable of subdiffraction imaging through demodulation at harmonics (nf, n = 2, 3, etc) of the excitation modulation frequency (f). By demodulating at 3f, a 36% increase in resolution was observed compared to the fundamental image, which will be useful characterizing thin films, nancrystals, and other devices where small defects can have large impacts on performance.

CHAPTER 1. GENERAL INTRODUCTION – ENERGY-RELEVANT INORGANIC NANOCRYSTALS

The field of nanotechnology has redefined or directly led to the development of several new fields in the landscape of renewable or sustainable energy, most notably in photovoltaics for solar energy capture and optoelectronics for lighting applications.[1] Major research avenues in nanoscience revolve around three main areas: synthesis of new materials or improved syntheses of existing materials, characterizations of unique properties of these materials due to their nanoscale dimensions, and development of applications for these materials in industry or society. The research contained in this volume primarily revolves around nanocrystal characterization, where the unique properties of the materials studied are measured via several complementary instrumental methods. To understand the utility of fundamental research on the photophysical characteristics of nanocrystals, discussion of nanocrystal-derived devices as well as microscopy techniques that rely on nanocrystals will be given.

In materials science, the number of possible materials to study is nearly limitless; even when limited to nanomaterials related to sustainable energy there are dozens of materials related to solar energy, hydrogen generation, and advanced batteries.[1] The vast majority of photovoltaic devices in use today are silicon-based, but emerging nanomaterials show great promise due to their strong absorption combined with tunable emission.[2] One class of nanomaterials of particular interest are lead halide perovskites due to suitable band gap, high luminescence quantum yield, and solution processability. At the core of the photovoltaic cell is the absorber layer, responsible for light collection and electron generation, and thus the composition of the absorber layer determines the overall

photon conversion efficiency (PCE) of the device. Though many nanomaterials have been studied as potential silicon replacements, none have received as much attention over the last 10 years as lead halide perovskites, most notably due to their meteoric rise in PCE (from ~4% to over 20%).[3] The perovskite structure has the general formula ABX_3, where A and B are two cations of differing sizes which both bond to the anion X. Since the demonstration of lead-based perovskites (methylammonium lead bromide, $CH_3NH_3PbBr_3$) as solar cell sensitizers in 2006,[4] this crystal structure has been adapted to myriad different combinations of cations and metal centers with goals ranging from increased stability towards oxygen and moisture to reduced toxicity.[5-6] The current record PCE of a cesium lead halide perovskite-based solar cell is 13.4%, achieved through surface treatment by AX salts in the functional device absorber layer.[7] Other studies show increased stability through addition of tri-octylphosphine to the perovskite layer while still maintaining an 11.2% PCE.[8]

Germanium-based nanomaterials have also garnered attention as less toxic alternatives to more conventional luminescent semiconductors, such as cadmium dichalcogenides, in applications such as photovoltaic cells, photodetectors, as well as biological imaging.[9] Germanium, like silicon, exhibits an indirect band gap that limits light absorption and thus luminescence quantum yield. Still, previous work showed the potential for tin doping to create a more direct band gap through strain.[10] The work described in Chapter 2 sought to understand the effect of tin doping on the luminescence properties of germanium nanocrystals.

A tremendous number of studies have been published regarding the synthesis, photophysical properties, and functional devices of lead halide-based perovskite materials,

including considerable work on the nanocrystalline form.[2, 5, 8, 11-22] Many studies focused on derived devices that can be constructed using the perovskite nanocrystals as the absorber layer, but our approach was to gain fundamental information about the photophysics of these light-harvesting materials. The work described in Chapter 3 sought to understand the photophysics and stability of cesium lead halide perovskite nanocrystals as a function of halide composition.

Microscopy techniques are critical to the study of materials for use in energy-related applications. However, conventional optical methods are inherently restricted spatially by Abbe's diffraction limit, $d \approx \frac{\lambda}{2NA}$. That is, the smallest area that can be probed by a given measurement is on the order of hundreds of nanometers, even using high numerical aperture objectives. Much work has been done to circumvent the diffraction limit to allow for more precise localization of unique properties such as fluorescent tags or quantum dots in biological systems.[23-34] Most of these techniques rely on one of two strategies: spatial or temporal modulation of the excitation light or localization of photo-activated fluorophores. In addition, there are several reports that highlight the importance of nanocrystals or quantum dots in microscopy techniques.

Many single particle tracking strategies rely on bright, stable photoluminescence of quantum dots to visualize movement of biomolecules in dynamic systems.[35] The quantum dots are typically labeled with antibodies specific to the target biomolecule in order to maximize binding affinity and reduce non-specific binding. Ma *et al*. were able to recently target single gene loci in the nuclei of cells via colocalization of two different quantum dot transcription activator-like effector (TALE) conjugates.[36] Single gene loci are typically related to genetic disease or pathogen infection. The two distinct TALE sequences bind to

either side of a target gene and the two distinct quantum dots appear in the same location in images, indicating the single gene locus. Gonda and coworkers sought to diagnose risk of recurrence of breast cancer by quantum dot imaging of patient tissues with their developed anti-protease-activated receptor1 (anti-PAR1) antibodies which specifically bind to cancerous tissue.[37] They also developed an autofluorescence subtraction method using several bandpass filters in order to better visualize signal from quantum dots and eliminate high autofluorescence false-positives. An *in vivo* study by Han *et al*. showed quantum dot-antibody conjugates allow for imaging of rare endogenous cells in live mice.[38] Especially for *in vivo* studies, the bright and stable photoluminescence of quantum dots paired with simple conjugation of several classes of antibodies make them excellent candidates for long term studies.

Although less common than localization-based subdiffraction imaging, another approach to subdiffraction imaging is saturated excitation microscopy, popularized and demonstrated by Katsumasa Fujita.[33, 39-42] Initial concepts for subdiffraction imaging combined structured illumination with saturated excitation,[43-44] but Fujita showed saturation was sufficient for modest resolution gains. This technique involves saturation of the excited state via high laser powers and modulation (at the frequency *f*) of the excitation source. The high laser power induces nonlinearity in the fluorescence signal, which generates signal at overtone frequencies (*2f, 3f, etc.*) that can be demodulated. The benefit is the signal from the overtone frequencies comes from the centermost portion of the diffraction limited spot, and thus subdiffraction information can be collected. The extent of the resolution improvement is proportional to the degree of saturation, which is correlated to laser power and other properties. Practical limitations in the attainable

resolution are the decreasing signal-to-noise ratio (SNR) of higher harmonic overtones and photodamage to the sample, but current systems have shown ~140 nm resolution using fluorescent nanodiamond.[41] In Chapter 4, ideas from saturated excitation are combined with photoluminescence from inorganic semiconductor quantum dots. An instrument was constructed that allowed for the modulation of the excitation laser, rastering of the sample across the objective for image collection, as well as demodulation of the luminescence signal. The degree of resolution improvement in saturated luminescence images collected at harmonics compared to the fundamental frequency is quantified, as well as other observations on the broad distribution of resolution gains on a single quantum dot basis.

Thesis Organization

This thesis is composed of two parts: in part 1 (Chapters 2 and 3) I describe efforts to characterize nanomaterials with downstream applications in photovoltaic or related devices, while in part 2 (Chapter 4) I demonstrate a subdiffraction microscope based on frequency-modulated quantum dot luminescence.

In Chapter 2, we investigate the effect of tin doping into germanium nanocrystals in an effort to improve photoluminescence quantum yield through band gap tuning. In Chapter 3, the photo- and thermal stability of cesium lead halide perovskite nanocrystals in ambient conditions is reported. Chapter 4 describes the development of a saturated excitation microscope capable of subdiffraction information from the photoluminescence of inorganic nanocrystal quantum dots. The data presented in Chapters 2 and 3 were collected in collaboration with the Vela and Petrich groups, Department of Chemistry, Iowa State University, while Chapter 4 was a collaboration with the Petrich group.

References

1. Serrano, E.; Rus, G.; Garcia-Martinez, J., Nanotechnology for sustainable energy. *Renewable and Sustainable Energy Reviews* **2009,** *13* (9), 2373-2384.

2. Protesescu, L.; Yakunin, S.; Bodnarchuk, M. I.; Krieg, F.; Caputo, R.; Hendon, C. H.; Yang, R. X.; Walsh, A.; Kovalenko, M. V., Nanocrystals of Cesium Lead Halide Perovskites ($CsPbX_3$, X= Cl, Br, and I): Novel Optoelectronic Materials Showing Bright Emission with Wide Color Gamut. *Nano Letters* **2015,** *15* (6), 3692-3696.

3. Berry, J.; Buonassisi, T.; Egger, D. A.; Hodes, G.; Kronik, L.; Loo, Y. L.; Lubomirsky, I.; Marder, S. R.; Mastai, Y.; Miller, J. S., Hybrid organic–inorganic perovskites (HOIPs): Opportunities and challenges. *Advanced Materials* **2015,** *27* (35), 5102-5112.

4. Kojima, A.; Teshima, K.; Miyasaka, T.; Shirai, Y., Novel photoelectrochemical cell with mesoscopic electrodes sensitized by lead-halide compounds. *Proc. 210th ECS Meeting (ECS, 2006)* **2006**.

5. Akkerman, Q. A.; Rainò, G.; Kovalenko, M. V.; Manna, L., Genesis, Challenges and Opportunities for Colloidal Lead Halide Perovskite Nanocrystals. *Nature Materials* **2018,** *17*, 394-405.

6. Tai, Q.; Kai-Chi, T.; Yan, F., Recent Progress of Inorganic Perovskite Solar Cells. *Energy & Environmental Science* **2019**.

7. Sanehira, E. M.; Marshall, A. R.; Christians, J. A.; Harvey, S. P.; Ciesielski, P. N.; Wheeler, L. M.; Schulz, P.; Lin, L. Y.; Beard, M. C.; Luther, J. M., Enhanced Mobility $CsPbI_3$ Quantum Dot Arrays for Record-Efficiency, High-Voltage Photovoltaic Cells. *Science Advances* **2017,** *3* (10), eaao4204.

8. Lu, C.; Li, H.; Kolodziejski, K.; Dun, C.; Huang, W.; Carroll, D.; Geyer, S. M., Enhanced stabilization of inorganic cesium lead triiodide (CsPbI 3) perovskite quantum dots with tri-octylphosphine. *Nano Research* **2018,** *11* (2), 762-768.

9. Vaughn, D. D., II; Schaak, R. E., Synthesis, Properties and Applications of Colloidal Germanium and Germanium-Based Nanomaterial. *Chem. Soc. Rev.* **2013,** *42* (7), 2861–2879.

10. Ramasamy, K.; Kotula, P. G.; Fidler, A. F.; Brumbach, M. T.; Pietryga, J. M.; Ivanov, S. A., Sn_xGe_{1-x} Alloy Nanocrystals: A First Step toward Solution-Processed Group IV Photovoltaics. *Chem. Mater.* **2015,** *27* (13), 4640–4649.

11. Bekenstein, Y.; Koscher, B. A.; Eaton, S. W.; Yang, P.; Alivisatos, A. P., Highly Luminescent Colloidal Nanoplates of Perovskite Cesium Lead Halide and Their Oriented Assemblies. *J Am Chem Soc* **2015,** *137* (51), 16008-11.

12. Bi, C.; Wang, S.; Li, Q.; Kershaw, S. V.; Tian, J.; Rogach, A. L., Thermally Stable Copper (II) Doped Cesium Lead Halide Perovskite Quantum Dots with a Strong Blue Emission. *The journal of physical chemistry letters* **2019**.

13. Chen, Y.-C.; Chou, H.-L.; Lin, J.-C.; Lee, Y.-C.; Pao, C.-W.; Chen, J.-L.; Chang, C.-C.; Chi, R.-Y.; Kuo, T.-R.; Lu, C.-W., Enhanced Luminescence and Stability of Cesium Lead Halide Perovskite CsPbX3 Nanocrystals by Cu2+-Assisted Anion Exchange Reactions. *The Journal of Physical Chemistry C* **2019,** *123* (4), 2353-2360.

14. Dong, Y.; Qiao, T.; Kim, D.; Parobek, D.; Rossi, D.; Son, D. H., Precise control of quantum confinement in cesium lead halide perovskite quantum dots via thermodynamic equilibrium. *Nano letters* **2018,** *18* (6), 3716-3722.

15. Marronnier, A.; Roma, G.; Boyer-Richard, S.; Pedesseau, L.; Jancu, J.-M.; Bonnassieux, Y.; Katan, C.; Stoumpos, C. C.; Kanatzidis, M. G.; Even, J., Anharmonicity and disorder in the black phases of cesium lead iodide used for stable inorganic perovskite solar cells. *ACS nano* **2018,** *12* (4), 3477-3486.

16. Mir, W. J.; Jagadeeswararao, M.; Das, S.; Nag, A., Colloidal Mn-doped Cesium Lead Halide Perovskite Nanoplatelets. *ACS Energy Letters* **2017,** *2* (3), 537-543.

17. Rainò, G.; Nedelcu, G.; Protesescu, L.; Bodnarchuk, M. I.; Kovalenko, M. V.; Mahrt, R. F.; Stöferle, T., Single Cesium Lead Halide Perovskite Nanocrystals at Low Temperature: Fast Single-Photon Emission, Reduced Blinking, and Exciton Fine Structure. *ACS Nano* **2016,** *10* (2), 2485-2490.

18. Ramasamy, P.; Lim, D.-H.; Kim, B.; Lee, S.-H.; Lee, M.-S.; Lee, J.-S., All-Inorganic Cesium Lead Halide Perovskite Nanocrystals for Photodetector Applications. *Chemical Communications* **2016,** *52* (10), 2067-2070.

19. Song, J.; Li, J.; Li, X.; Xu, L.; Dong, Y.; Zeng, H., Quantum Dot Light-Emitting Diodes Based on Inorganic Perovskite Cesium Lead Halides ($CsPbX_3$). *Advanced Materials* **2015,** *27* (44), 7162-7167.

20. Yang, D.; Cao, M.; Zhong, Q.; Li, P.; Zhang, X.; Zhang, Q., All-inorganic cesium lead halide perovskite nanocrystals: synthesis, surface engineering and applications. *Journal of Materials Chemistry C* **2019,** *7* (4), 757-789.

21. Zhang, D.; Eaton, S. W.; Yu, Y.; Dou, L.; Yang, P., Solution-Phase Synthesis of Cesium Lead Halide Perovskite Nanowires. *Journal of the American Chemical Society* **2015,** *137* (29), 9230-9233.

22. Zhu, J.; Yang, X.; Zhu, Y.; Wang, Y.; Cai, J.; Shen, J.; Sun, L.; Li, C., Room-Temperature Synthesis of Mn-Doped Cesium Lead Halide Quantum Dots with High Mn Substitution Ratio. *The Journal of Physical Chemistry Letters* **2017,** *8* (17), 4167-4171.

23. Betzig, E.; Patterson, G. H.; Sougrat, R.; Lindwasser, O. W.; Olenych, S.; Bonifacino, J. S.; Davidson, M. W.; Lippincott-Schwartz, J.; Hess, H. F., Imaging intracellular fluorescent proteins at nanometer resolution. *Science* **2006,** *313* (5793), 1642-1645.

24. Enderlein, J., Breaking the diffraction limit with dynamic saturation optical microscopy. *Applied Physics Letters* **2005,** *87*, 094105.

25. Gustafsson, M. G. L.; Shao, L.; Carlton, P. M.; Wang, C. J. R.; Golubovskaya, I. N.; Cande, W. Z.; Agard, D. A.; Sedat, J. W., Three-dimensional resolution doubling in wide-field fluorescence microscopy by structured illumination. *Biophysical journal* **2008,** *94*, 4957-4970.

26. Hell, S. W.; Wichmann, J., Breaking the diffraction resolution limit by stimulated emission: stimulated emission-depletion fluorescence microscopy. *Optics Letters* **1994,** *19* (11), 780-782.

27. Lesoine, M. D.; Bhattacharjee, U.; Guo, Y.; Vela, J.; Petrich, J. W.; Smith, E. A., Subdiffraction, luminescence-depletion imaging of isolated, giant, CdSe/CdS nanocrystal quantum dots. *J Phys Chem C* **2013,** *117*, 3662-3667.

28. Medintz, I. L.; Uyeda, H. T.; Goldman, E. R.; Mattoussi, H., Quantum dot bioconjugates for imaging, labelling and sensing. *Nature materials* **2005,** *4* (6), 435.

29. Rust, M. J.; Bates, M.; Zhuang, X., Sub-diffraction-limit imaging by stochastic optical reconstruction microscopy (STORM). *Nature methods* **2006,** *3* (10), 793.

30. Schermelleh, L.; Ferrand, A.; Huser, T.; Eggeling, C.; Sauer, M.; Biehlmaier, O.; Drummen, G. P., Super-resolution microscopy demystified. *Nature cell biology* **2019,** *21* (1), 72.

31. Schwartz, O.; Levitt, J. M.; Tenne, R.; Itzhakov, S.; Deutsch, Z.; Oron, D., Superresolution microscopy with quantum emitters. *Nano letters* **2013,** *13* (12), 5832-5836.

32. Wei, F.; Lu, D.; Shen, H.; Wan, W.; Ponsetto, J. L.; Huang, E.; Liu, Z., Wide field super-resolution surface imaging through plasmonic structured illumination microscopy. *Nano letters* **2014,** *14* (8), 4634-4639.

33. Yamanaka, M.; Yonemaru, Y.; Kawano, S.; Uegaki, K.; Smith, N. I.; Kawata, S.; Fujita, K., Saturated excitation microscopy for sub-diffraction-limited imaging of cell clusters. *Journal of biomedical optics* **2013,** *18* (12), 126002-126002.

34. Yang, B.; Trebbia, J.-B.; Baby, R.; Tamarat, P.; Lounis, B., Optical nanoscopy with excited state saturation at liquid helium temperatures. *Nature Photonics* **2015,** *9* (10), 658-662.

35. Shen, H.; Tauzin, L. J.; Baiyasi, R.; Wang, W.; Moringo, N.; Shuang, B.; Landes, C. F., Single particle tracking: from theory to biophysical applications. *Chemical Reviews* **2017,** *117* (11), 7331-7376.

36. Ma, Y.; Wang, M.; Li, W.; Zhang, Z.; Zhang, X.; Tan, T.; Zhang, X.-E.; Cui, Z., Live cell imaging of single genomic loci with quantum dot-labeled TALEs. *Nature communications* **2017,** *8*, 15318.

37. Gonda, K.; Miyashita, M.; Higuchi, H.; Tada, H.; Watanabe, T. M.; Watanabe, M.; Ishida, T.; Ohuchi, N., Predictive diagnosis of the risk of breast cancer recurrence after surgery by single-particle quantum dot imaging. *Scientific reports* **2015,** *5*, 14322.

38. Han, H.-S.; Niemeyer, E.; Huang, Y.; Kamoun, W. S.; Martin, J. D.; Bhaumik, J.; Chen, Y.; Roberge, S.; Cui, J.; Martin, M. R., Quantum dot/antibody conjugates for in vivo cytometric imaging in mice. *Proceedings of the National Academy of Sciences* **2015,** *112* (5), 1350-1355.

39. Yonemaru, Y.; Yamanaka, M.; Smith, N. I.; Kawata, S.; Fujita, K., Saturated excitation microscopy with optimized excitation modulation. *ChemPhysChem* **2014,** *15* (4), 743-749.

40. Yamanaka, M.; Saito, K.; Smith, N. I.; Kawata, S.; Nagai, T.; Fujita, K., Saturated excitation of fuorescent proteins for subdiffraction-limited imaging of living cells in three dimensions. *Interface Focus* **2013,** *3*, 1-7.

41. Yamanaka, M.; Tzeng, Y.-K.; Kawano, S.; Smith, N. I.; Kawata, S.; Chang, H.-C.; Fujita, K., SAX microscopy with fluorescent nanodiamond probes for high-resolution fluorescence imaging. *Biomedical optics express* **2011,** *2* (7), 1946-1954.

42. Fujita, K.; Kobayashi, M.; Kawano, S.; Yamanaka, M.; Kawata, S., High-resolution confocal microscopy by saturated excitation of fluorescence. *Physical Review Letters* **2007,** *99*, 228105.

43. Gustafsson, M. G. L., Nonlinear structured-illumination microscopy: wide-field fluorescence imaging with theoretically unlimited resolution. *Proceedings of the National Academy of Sciences* **2005,** *102* (37), 13081-13086.

44. Heintzmann, R.; Jovin, T. M., Saturated patterned excitation microscopy—a concept for optical resolution improvement. *Journal of the Optical Society of America A* **2002,** *19* (8), 1599-1609.

CHAPTER 2. GERMANIUM–TIN/CADMIUM SULFIDE CORE/SHELL NANOCRYSTALS WITH ENHANCED NEAR-INFRARED PHOTOLUMINESCENCE

Brett W. Boote[†], Long Men[†], Himashi P. Andaraarachchi, Ujjal Bhattacharjee, Jacob W. Petrich, Javier Vela*, Emily A. Smith*

Modified from a manuscript published in *Chemistry of Materials*, **2017**, *29*, 6012-6021.

Affiliations

The Ames Laboratory, U.S. Department of Energy, and Department of Chemistry, Iowa State University, Ames, Iowa 50011-3111, United States

[†]*These authors contributed equally to this manuscript*

Abstract

$Ge_{1-x}Sn_x$ alloy nanocrystals and $Ge_{1-x}Sn_x$/CdS core/shell nanocrystals were prepared *via* solution phase synthesis and their size, composition, and optical properties were characterized. The diameter of the nanocrystal samples ranged from 6 to 13 nm. The crystal structure of the $Ge_{1-x}Sn_x$ materials was consistent with cubic diamond phase while the CdS shell was consistent with the zinc blende polytype. Inclusion of Sn alone does not result in enhanced photoluminescence intensity, however, adding an epitaxial CdS shell onto the $Ge_{1-x}Sn_x$ nanocrystals does enhance the photoluminescence up to 15× over Ge/CdS nanocrystals with a pure Ge core. More effective passivation of surface defects—and a consequent decrease in surface oxidation—by the CdS shell as a result of

improved epitaxy (smaller lattice mismatch) is the most likely explanation for the increased photoluminescence observed for the $Ge_{1-x}Sn_x$/CdS materials. With enhanced photoluminescence in the near-infrared, $Ge_{1-x}Sn_x$ core/shell nanocrystals might be useful alternatives to other materials for energy capture and conversion applications and as imaging probes.

Introduction

Ge-based materials have garnered significant attention recently as alternatives to other well-studied luminescent semiconductors, such as cadmium and lead chalcogenides.[9, 45] Materials made of elemental Ge have band gaps in the 0.67 to 1.6 eV range for bulk and highly confined (~2-3 nm) nanocrystals, respectively.[46] The large blue shift in the band gap of the nanocrystals is due to size-dependent quantum confinement. Though prone to oxidation when uncoated, Ge nanocrystals have been shown to exhibit increased stability as well as enhanced photoluminescence when a suitable shell is added.[47-48]

Ge initially would seem to have limited utility in energy applications due to its inherent indirect band gap, which lowers its absorption cross-section and quantum yields. Recent reports suggest incorporation of Sn into Ge nanocrystals and thin films should produce a more direct band gap as a result of lattice strain.[49-51] For thin films, modifying the substrate on which the films are grown also allows the strain to be tuned while keeping the Sn composition constant.[52] A careful study of the bowing parameter on $Ge_{1-x}Sn_x$ films showed the crossover Sn content to be $x = 0.087$, which was higher than previously predicted.[53] It has also been shown by Senaratne *et al.* that n-type doping of $Ge_{1-x}Sn_x$ films enhances the photoluminescence.[54] Recently, Stange *et al.* demonstrated a

strain-dependent indirect-to-direct band gap transition in $Ge_{0.875}Sn_{0.125}$ thin films grown on Ge buffer layers.[55] Band gap characteristics of related Ge-rich $Ge_{1-x}Si_x$ films have also been studied as a step toward the design of ternary systems based on Si, Ge, and Sn.[45]

Over the last decade, various methods to prepare Ge nanocrystals have been developed. Reduction of germanium halides ($GeCl_4$, $GeBr_2$, GeI_2 or GeI_4) using strong reducing agents ($NaBH_4$, $LiAlH_4$, etc.) in the presence of suitable surfactants [oleylamine, octadecene (ODE), trioctylphosphine (TOP)] is widely used to make monodisperse Ge nanocrystals.[56-65] Heating a solution of $GeBr_2$ or GeI_2 with a surfactant has also been shown to generate Ge nanocrystals.[66-68] Co-reduction of GeI_2 and GeI_4 is another common strategy for generating Ge nanocrystals in the ~2-20 nm size regime, where the precursor ratio controls the particle size.[46, 69-73] The polymerization of $[Ge_9]^{4-}$ or other related Zintl ions, both with and without linking cations such as Ge^{4+} or Pt^{2+}, generates highly ordered, porous Ge nanocrystals.[74-78] Other preparations involve reduction of Ge-rich oxides,[79-84] heat-assisted reduction of the GeH_2 Wittig adduct $Ph_3PCMe_2 \cdot GeH_2 \cdot BH_3$,[85-86] laser photolysis of $Ge(CH_3)_4$ or GeH_4 gas,[87-89] photolysis of Ge wafer,[90] electroless deposition on preformed Ag nanocrystals,[91] Au-catalyzed vapor-liquid-solid growth using GeH_4[92] or diphenylgermane,[93] ultrasonic aerosol pyrolysis of tetrapropylgermane,[94] solution or solid phase reduction of NaGe,[95] plasma decomposition of $GeCl_4$[96-98] or GeH_4,[99] sulfur-assisted thermal decomposition of triphenylgermanium chloride,[100] and heating a solution of an alkylgermane in various high-temperature organic solvents.[101]

The preparation of Ge-Sn alloy nanocrystals typically follows one of the aforementioned strategies with the addition of a suitable Sn precursor, such as tin(II)

chloride ($SnCl_2$) or bis(trimethylsilyl)amide [$Sn(HDMS)_2$].[10, 49] A recent report showed the bottom-up formation of $Ge_{1-x}Sn_x$ nanowires grown from Sn nanocrystals.[102] The concentration of Sn in these nanowires was found to be 12.4 atom% (x = 0.124). $Ge_{1-x}Sn_x$ nanowires have also been formed from mixed Ge(II) and Sn(II) imido cubane precursors.[103] Spherical, Sn-rich Ge-Sn nanocrystals within a Ge matrix were prepared by annealing a Ge-Sn alloy layer cast between two thick layers of Ge.[104] Small aspect ratio Ge-Sn nanorod heterostructures have been prepared in one-pot through sequential additions of Sn and Ge precursors.[105] There are also several reports on Ge-Sn alloy thin films to study strained and relaxed phases.[50, 52, 106-107]

Raman spectroscopy is very useful for the characterization of multiple component inorganic materials. It can be used to characterize amorphous *vs.* crystalline materials[101] and to determine strain within alloy systems.[49, 102-103] Lin *et al.* independently found the contributions of alloy composition and strain to the shift in the Ge-Ge longitudinal optical (LO) phonon in $Ge_{1-x}Sn_x$ films by tuning substrate topology.[52] They found a linear dependence between the Raman shift and film strain ($\Delta\omega = -(563 \pm 34)\varepsilon$ cm^{-1}) as well as Sn composition ($\Delta\omega = -(82 \pm 4)x$ cm^{-1}) where ε is the strain (in fractional form) and x is the Sn composition. Esteves *et al.* measured the Ge LO phonon mode by Raman spectroscopy for spherical $Ge_{1-x}Sn_x$ nanocrystals with increasing Sn content up to x = 0.279.[49] Increasing Sn content was associated with a lower Raman shift from ~294 to 287 cm^{-1}, which they attributed to combined alloy composition and lattice strain. Using Raman spectroscopy and scanning tunneling electron microscopy with energy dispersive X-ray spectroscopy (STEM-EDX), Seifner *et al.* correlated a shift in the LO phonon mode with varying Sn content for $Ge_{1-x}Sn_x$ nanorods.[103] A maximum shift in the LO

phonon mode of -15 cm^{-1} was observed for nanorod sections where the mole fraction of Sn was at least 0.20. Similar behavior in $Ge_{1-x}Sn_x$ nanorods was observed by Biswas and coworkers.[93]

X-ray photoelectron spectroscopy (XPS) is another technique well suited to characterize Ge materials since they are prone to oxidation. XPS data for $Ge_{1-x}Sn_x$ nanocrystals synthesized by Ramasamy *et al.* showed typical peaks corresponding to Ge^0, Ge^{2+}, Ge^{4+}, Sn^0, and a broad, overlapping peak for Sn^{2+} and Sn^{4+}.[10] Relatively high ratios of the metallic peak to the oxidized peaks correlate to very little surface oxidation of these nanocrystals. Esteves and coworkers observed similar results, where three types of peaks were present: metallic Ge^0 and Sn^0 peaks from interior atoms, Ge^{2+} and $Sn^{2+/4+}$ peaks from atoms bound to passivating ligands, and a small Ge^{4+}peak from GeO_2 at the surface.[49] It has also been shown by XPS that treating Ge nanocrystals with dilute HCl removed a high percentage of a GeO_2 layer at the surface, with weakly bound Cl^- acting as a passivating ligand.[88] Indeed, all reports on the preparation of Ge nanocrystals where XPS was performed show strong peaks for Ge^0 and small contributions from oxidized species, whether they are attributed to surface ligands and/or surface oxidation (GeO_2).[62, 72, 108]

The photoluminescence (PL) properties of Ge-based materials are highly sensitive to the resultant size of the nanocrystals as well as other properties such as the capping ligand used.[46-47, 61, 96, 109] Lee *et al.* prepared Ge nanocrystals stabilized with 1-octadecene that exhibited luminescence maxima from 900 to 1400 nm for diameters 3.2 to 4.0 nm.[61] Ruddy and coworkers demonstrated luminescent 2.3-4.7 nm nanocrystals capped with 1-octadecene prepared by co-reduction of GeI_2 and GeI_4 with size-dependent near-infrared

PL from 860-1230 nm.[46] Guo *et al.* demonstrated 7 nm Ge/4.9CdS core/shell nanocrystals that exhibited a PL maximum at 950 nm.[47] Wheeler and coworkers showed 4.8-10.2 nm Ge nanocrystals capped with alkyl chains synthesized in the vapor phase that exhibit PL from 1200-1610 nm.[96] Recently, Robel and coworkers monitored the combined effect of temperature and high magnetic field on the PL lifetimes of Ge nanocrystals, which showed splitting between closely-spaced states as well as mixing between dark and bright states all contribute toward the indirect PL.[109] The intricacies of these widely varying optical properties are not clear: surface states very likely play a role for the luminescence in the visible region, as this extent of a blue shift from the bulk band gap is not explained by confinement alone.

Temperature-dependent PL studies have also been performed to examine the direct and indirect band gap contributions of $Ge_{1-x}Sn_x$ materials.[110-111] The Arachchige group has demonstrated highly confined $Ge_{1-x}Sn_x$ nanocrystals showing PL in the 620 to 770 nm range, which closely follow calculations using *ab initio* HSE hybrid functional theory. They also used time-resolved PL at low (15 K) and ambient temperatures to further understand carrier dynamics.[112-113] PL lifetimes at 15 K were found to be 3-27 μs, three orders of magnitude slower than at room temperature, owing to slow recombination of carriers in surface traps and spin-forbidden dark excitons. Temperature effects on the PL of very thin $Ge_{1-x}Sn_x$ films have also been studied, showing a monotonic thermal PL quenching despite the indirect nature of the band gap.[114]

Reported herein are the comparative solution phase synthesis, characterization, and optical properties of $Ge_{1-x}Sn_x$ alloy nanocrystals *vs.* $Ge_{1-x}Sn_x$/CdS core/shell nanocrystals. All nanocrystalline samples were characterized by X-ray diffraction (XRD),

transmission electron microscopy (TEM), Raman spectroscopy, X-ray photoelectron spectroscopy (XPS), and steady-state and time-resolved near infrared PL spectroscopy. The purpose of this work is to better understand the photophysical properties of Sn-doped Ge-based nanocrystals that may be useful for energy-related applications such as photovoltaics, light emitting devices (LEDs) or, with appropriate surface passivation,[115-116] as near-infrared active luminescent biological markers.

Experimental Section

Materials. Cadmium oxide (CdO, 99.998%), sulfur (S_8, 99.999%) and oleic acid (90%) were purchased from Alfa Aesar; *n*-butyllithum (*n*-BuLi, 1.6 M hexane solution), bis[bis(trimethylsilyl)amido]tin(II) ($Sn(HMDS)_2$, ≥99.0%), oleylamine (OLA, ≥80-90.0%) and dioctylamine ($octyl_2NH$, 98%) were purchased from Sigma-Aldrich; hexadecylamine ($hexadecylNH_2$, 98%) and 1-octadecene (ODE, 90%) were purchased from Acros; and germanium(II) iodide (GeI_2, 99.99+%-Ge) was purchased from Strem. Procedures were performed under a dry inert gas atmosphere (N_2 or Ar) inside a glovebox or Schlenk line, unless specified otherwise.

Preparation of Ge and $Ge_{1-x}Sn_x$ (core) nanocrystals. Germanium cores were synthesized by a modified literature procedure.[47] Briefly, GeI_2 (0.049 g, 0.15 mmol) was added to an oven-dry, four-neck 250 mL round-bottom (R.B.) flask containing hexadecylamine (0.75 g, 3.1 mmol). The contents were degassed under vacuum at 80°C for 30 min, refilled with dry Ar, and heated to 200°C. A mixture of n-BuLi (0.2 mL of 1.6 M hexane solution) and ODE (0.75 mL) was quickly injected while stirring. The temperature was raised from 200°C to 300°C, and the mixture further stirred for 1 h before cooling to room temperature (R.T., 21°C). The nanocrystals were purified by

crashing three times with 10 mL of a 1:1 or 1:3 v/v acetone/methanol solution and centrifugation at 4500 rpm for 5 min, followed by redispersion in 5 mL of toluene.

$Ge_{1-x}Sn_x$ cores were prepared by a modified reported procedure.[10] Briefly, GeI_2 (0.049g, 0.15 mmol) and oleylamine (5 mL for $Ge_{0.95}Sn_{0.05}$; 10 mL for $Ge_{0.75}Sn_{0.25}$) with a varied amount of $Sn(HMDS)_2$ (0.018 g, 0.04 mmol for $Ge_{0.95}Sn_{0.05}$; 0.066 g, 0.15 mmol for $Ge_{0.75}Sn_{0.25}$) were added into a four-neck 250 mL round-bottom flask in a glovebox. The mixture was degassed under vacuum at 80 °C for 30 min, refilled with dry Ar, and heated to 230 °C for $Ge_{0.95}Sn_{0.05}$ or 280°C for $Ge_{0.75}Sn_{0.25}$. The mixture was annealed for 30 min for $Ge_{0.95}Sn_{0.05}$ cores or 5 min for $Ge_{0.75}Sn_{0.25}$ cores before cooling down to R.T.. It should be noted that the exact compositions of $Ge_{1-x}Sn_x$ nanocrystals varied somewhat from batch to batch; the low Sn inclusion preparation varied from 4-8% Sn, while the high Sn inclusion preparation varied from 23-28%. For simplicity, these are labeled as $Ge_{0.95}Sn_{0.05}$ and $Ge_{0.75}Sn_{0.25}$, respectively.

Preparation of Ge/CdS and $Ge_{1-x}Sn_x$/CdS (core/shell) nanocrystals. Ge/CdS or $Ge_{1-x}Sn_x$/CdS core/shell nanocrystals were prepared as follows: precursor solutions of Cd and S were prepared by a literature procedure.[47] 0.1 M $Cd(oleate)_2$ solution: CdO (318 mg, 2.48 mmol), oleic acid (3.09 g, 10.9 mmol), and ODE (7.11 g, 28.2 mmol) were degassed under vacuum at 80°C for 60 min, refilled with Ar, and heated to 240°C until optically clear. The mixture was allowed to cool down to R.T., and $(octyl)_2NH$ (12.5 mL, 41.4 mmol), previously degassed at 80°C for 30 min, injected into it. 0.1 M S_8 solution: S_8 (79.0 mg, 2.47 mmol) and ODE (19.7 g, 78.1 mmol) were degassed under a vacuum at 80°C for 30 min, refilled with Ar, and heated to 180°C for 20 min until optically clear.

To prepare core-shell nanocrystals *with excess precursors* (one-pot synthesis), a batch of freshly prepared $Ge_{1-x}Sn_x$ cores (in amine or amine/ODE) solution, ODE (1.5 mL, 4.7 mmol), and $(octyl)_2NH$ (1.5 mL, 5.0 mmol) were added to a four-neck 250 mL R.B. flask. The mixture was degassed at 80°C for 30 min, refilled with Ar, and heated to 230°C for Ge and $Ge_{0.95}Sn_{0.05}$ or 250°C for $Ge_{0.75}Sn_{0.25}$). Cd and S precursors were alternately injected using two programmable syringe pumps, each followed by a 15 min wait. The S precursor was injected first. 15 min after the last Cd injection, the mixture was allowed to cool to R.T.. Core-shell nanocrystals were washed as described above for $Ge_{1-x}Sn_x$ nanocrystals.

To prepare core-shell nanocrystals *without excess precursors*, the procedure above was repeated using nanocrystal cores where excess precursors have been removed following the purification method above. Toluene was removed under vacuum prior to shell growth.

Optical Characterization. Solution optical density (absorption plus scattering) spectra were measured with a photodiode array 8453 UV-visible spectrophotometer (Agilent, Santa Clara, CA). Steady-state photoluminescence (PL) spectra were measured using a Horiba-Jobin Yvon Nanolog scanning spectrofluorometer equipped with a liquid nitrogen-cooled InGaAs photodiode array. To account for sample concentration, PL intensities were divided by the optical density at the excitation wavelength of 350 nm. Photoluminescence lifetime measurements were performed using a previously described setup with a Nd:YAG laser (Continuum) and an avalanche photodiode.[117] The samples in toluene solution were excited at 532-nm with a pulse energy of 1 mJ/cm^2. The time-

resolved photoluminescence was collected using an 800-nm long-pass filter and the decay trace was fit to a single or double exponential decay as needed.

Raman microspectroscopy was performed on nanocrystals using a 532-nm Sapphire SF laser (Coherent, Santa Clara, CA) illuminating a DM IRBE inverted light microscope (Leica Microsystems, Buffalo Grove, IL) fitted with a 100× oil (1.47 NA) objective. The nanocrystal solutions were drop cast onto glass slides and dried under ambient conditions. The scattered light was passed into a HoloSpec spectrometer (Kaiser Optical Systems, Ann Arbor, MI) equipped with a Newton 940 CCD camera (Andor Technology, Belfast, United Kingdom). The laser power density was 1.3×10^4 W/cm^2 with a laser spot size of 1 μm, and the acquisition time was 60 s. The data were plotted using IGOR (WaveMetrics, Portland, OR).

Infrared spectroscopy was performed on a Bruker Vertex 80 FT-IR spectrometer equipped with a MIR_IR_XPM detector with 16 scans at a resolution of 4 cm^{-1}. The samples were prepared as drop cast thin films on NaCl salt plates. Background spectra were collected under identical conditions, and samples were continuously purged with dry N_2 to minimize water vapor absorbance.

Structural Characterization. Powder X-ray diffraction (XRD) was measured using Cu Kα radiation on a Rigaku Ultima diffractometer. X-ray photoelectron spectroscopy (XPS) measurements were performed using a Kratos Amicus/ESCA 3400 instrument. The sample was irradiated with 240 W non-monochromated Mg Kα x-rays, and photoelectrons emitted at 0 ° from the surface were analyzed using a DuPont-type analyzer. The pass energy was set at 75 eV. CasaXPS was used to process raw data files. The binding energy of C 1s at 284.6 eV was used as a reference. Depth profiling was

performed using monoatomic Ar ion sputtering for 8 s, followed by XPS acquisition. The acceleration voltage used was 500 V in order to minimize ion-induced reduction. Sample rotation during sputtering was used to achieve uniform etching. Transmission Electron Microscopy (TEM) was conducted using a FEI Tecnai G2 F20 field emission TEM operating at up to 200 kV. Samples were prepared by placing 1 or 2 drops of concentrated toluene solutions onto carbon-coated copper grids. Elemental composition was characterized by energy-dispersive spectroscopy (EDX). Nanocrystal dimensions were measured with ImageJ. The longest dimension was measured and reported. At least 300 nanocrystals were counted in each case. Uncertainties in all measurements are reported as standard deviations.

Results and Discussion

Synthesis and Characterization of $Ge_{1-x}Sn_x$ Core Nanocrystals. Ge, $Ge_{0.95}Sn_{0.05}$, and $Ge_{0.75}Sn_{0.25}$ nanocrystals were prepared and characterized by powder X-ray diffraction (XRD). Patterns of $Ge_{1-x}Sn_x$ nanocrystals shown in **Figure 1** confirm the crystalline products are homogeneous nanoalloys of Ge and α-Sn in the cubic diamond phase with $Fd\overline{3}m$ space group. The composition of Sn incorporated in the cubic Ge lattice was calculated based on Vegard's Law: $a_{(Ge_{1-x}Sn_x)} = a_{(Sn)}(x) + a_{(Ge)}(1-x)$. Here, a is the lattice parameter of the sample or standard and x is the composition of Sn in the nanocrystal. Structural parameters of the Ge and $Ge_{1-x}Sn_x$ nanocrystals, as well as CdS, are shown in **Table 1** and **Figure 2**. The shift in the diffraction peak to lower 2θ angles indicates a lattice expansion from 5.658 Å (Ge) to 5.706 Å ($Ge_{0.95}Sn_{0.05}$) and 5.870 Å ($Ge_{0.75}Sn_{0.25}$). To ensure the measured peak shift was not due to any measurement

variables, such as the sample height in the XRD instrument, Si powder was used as an internal standard to align the experimental pattern for all samples. As is often the case in low temperature, solution-synthesized nanocrystals,[48] the molar ratios of Ge:Sn used in the synthetic preparations were not conserved in the nanocrystal. For instance, the $Ge_{0.75}Sn_{0.25}$ sample was prepared from a 1:1 molar ratio of Ge:Sn. This could be explained, in part, by the comparatively large cationic radius of Sn^{2+} compared to Ge^{2+}, which contributes to Sn having a relatively low solubility in bulk Ge of about ~1%.[118] However, Sn incorporation as high as 42% has been reported in $Ge_{1-x}Sn_x$ nanocrystal alloys,[10] likely because solution phase nanocrystal syntheses are often kinetically and not thermodynamically controlled.

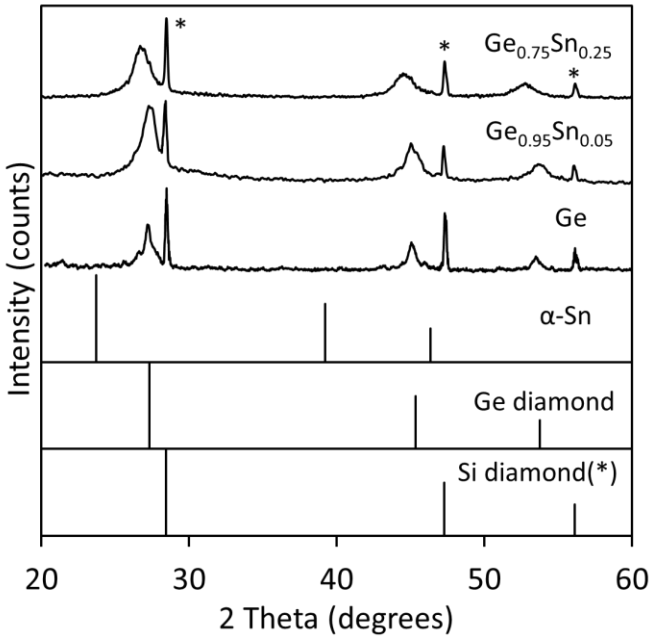

Figure 1. Experimental powder X-ray diffraction (XRD) patterns of Ge and $Ge_{1-x}Sn_x$ alloy nanocrystals. The standard powder XRD patterns of bulk Ge, α-Sn, and Si diamond (* = used as an internal standard) are shown for comparison.

Table 1. Structural parameters of Ge and $Ge_{1-x}Sn_x$ nanocrystals.

Material	Crystal structure	Lattice parameter (Å)	Lattice mismatch[a]
CdS	zinc blende	5.832	0
Ge	diamond	5.658	+3.0%
$Ge_{0.95}Sn_{0.05}$	diamond	5.706	+2.2%
$Ge_{0.75}Sn_{0.25}$	diamond	5.870	-0.65%

[a] $\Delta a = 100 \times (a_{shell} - a_{core})/(a_{core})$; signs refer to shell-induced core expansion (+) or compression (-).

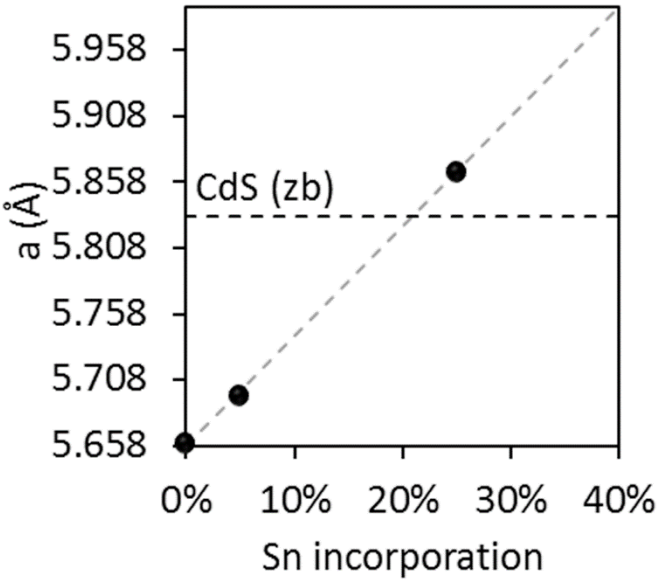

Figure 2. Lattice parameter of $Ge_{1-x}Sn_x$ nanocrystals as a function of Sn incorporation. $Ge_{0.75}Sn_{0.25}$ nanocrystals have the smallest lattice mismatch with the cubic CdS (5.832, horizontal dashed line), compared to Ge or $Ge_{0.95}Sn_{0.05}$. The dashed gray line is a linear regression to the data.

To accurately characterize the morphology and size of the nanocrystals, TEM images were collected (**Figure 3**). Size histograms for each sample are shown in **Figure S1**. Overall, the samples are well dispersed spheroidal nanocrystals with crystal sizes of 6 ± 1 nm (Ge), 6 ± 1 nm ($Ge_{0.95}Sn_{0.05}$), and 11 ± 2 nm ($Ge_{0.75}Sn_{0.25}$). Adding more Sn precursor always leads to larger core particles. In an effort to make $Ge_{1-x}Sn_x$ cores comparable in size to Ge cores, we lowered the precursor solution concentration and shortened the reaction time. However, while this approach works well for $Ge_{0.95}Sn_{0.05}$ with a particle size of 6 ± 1 nm, the smallest $Ge_{0.75}Sn_{0.25}$ we could synthesize still has a

relatively large particle size of 11 ± 2 nm. In addition to TEM, energy dispersive spectrometry (EDX) was performed to assess the particle composition and homogeneity (**Table 2**). EDX data of $Ge_{1-x}Sn_x$ nanocrystals shows good agreement with the theoretical elemental composition calculated by Vegard's Law.

Table 2. TEM-EDX analysis of Ge, $Ge_{1-x}Sn_x$ and $Ge_{1-x}Sn_x$/CdS nanocrystals.

Sample	Size (nm)	Composition: Ge, Sn, Cd, S	
		Theoretical (%)[a]	EDX (%)
Ge	6 ± 1	100, 0, 0, 0	100, 0, 0, 0
$Ge_{0.95}Sn_{0.05}$	6 ± 1	95, 5, 0, 0	90 ± 1, 10 ± 1, 0, 0
$Ge_{0.75}Sn_{0.25}$	11 ± 2	75, 25, 0, 0	78 ± 3, 22 ± 3, 0, 0
Ge/3.4CdS	8 ± 2	19, 0, 41, 41	7 ± 1, 0, 49 ± 1, 44 ± 1
$Ge_{0.95}Sn_{0.05}$/3.4CdS	8 ± 2	29, 2, 35, 35	67 ± 9, 8 ± 7, 18 ± 8, 7 ± 3
$Ge_{0.75}Sn_{0.25}$/3.4CdS	13 ± 2	28, 9, 31, 31	58 ± 3, 4 ± 2, 16 ± 2, 22 ± 1

[a]Based on a 100% Ge_xSn_{1-x}/CdS composition.

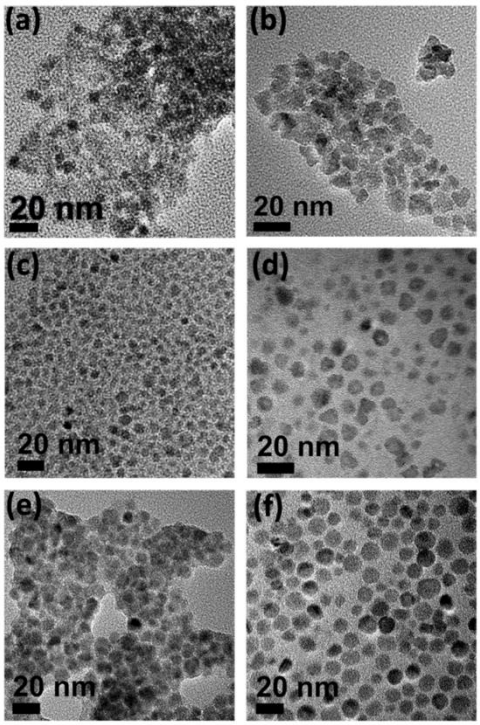

Figure 3. $Ge_{1-x}Sn_x$ core and $Ge_{1-x}Sn_x$/CdS core/shell nanocrystals: (a) Ge (6 ± 1 nm), (b) Ge/CdS (8 ± 2 nm), (c) $Ge_{0.95}Sn_{0.05}$ (6 ± 1 nm), (d) $Ge_{0.95}Sn_{0.05}$/CdS (8 ± 2 nm), (e) $Ge_{0.75}Sn_{0.25}$ (11 ± 2 nm), (f) $Ge_{0.75}Sn_{0.25}$/CdS (13 ± 2 nm). The average size measured from more than 300 nanocrystals is provided in parentheses.

Raman spectra for the Ge-Ge LO phonon mode of pure Ge and $Ge_{1-x}Sn_x$ alloy nanocrystals are shown in **Figure 4a**. As the Sn content is increased, the Ge LO phonon mode is shifted by -1.2 cm^{-1} ($Ge_{0.95}Sn_{0.05}$) and -4.4 cm^{-1} ($Ge_{0.75}Sn_{0.25}$). For the $Ge_{1-x}Sn_x$ alloy system, two additive factors determine the observed peak shift in the Ge-Ge LO phonon: the compositional (pure mass) effect and lattice strain. Deconvoluting the compositional effect and strain has been performed on films, where substrate conditions allow for tuning the strain.[52, 106-107, 119-120] For small nanocrystals it is likely that the compositional effect dominates since strain within the alloy can be dissipated due to a high surface area.[93] The smaller Raman shifts are thus primarily attributed to the larger Sn atoms expanding the crystal lattice as shown by XRD; longer (weaker) bonds are associated with a shift to lower energies. A plot of the Sn compositional dependence of the Ge-Ge LO phonon is shown in **Figure 4b**. For two batches of $Ge_{1-x}Sn_x$ nanocrystals prepared in the same way the best-fit line produced different slopes despite similar compositions being measured by XRD: $\Delta\omega(x) = -(17 \pm 1)x$ and $\Delta\omega(x) = -(42 \pm 5)x$ where x is the Sn composition. At present, it is unclear why the two sets of experiments showed different compositional dependence, and why these values are different than those reported for nanorods[93] and strain-free films[107]—further experiments are underway to investigate this. The line traces shown in **Figure 4a** are two-peak Gaussian fits to the experimental spectra to account for asymmetry at lower Raman shifts. Asymmetry in the phonon peaks of small nanocrystals is attributed to contributions from surface optical (SO) phonons, which are typically slightly lower in energy than the corresponding LO phonons.[121-122] SO phonons are more prominent for anisotropic crystals.[123] The Sn-Ge LO phonon was not observed in the Raman spectrum of the nanoalloy, which is

consistent with previous work on thin films.[107] A Raman spectrum of GeO_2 was also acquired to investigate the possibility of interference from surface oxidation (**Figure S2**), but no GeO_2 bands are observed in the 280 to 320 cm^{-1} Ge-Ge LO phonon range, which is consistent with the literature.[124] Likewise, no additional bands that correlate to GeO_2 were observed outside this spectral range for the Ge and $Ge_{1-x}Sn_x$ nanocrystal samples.

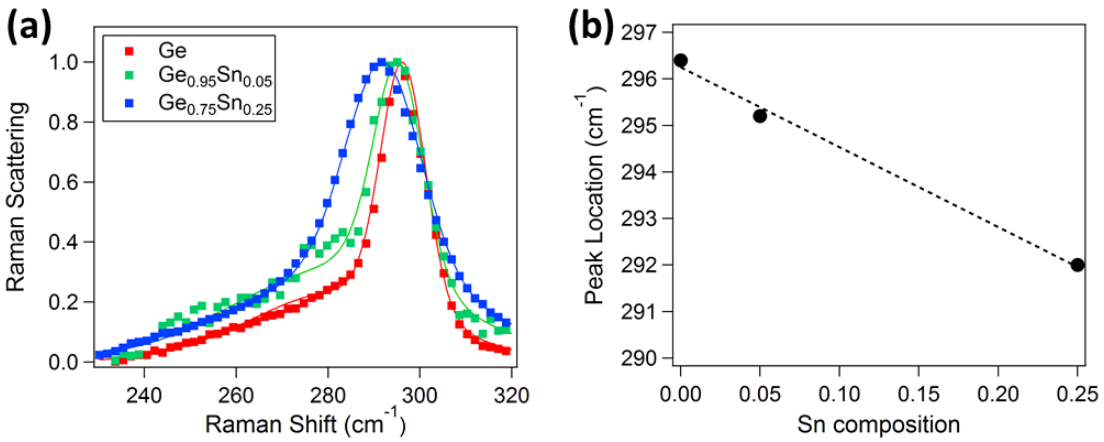

Figure 4. (a) Normalized Raman spectra for Ge and $Ge_{1-x}Sn_x$ alloy nanocrystals and (b) Sn compositional dependence of Ge-Ge LO phonon peak position. As the Sn content increases, the Ge LO phonon peak is shifted to lower wavenumbers and the FWHM increases. Spectra were fit to 2-peak Gaussian curves (solid lines) to account for asymmetry. Average Raman peak properties are listed in Table S1.

Synthesis and Characterization of $Ge_{1-x}Sn_x$/CdS Core/Shell Nanocrystals.

Freshly synthesized $Ge_{1-x}Sn_x$ cores were reacted with Cd and S precursors alternately to form CdS shells using the successive ion layer adsorption and reaction (SILAR) method.[47, 125] Two preparation methods were employed: one using the synthetic mixture of the $Ge_{1-x}Sn_x$ cores without removing the residual precursors (one-pot synthesis), referred to as the crude $Ge_{1-x}Sn_x$ sample, and the second using cores re-suspended in toluene after purification *via* centrifugation, referred to as the purified $Ge_{1-x}Sn_x$ sample. The XRD patterns and Raman spectra of the crude $Ge_{1-x}Sn_x$ samples showed unwanted

SnS (**Figure S3**). Because the core/shell synthesis using crude core solutions did not generate monodisperse core/shell nanocrystals, all core/shell samples discussed in the remaining text were prepared using purified cores. **Figure 5** shows XRD patterns of the core/shell nanocrystals. The Ge/CdS sample showed mainly hexagonal wurtzite structure. Ge/CdS nanocrystals with a predominately wurtzite structure have been reported previously for a preparation using crude core solution.[47] Polytypism in group IV and II-VI nanocrystals, as well as in their epitaxial (core/shell, etc.) systems is relatively common, and can be size-dependent.[126-128]

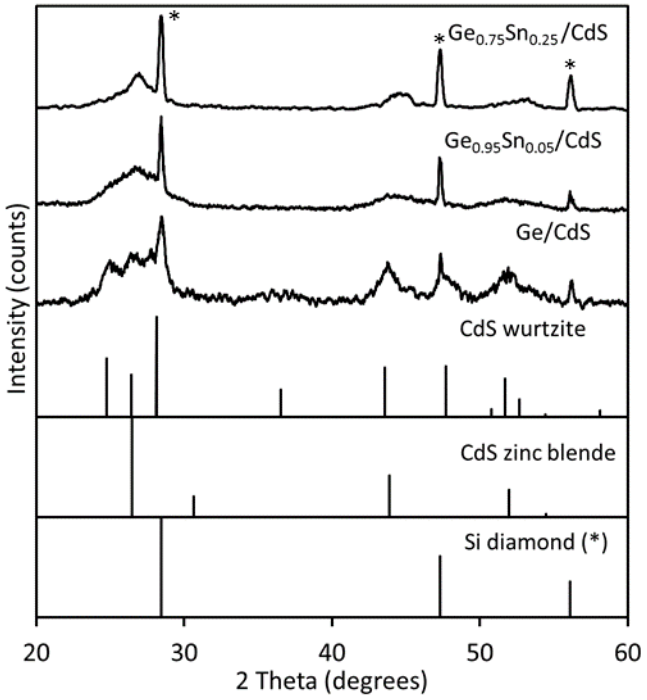

Figure 5. Experimental powder X-ray diffraction (XRD) patterns of Ge/CdS and $Ge_{1-x}Sn_x$/CdS core/shell nanocrystals. The standard powder XRD patterns of bulk CdS zinc blende (cubic), CdS wurtzite (hexagonal), and Si diamond (* = used as an internal standard) are shown for comparison.

To make the core/shell nanocrystals with different Sn incorporations comparable, we grew CdS shells with similar thicknesses. TEM images in **Figure 3** show, in all cases, the core/shell nanocrystals increase 2 nm in diameter compared to their uncoated or bare

cores. When compared to the known lattice parameter of CdS (either wurtzite or zinc blende give similar results), this shell thickness corresponds to the growth of 3.4 monolayers of CdS on the $Ge_{1-x}Sn_x$ cores. Area EDX scans containing several $Ge_{1-x}Sn_x$ cores agree with their theoretical elemental composition; albeit the Ge content in $Ge_{1-x}Sn_x$ /CdS core/shells appears to be larger than the theoretical value. EDX elemental mapping of individual particles show that a majority of $Ge_{1-x}Sn_x$ cores are coated with CdS (**Figure S4**). Many of these core/shell particles have a relatively inhomogeneous shell, which is consistent with well-documented studies on CdSe/CdS core/shell nanocrystals.[115-116, 129-131]

As in the classical CdSe/CdS system, inhomogeneous surface coverage in $Ge_{1-x}Sn_x$ /CdS core/shell nanocrystals is not an immediate problem, at least in terms of ensemble optical properties, as it is able to provide enough surface passivation to enhance and stabilize PL compared to the bare $Ge_{1-x}Sn_x$ cores. High resolution high-angle annular dark-field (HAADF) STEM images of a $Ge_{0.75}Sn_{0.25}$/CdS nanocrystals (**Figure S5**) show the presence of continuous lattice fringes throughout each particle.

Raman spectra for the $Ge_{1-x}Sn_x$/CdS core/shell nanocrystals are shown in **Figure S6**. The Raman shift of the Ge-Ge LO phonon mode for the Ge/CdS nanocrystals is shifted by a statistically significant +1.1 cm^{-1} relative to the nanocrystals without a shell. This implies the shell generates compressive strain on the core, due to the smaller lattice parameter of CdS wurtzite compared to Ge (Ge = 5.658 Å, CdS wurtzite a = 4.135 Å). If CdS (with a peak maximum at 300 cm^{-1}) spectrally interfered with the Ge LO optical phonon mode (with a peak maximum <296 cm^{-1} in the core material), we would expect the peak FWHM to increase. We conclude that CdS does not spectrally interfere in our

data, as the peak FWHM is the same or slightly decreased for the core/shell nanocrystals. In addition, no peaks were measured for pure CdS nanocrystals measured under similar acquisition parameters as those used to collect the data in **Figure S6**. For the $Ge_{1-x}Sn_x$ core/shell samples, the shifts in the LO phonon mode upon shell addition are insignificant (**Table S1**). The lattice parameter for CdS zinc blende (5.82 Å) is closer to the lattice parameter of the alloy core materials (**Table 1**), particularly $Ge_{0.75}Sn_{0.25}$, which is consistent with minimal compressive strain and a negligible phonon mode shift. The smaller lattice mismatch between the $Ge_{1-x}Sn_x$ core nanocrystals and the CdS shell facilitates epitaxial growth of the latter.

X-Ray Photoelectron Spectroscopy of Ge/CdS and $Ge_{1-x}Sn_x$/CdS Core/Shell Nanocrystals. XPS survey spectra of all core/shell nanocrystal samples are shown in the supporting information (**Figure S7**). XPS depth profiling was performed to reveal the sub-surface information of the Ge/CdS core/shell nanocrystals and to corroborate the formation of a core/shell structure (**Figure 6**). We analyzed the chemical states of Ge, Cd, and S. There is no Ge signal above the noise in the initial etching cycles. After a few etching cycles, emerging peaks at ~29.5 eV in the Ge 3d energy region and ~1217 and 1250 eV in the Ge 2p energy region that correspond to metallic Ge^0 were measured, along with a shoulder peak at ~32-33 eV corresponding to $Ge^{2+/4+}$ (**Figure 6a**). These data are consistent with the chemical state of purified Ge core without any shell growth (Ge^0), which exhibits a peak at ~29.5 eV, and mild surface oxidation ($Ge^{2+/4+}$). Furthermore, the core/shell nanocrystals exhibited peaks throughout the etching at ~405 and ~412 eV corresponding to Cd, and a peak at ~162 eV, which corresponds to S^{2-}

(**Figure 6c-d**). This substructure information provides confirmation for the chemical speciation of the core/shell structure of Ge/CdS nanocrystals.

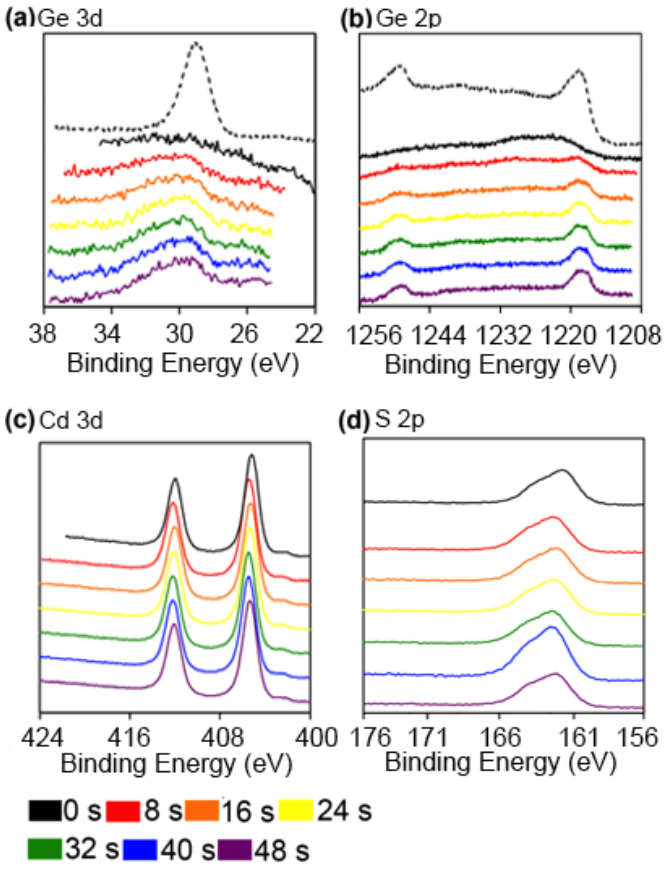

Figure 6. XPS depth profiles of Ge/CdS core/shell nanocrystals. Depth profiling uses an ion beam to etch the layers of the sample revealing sub-surface information; each etching cycle is 8 s and total etching time is indicated by the color of the spectra. Ge nanocrystals with no shell are shown as dashed lines in (a) and (b) for reference, and all the spectra are calibrated to adventitious carbon at 284.6 eV.

We similarly analyzed the chemical states of Ge, Sn, Cd, and S in the purified $Ge_{1-x}Sn_x$ and $Ge_{1-x}Sn_x$/CdS core/shell nanocrystals (**Figure 7**). XPS confirms the element distribution in alloy nanocrystals. The Ge 3d peak at ~29.5 eV and a shoulder around ~32-33 eV corresponds to Ge^0 and $Ge^{2+/4+}$ species, respectively. The peak at ~486 eV corresponds to Sn^{4+} species (SnO_2). Ge and Sn in higher oxidation states indicate post-synthetic surface oxidation. The core/shell

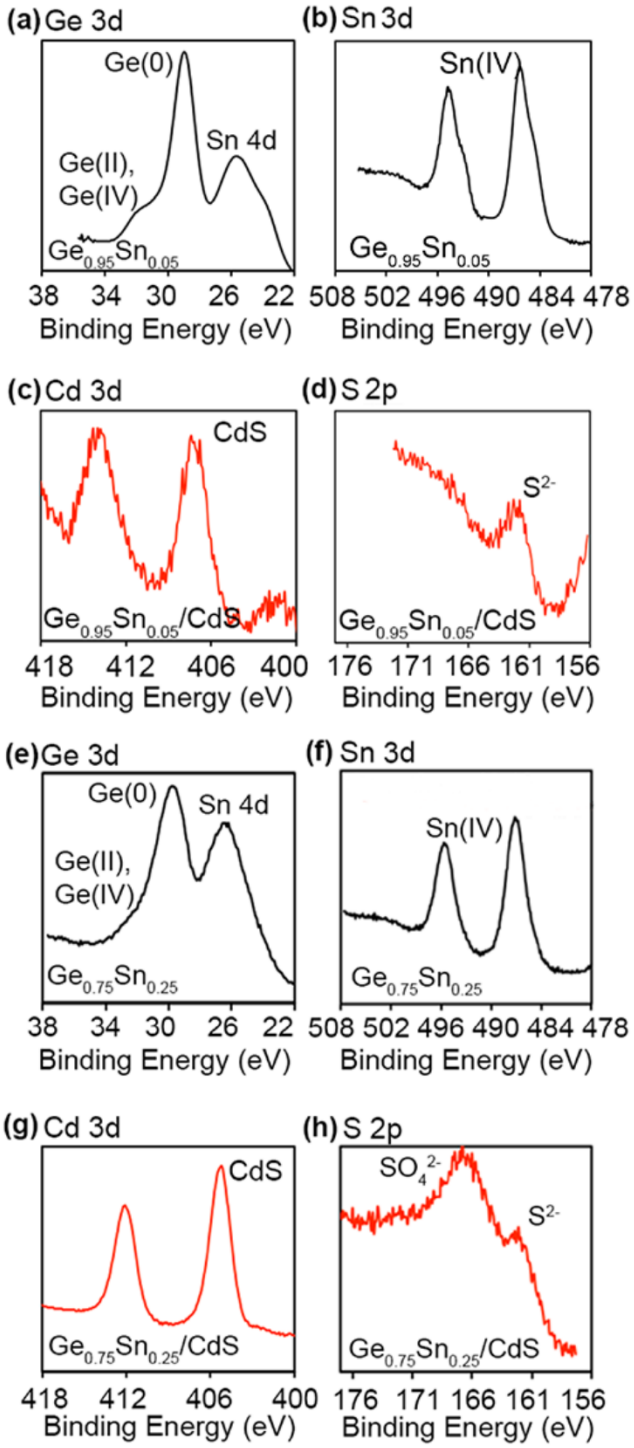

Figure 7. X-ray photoelectron spectra (XPS) of (a-b) $Ge_{0.95}Sn_{0.05}$, (c-d) $Ge_{0.95}Sn_{0.05}$/CdS, (e-f) $Ge_{0.75}Sn_{0.25}$, and (g-h) $Ge_{0.75}Sn_{0.25}$/CdS nanocrystals. All the spectra are calibrated to adventitious carbon at 284.6 eV.

Luminescence Properties of $Ge_{1-x}Sn_x$ Core and $Ge_{1-x}Sn_x$/CdS Core/Shell Nanocrystals. The solution phase optical density spectra of Ge and $Ge_{1-x}Sn_x$ nanoscrystals show no prominent absorption features (**Figure 8**), which could be due to the small bandgap (0.66 eV, 1876 nm for bulk Ge, **Figure S8**) being out of our instrument range. The $Ge_{1-x}Sn_x$/CdS core/shell nanocrystals have absorption onsets at 450-500 nm, which is consistent with the bandgap of quantum confined CdS shells (**Figure S8**).[132]

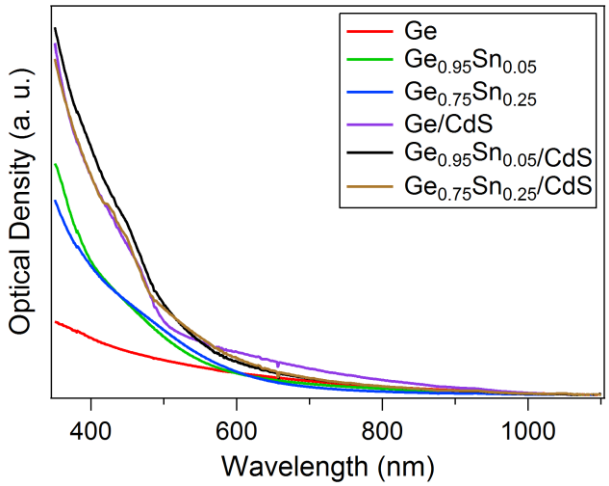

Figure 8. Solution phase optical density (absorption and scattering) spectra of Ge, $Ge_{1-x}Sn_x$, Ge/CdS and $Ge_{1-x}Sn_x$/CdS nanocrystals suspended in toluene.

Photoluminescence spectra of the nanocrystals corrected for optical density at the excitation wavelength of 350 nm are shown in **Figure 9**. For the nanocrystals without shells, the signals from all samples were too low to confidently discriminate them from the instrument's background. This means there is no detectable PL from any of the core-only nanocrystals. Sn inclusion in the alloy nanocrystals is thus not associated with an increase in luminescence intensity. Assuming the doped and undoped samples had similar surface defects and surface oxidation, there is no indication that a more direct band gap character

was achieved in the Sn-doped nanocrystals, as an enhanced PL response was not measured. On the other hand, all the core/shell nanocrystals display an enhanced near infrared PL compared to the $Ge_{1-x}Sn_x$ and Ge nanocrystals without shells. With a bulk band gap of 0.66 eV (**Figure S8**), the PL spectra indicate these core/shells are also quantum confined. The PL enhancements of $Ge_{0.75}Sn_{0.25}$/CdS and $Ge_{0.95}Sn_{0.05}$/CdS were 15× and 12× greater than Ge/CdS, respectively. The luminescence intensity decreases when oxidation is measured by the presence of a Ge-O band in the FT-IR spectrum. $Ge_{0.75}Sn_{0.25}$/CdS core/shells where no oxidation was present show the highest PL intensity. In another set of experiments where oxidation was measured by FT-IR spectroscopy (for example **Figure S9** shows an example of oxidation in the $Ge_{0.75}Sn_{0.25}$ sample), the oxidized core/shells exhibited 100× lower luminescence than the non-oxidized $Ge_{0.75}Sn_{0.25}$/CdS sample (**Figure 9**). The observed PL enhancement is most

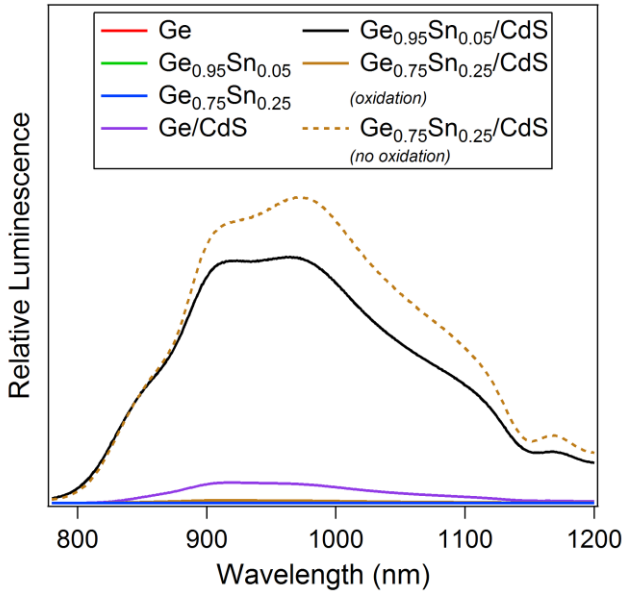

Figure 9. Relative near infrared photoluminescence (PL) spectra of the Ge and $Ge_{1-x}Sn_x$ cores and requisite core/shell nanocrystals. The intensity is normalized by the optical density at the excitation wavelength, λ_{exc} = 350 nm. The Ge, $Ge_{0.95}Sn_{0.05}$, $Ge_{0.75}Sn_{0.25}$, and oxidized $Ge_{0.75}Sn_{0.25}$/CdS samples overlap on this scale.

likely due to more effective surface passivation by the CdS shell on the $Ge_{1-x}Sn_x$ cores, because Sn inclusion in the core without the shell did not result in a higher PL response (see above), whereas oxidation reduces luminescence. Considering the lattice parameters of the core and shell, doping the core with Sn leads to improved epitaxy (smaller lattice mismatch with the shell). This may produce improved crystal growth for core/shell nanocrystals with fewer defects within the crystals that can quench photoluminescence.

Excited-state lifetime measurements for the core/shell nanocrystals are shown in **Figure 10**. These measurements were performed on only the core/shell nanocrystals because the PL intensity of the core-only particles was too low to measure the lifetimes. The Ge/CdS nanocrystals yielded a lifetime of 4.1 µs, which is similar to the previous finding of Guo *et al*.[47] Upon incorporation of Sn in the Ge core, the PL lifetimes decreased to 2.8 and 1.0 µs for $Ge_{0.95}Sn_{0.05}$/CdS and $Ge_{0.75}Sn_{0.25}$/CdS, respectively. The observed decrease in PL lifetime along with higher steady state PL intensity in the

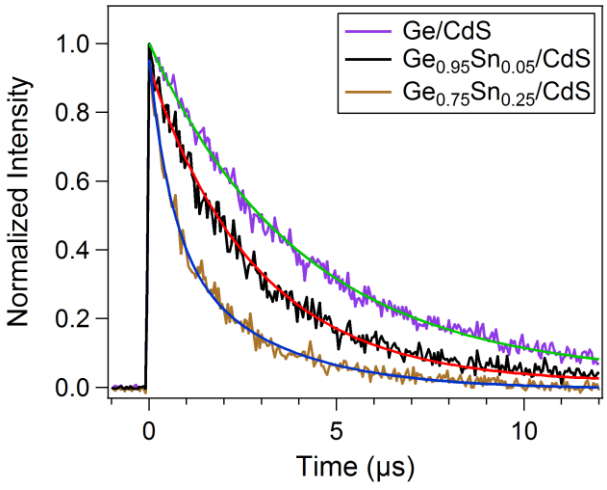

Figure 10. Time-resolved photoluminescence traces of Ge/CdS, $Ge_{0.95}Sn_{0.05}$/CdS, and $Ge_{0.75}Sn_{0.25}$/CdS core/shell nanocrystals. The decays of Ge/CdS and $Ge_{0.95}Sn_{0.05}$/CdS are single-exponential with lifetimes of 4.1 µs and 2.8 µs, respectively, while a double-exponential was used for $Ge_{0.75}Sn_{0.25}$/CdS, yielding an average lifetime of 1.0 µs.

core/shell nanocrystals could be indicative of a more direct band gap. However, there may be no correlation between the steady state PL intensity and the lifetimes of these materials. In order to correlate these two measurements, one would have to show the emitting states are the same for all types of nanocrystals; however, and unlike the case of coating cores of the exact same material but having different sizes, there is no reason to assume this is the case for our series because they are based on chemically distinct cores (materials with different doping levels).

Conclusion

$Ge_{1-x}Sn_x$ alloy nanocrystals and $Ge_{1-x}Sn_x$ core/shell nanocrystals were prepared *via* solution-based synthesis and characterized by XRD, TEM, Raman, optical, and X-ray photoelectron spectroscopy. Incorporation of Sn did not increase the PL intensity in the cores, but core/shell nanocrystals prepared using the Sn-doped cores and CdS shell show up to 15× enhanced PL when compared to Ge/CdS materials. This is explained by improved epitaxy between the lattice-expanded Sn-doped Ge cores and the structurally similar CdS shell, along with reduced surface oxidation. The combination of scalability and improved PL intensities make these $Ge_{1-x}Sn_x$ core/shell nanocrystals promising alternatives to other near infrared-active materials for use as functional materials in solar cells and LEDs. In addition, these nanocrystals have potential as anode materials in advanced lithium ion batteries, and when combined with available biocompatibility steps (ligand exchange and surface-protection or encapsulation), as near-infrared luminescent markers in biological studies.

Acknowledgements

This research is supported by the U.S. Department of Energy, Office of Basic Energy Sciences, Division of Chemical Sciences, Geosciences, and Biosciences through the Ames Laboratory. Electron microscopy characterization was performed at Ames Laboratory's Sensitive Instrument Facility. Ames Laboratory is operated for the U.S. Department of Energy by Iowa State University under contract # DE-AC02-07CH11358. The authors thank Duane Johnson and Gordie Miller for comments. XPS work was performed at the Materials Analysis and Research Laboratory of the Iowa State University Office of Biotechnology. We thank Dapeng Jing for XPS measurements and discussions.

References

9. Vaughn, D. D., II; Schaak, R. E., Synthesis, Properties and Applications of Colloidal Germanium and Germanium-Based Nanomaterial. *Chem. Soc. Rev.* **2013,** *42* (7), 2861–2879.

10. Ramasamy, K.; Kotula, P. G.; Fidler, A. F.; Brumbach, M. T.; Pietryga, J. M.; Ivanov, S. A., Sn_xGe_{1-x} Alloy Nanocrystals: A First Step toward Solution-Processed Group IV Photovoltaics. *Chem. Mater.* **2015,** *27* (13), 4640–4649.

45. Xu, C.; Gallagher, J. D.; Senaratne, C. L.; Menéndez, J.; Kouvetakis, J., Optical Properties of Ge-Rich $Ge_{1-x}Si_x$ Alloys: Compositional Dependence of the Lowest Direct and Indirect Gaps. *Phys. Rev. B* **2016,** *93* (12), 125207-1–125207-16.

46. Ruddy, D. A.; Johnson, J. C.; Smith, E. R.; Neale, N. R., Size and Bandgap Control in the Solution-Phase Synthesis of Near-Infrared-Emitting Germanium Nanocrystals. *ACS Nano* **2010,** *4*, 7459–7466.

47. Guo, Y.; Rowland, C. E.; Schaller, R. D.; Vela, J., Near-Infrared Photoluminescence Enhancement in Ge/CdS and Ge/ZnS Core/Shell Nanocrystals: Utilizing IV/II-VI Semiconductor Epitaxy. *ACS Nano* **2014,** *8*, 8334–8343.

48. Men, L.; White, M. A.; Andaraarachchi, H. A.; Rosales, B. A.; Vela, J., Synthetic Development of Low Dimensional Materials. *Chem. Mater.* **2017,** *29*, 168–175.

49. Esteves, R. J. A.; Ho, M. Q.; Arachchige, I. U., Nanocrystalline Group IV Alloy Semiconductors: Synthesis and Characterization of $Ge_{1-x}Sn_x$ Quantum Dots for Tunable Bandgaps. *Chem. Mater.* **2015,** *27*, 1559–1568.

50. Cheng, R.; Wang, W.; Gong, X.; Sun, L.; Guo, P.; Hu, H.; Shen, Z.; Han, G.; Yeo, Y.-C., Relaxed and Strained Patterned Germanium-Tin Structures: A Raman Scattering Study. *J. Solid State Sci.* **2013,** *2* (4), 138–145.

51. Gupta, S.; Magyari-Köpe, B.; Nishi, Y.; Saraswat, K. C., Achieving Direct Band Gap in Germanium Through Integration of Sn Alloying and External Strain. *J. Appl. Phys.* **2013,** *113*, 073707-1–073707-7.

52. Lin, H.; Chen, R.; Huo, Y.; Kamins, T. I.; Harris, J. S., Raman Study of Strained $Ge_{1-x}Sn_x$ Alloys. *Appl. Phys. Lett.* **2011,** *98*, 261917-1–261917-3.

53. Gallagher, J. D.; Senaratne, C. L.; Kouvetakis, J.; Menendez, J., Compositional Dependence of the Bowing Parameter for the Direct and Indirect Band Gaps in $Ge_{1-y}Sn_y$ Alloys. *Appl. Phys. Lett.* **2014,** *105* (14), 142102-1–142102-5.

54. Senaratne, C. L.; Gallagher, J. D.; Xu, C.; Sims, P.; Menendez, J.; Kouvetakis, J., Doping of Direct Gap $Ge_{1-y}Sn_y$ Alloys to Attain Electroluminescence and Enhanced Photoluminescence. *ECS Trans.* **2015,** *69* (14), 157–164.

55. Stange, D.; Wirths, S.; Von Den Driesch, N.; Mussler, G.; Stoica, T.; Ikonic, Z.; Hartmann, J.; Mantl, S.; Grützmacher, D.; Buca, D., Optical Transitions in Direct-Bandgap $Ge_{1-x}Sn_x$ Alloys. *ACS Photonics* **2015,** *2* (11), 1539–1545.

56. Carolan, D.; Doyle, H., Efficient One-Pot Synthesis of Monodisperse Alkyl-Terminated Colloidal Germanium Nanocrystals. *J. Nanopart. Res.* **2014,** *16* (12), 2721-1–2721-8.

57. Carolan, D.; Doyle, H., Size Controlled Synthesis of Germanium Nanocrystals: Effect of Ge Precursor and Hydride Reducing Agent. *Journal of Nanomater.* **2015,** *2015*, 156-1–156-9.

58. Chou, N. H.; Oyler, K. D.; Motl, N. E.; Schaak, R. E., Colloidal Synthesis of Germanium Nanocrystals Using Room-Temperature Benchtop Chemistry. *Chem. Mater.* **2009,** *21*, 4105–4107.

59. Codoluto, S. C.; Baumgardner, W. J.; Hanrath, T., Fundamental Aspects of Nucleation and Growth in the Solution-Phase Synthesis of Germanium Nanocrystals. *CrystEngComm* **2010,** *12* (10), 2903–2909.

60. Karatutlu, A.; Song, M.; Wheeler, A. P.; Ersoy, O.; Little, W. R.; Zhang, Y.; Puech, P.; Boi, F. S.; Luklinska, Z.; Sapelkin, A. V., Synthesis and Structure of Free-Standing Germanium Quantum Dots and Their Application in Live Cell Imaging. *RSC Adv.* **2015,** *5* (26), 20566–20573.

61. Lee, D. C.; Pietryga, J. M.; Robel, I.; Werder, D. J.; Schaller, R. D.; Klimov, V. I., Colloidal Synthesis of Infrared-Emitting Germanium Nanocrystals. *J. Am. Chem. Soc.* **2009,** *131*, 3436–3437.

62. Lu, X. M.; Korgel, B. A.; Johnston, K. P., High Yield of Germanium Nanocrystals Synthesized from Germanium Diiodide in Solution. *Chem. Mater.* **2005,** *17*, 6479–6485.

63. Zhang, Y.; Ersoy, O.; Karatutlu, A.; Little, W.; Sapelkin, A., Local Structure of Ge Quantum Dots Determined by Combined Numerical Analysis of EXAFS and XANES Data. *J. Synchrotron Radiat.* **2016,** *23* (1), 253–259.

64. Prabakar, S.; Shiohara, A.; Hanada, S.; Fujioka, K.; Yamamoto, K.; Tilley, R. D., Size Controlled Synthesis of Germanium Nanocrystals by Hydride Reducing Agents and Their Biological Applications. *Chem. Mater.* **2010,** *22* (2), 482–486.

65. Warner, J. H.; Tilley, R. D., Synthesis of Water-Soluble Photoluminescent Germanium Nanocrystals. *Nanotechnology* **2006,** *17* (15), 3745–3749.

66. Cosentino, S.; Torrisi, G.; Raciti, R.; Zimbone, M.; Crupi, I.; Mirabella, S.; Terrasi, A., Growth Kinetics of Colloidal Ge Nanocrystals for Light Harvesters. *RSC Adv.* **2016,** *6* (44), 38454–38462.

67. Ghosh, B.; Ogawara, M.; Sakka, Y.; Shirahata, N., Reductant-Free Colloidal Synthesis of Near-IR Emitting Germanium Nanocrystals: Role of Primary Amine. *J. Nanosci. Nanotechnol.* **2014,** *14* (3), 2204–2210.

68. Shirahata, N., Solution-Processable White-Light-Emitting Germanium Nanocrystals. *J. Solid State Chem.* **2014,** *214*, 74–78.

69. Holmes, A. L.; Hutges, J.; Reckmann, A.; Muthuswamy, E.; Meerholz, K.; Kauzlarich, S. M., Probing Electronics as a Function of Size and Surface of Colloidal Germanium Nanocrystals. *J. Phys. Chem. C* **2015,** *119* (10), 5671–5678.

70. Muthuswamy, E.; Iskandar, A. S.; Amador, M. M.; Kauzlarich, S. M., Facile Synthesis of Germanium Nanoparticles with Size Control: Microwave versus Conventional Heating. *Chem. Mater.* **2013,** *25*, 1416–1422.

71. Muthuswamy, E.; Zhao, J.; Tabatabaei, K.; Amador, M. M.; Holmes, M. A.; Osterloh, F. E.; Kauzlarich, S. M., Thiol-Capped Germanium Nanocrystals: Preparation and Evidence for Quantum Size Effects. *Chem. Mater.* **2014,** *26*, 2138–2146.

72. Vaughn, D. D., II; Bondi, J. F.; Schaak, R. E., Colloidal Synthesis of Air-Stable Crystalline Germanium Nanoparticles with Tunable Sizes and Shapes. *Chem. Mater.* **2010,** *22*, 6103–6108.

73. Ruddy, D. A.; Erslev, P. T.; Habas, S. E.; Seabold, J. A.; Neale, N. R., Surface Chemistry Exchange of Alloyed Germanium Nanocrystals: A Pathway Toward Conductive Group IV Nanocrystal Films. *J. Phys. Chem. Lett.* **2013,** *4*, 416–421.

74. Armatas, G. S.; Kanatzidis, M. G., Mesoporous Compound Semiconductors from the Reaction of Metal Ions with Deltahedral $[Ge_9]^{4-}$ Clusters. *J. Am. Chem. Soc.* **2008,** *130*, 11430–11436.

75. Armatas, G. S.; Kanatzidis, M. G., High-Surface-Area Mesoporous Germanium from Oxidative Polymerization of the Deltahedral $[Ge_9]^{4-}$ Cluster: Electronic Structure Modulation with Donor and Acceptor Molecule. *Adv. Mater.* **2008,** *20*, 546–550.

76. Armatas, G. S.; Kanatzidis, M. G., Mesoporous Germanium-Rich Chalcogenido Frameworks with Highly Polarizable Surfaces and Relevance to Gas Separation. *Nat. Mater.* **2009,** *8*, 217–222.

77. Armatas, G. S.; Kanatzidis, M. G., Size Dependence in Hexagonal Mesoporous Germanium: Pore Wall Thickness versus Energy Gap and Photoluminescence. *Nano Lett.* **2010,** *2010*, 3330–3336.

78. Bag, S.; Trikalitis, P. N.; Chupas, P. J.; Armatas, G. S.; Kanatzidis, M. G., Porous Semiconducting Gels and Aerogels from Chalcogenide Clusters. *Science* **2007,** *317*, 490–493.

79. Henderson, E. J.; Hessel, C. M.; Cavell, R. G.; Veinot, J. G. C., How Processing Atmosphere Influences the Evolution of GeO_2-Embedded Germanium Nanocrystals Obtained from the Thermolysis of Phenyl Trichlorogermane-Derived Polymers. *Chem. Mater.* **2010,** *22*, 2653–2661.

80. Hoffman, M.; Veinot, J. G. C., Understanding the Formation of Elemental Germanium by Thermolysis of Sol-Gel Derived Organogermanium Oxide Polymers. *Chem. Mater.* **2012,** *24*, 1283–1291.

81. Henderson, E. J.; Hessel, C. M.; Veinot, J. G. C., Synthesis and Photoluminescent Properties of Size-Controlled Germanium Nanocrystals from Phenyl Trichlorogermane-Derived Polymers. *J. Am. Chem. Soc.* **2008,** *130* (11), 3624–3632.

82. Henderson, E. J.; Seino, M.; Puzzo, D. P.; Ozin, G. A., Colloidally Stable Germanium Nanocrystals for Photonic Applications. *ACS Nano* **2010,** *4* (12), 7683–7691.

83. Henderson, E. J.; Veinot, J. G. C., Synthesis of Oxide Encapsulated and Freestanding Hydride Surface Terminated $Si_{1-x}Ge_x$ Nanocrystals. *Chem. Mater.* **2007,** *19*, 1886–1888.

84. Wu, J.; Sun, Y.; Zou, R.; Song, G.; Chen, Z.; Wang, C.; Hu, J., One-Step Aqueous Solution Synthesis of Ge Nanocrystals from GeO_2 Powders. *CrystEngComm* **2011,** *13*, 3674–3677.

85. Purkait, T. K.; Swarnakar, A. K.; De Los Reyes, G. B.; Hegmann, F. A.; Rivard, E.; Veinot, J. G. C., One-pot Synthesis of Functionalized Germanium Nanocrystals from a Single Source Precursor. *Nanoscale* **2015,** *7* (6), 2241–2244.

86. Millo, O.; Balberg, I.; Azulay, D.; Purkait, T. K.; Swarnakar, A. K.; Rivard, E.; Veinot, J. G. C., Direct Evaluation of the Quantum Confinement Effect in Single Isolated Ge Nanocrystals. *J Phys. Chem. Lett.* **2015,** *6* (17), 3396–3402.

87. Kim, C. H.; Im, H. S.; Cho, Y. J.; Jung, C. S.; Jang, D. M.; Myung, Y.; Kim, H. S.; Back, S. H.; Lim, Y. R.; Lee, C.-W.; Park, J., High-Yield Gas-Phase Laser Photolysis Synthesis of Germanium Nanocrystals for High-Performance Photodetectors and Lithium Ion Batteries. *J. Phys. Chem. C* **2012,** *116*, 26190–26196.

88. Kim, S.; Walker, B.; Park, S. Y.; Choi, H.; Ko, S.-J.; Jeong, J.; Yun, M. H.; Lee, J. C.; Kim, D. S.; Kim, J. Y., Size Tailoring of Aqueous Germanium Nanoparticle Dispersions. *Nanoscale* **2014,** *6* (17), 10156–10160.

89. Cho, Y. J.; Kim, C. H.; Im, H. S.; Myung, Y.; Kim, H. S.; Back, S. H.; Lim, Y. R.; Jung, C. S.; Jang, D. M.; Park, J., Germanium–Tin Alloy Nanocrystals for High-Performance Lithium Ion Batteries. *Phys. Chem. Chem. Phys.* **2013,** *15* (28), 11691–11695.

90. Shirahata, N.; Hirakawa, D.; Masuda, Y.; Sakka, Y., Size-Dependent Color Tuning of Efficiently Luminescent Germanium Nanoparticles. *Langmuir* **2013,** *29*, 7401–7410.

91. Nolan, B. M.; Chan, E. K.; Zhang, X.; Muthuswamy, E.; van Benthem, K.; Kauzlarich, S. M., Sacrificial Silver Nanoparticles: Reducing GeI2 To Form Hollow Germanium Nanoparticles by Electroless Deposition. *ACS Nano* **2016,** *10* (5), 5391–5397.

92. Meng, A. C.; Fenrich, C. S.; Braun, M. R.; McVittie, J. P.; Marshall, A. F.; Harris, J. S.; McIntyre, P. C., Core/Shell Germanium/Germanium-Tin Nanowires Exhibiting Room Temperature Direct-and Indirect-Gap Photoluminescence. *Nano Lett.* **2016,** *16*, 7521–7529.

93. Biswas, S.; Doherty, J.; Saladukha, D.; Ramasse, Q.; Majumdar, D.; Upmanyu, M.; Singha, A.; Ochalski, T.; Morris, M. A.; Holmes, J. D., Non-Equilibrium Induction of Tin in Germanium: Towards Direct Bandgap $Ge_{1-x}Sn_x$ Nanowires. *Nat. Commun.* **2016,** *7*, 11405-1–11405-12.

94. Stoldt, C. R.; Haag, M. A.; Larsen, B. A., Preparation of Freestanding Germanium Nanocrystals by Ultrasonic Aerosol Pyrolysis. *Appl. Phys. Lett.* **2008,** *93* (4), 043125-1–043125-3.

95. Ma, X.; Wu, F.; Kauzlarich, S. M., Alkyl-Terminated Crystalline Ge Nanoparticles Prepared From NaGe: Synthesis, Functionalization and Optical Properties. *J. Solid State Chem.* **2008,** *181* (7), 1628–1633.

96. Wheeler, L. M.; Levij, L. M.; Kortshagen, U. R., Tunable Band Gap Emission and Surface Passivation of Germanium Nanocrystals Synthesized in the Gas Phase. *J. Phys. Chem. Lett.* **2013,** *4*, 3392–3396.

97. Gresback, R.; Holman, Z.; Kortshagen, U., Plasma Synthesis of Highly Monodisperse Ge Nanocrystals and Self-Assembly of Dense Nanocrystal Layers. *Mat. Res. Soc. Symp. Proc.* **2007,** *974*, 0974-CC05.

98. Gresback, R.; Holman, Z.; Kortshagen, U., Nonthermal Plasma Synthesis of Size-Controlled, Monodisperse, Freestanding Germanium Nanocrystals. *Appl. Phys. Lett.* **2007,** *91* (9), 093119-1–093119-3.

99. Wheeler, L. M.; Nichols, A. W.; Chernomordik, B. D.; Anderson, N. C.; Beard, M. C.; Neale, N. R., All-Inorganic Germanium Nanocrystal Films by Cationic Ligand Exchange. *Nano Lett.* **2016,** *16* (3), 1949–1954.

100. Warner, J. H., Solution-Phase Synthesis of Germanium Nanoclusters Using Sulfur. *Nanotechnology* **2006,** *19* (22), 5613–5619.

101. Zaitseva, N.; Dai, Z. R.; Grant, C. D.; Harper, J.; Saw, C., Germanium Nanocrystals Synthesized in High-Boiling-Point Organic Solvents. *Chem. Mater.* **2007,** *19* (21), 5174–5178.

102. Barth, S.; Seifner, M. S.; Bernardi, J., Microwave-Assisted Solution–Liquid–Solid Growth of $Ge_{1-x}Sn_x$ Nanowires with High Tin Content. *Chem. Commun.* **2015,** *51*, 12282–12285.

103. Seifner, M. S.; Biegger, F.; Lugstein, A.; Bernardi, J.; Barth, S., Microwave-Assisted $Ge_{1-x}Sn_x$ Nanowire Synthesis: Precursor Species and Growth Regimes. *Chem. Mater.* **2015,** *27* (17), 6125–6130.

104. Tonkikh, A. A.; Zakharov, N. D.; Suvorova, A. A.; Eisenschmidt, C.; Schilling, J.; Werner, P., Cubic Phase Sn-Rich GeSn Nanocrystals in a Ge Matrix. *Cryst. Growth Des.* **2014,** *14* (4), 1617–1622.

105. Bodnarchuk, M. I.; Kravchyk, K. V.; Krumeich, F.; Wang, S.; Kovalenko, M. V., Colloidal Tin-Germanium Nanorods and Their Li-Ion Storage Properties. *ACS Nano* **2014,** *8* (3), 2360–2368.

106. D'Costa, V. R.; Cook, C. S.; Birdwell, A. G.; Littler, C. L.; Canonico, M.; Zollner, S.; Kouvetakis, J.; Menéndez, J., Optical Critical Points of Thin-Film $Ge_{1-y}Sn_y$ Alloys: A Comparative $Ge_{1-y}Sn_y/Ge_{1-x}Si_x$ Study. *Phys. Rev. B* **2006,** *73* (12), 125207-1–125207-16.

107. Li, S. F.; Bauer, M. R.; Menéndez, J.; Kouvetakis, J., Scaling Law for the Compositional Dependence of Raman Frequencies in SnGe and GeSi Alloys. *Appl. Phys. Lett.* **2004,** *84*, 867–869.

108. Dag, Ö.; Henderson, E. J.; Ozin, G. A., Synthesis of Nanoamorphous Germanium and Its Transformation to Nanocrystalline Germanium. *Small* **2012,** *8*, 921–929.

109. Robel, I.; Shabaev, A.; Lee, D. C.; Schaller, R. D.; Pietryga, J. M.; Crooker, S. A.; Efros, A. L.; Klimov, V. I., Temperature and Magnetic-Field Dependence of Radiative Decay in Colloidal Germanium Quantum Dots. *Nano Lett.* **2015,** *15* (4), 2685–2692.

110. Du, W.; Ghetmiri, S. A.; Conley, B. R.; Mosleh, A.; Nazzal, A.; Soref, R. A.; Sun, G.; Tolle, J.; Margetis, J.; Naseem, H. A., Competition of Optical Transitions Between Direct and Indirect Bandgaps in $Ge_{1-x}Sn_x$. *Appl. Phys. Lett.* **2014,** *105* (5), 051104-1–051104-4.

111. Wirths, S.; Geiger, R.; Von Den Driesch, N.; Mussler, G.; Stoica, T.; Mantl, S.; Ikonic, Z.; Luysberg, M. l.; Chiussi, S.; Hartmann, J. M., Lasing in Direct-Bandgap GeSn Alloy Grown on Si. *Nat. Photon.* **2015,** *9* (2), 88–92.

112. Esteves, R. J. A.; Hafiz, S.; Demchenko, D. O.; Özgür, Ü.; Arachchige, I. U., Ultra-Small $Ge_{1-x}Sn_x$ Quantum Dots with Visible Photoluminescence. *Chem. Commun.* **2016,** *52* (78), 11665–11668.

113. Hafiz, S. A.; Esteves, R. J. A.; Demchenko, D. O.; Arachchige, I. U.; Özgür, U., Energy Gap Tuning and Carrier Dynamics in Colloidal $Ge_{1-x}Sn_x$ Quantum Dots. *J. Phys. Chem. Lett.* **2016,** *7* (17), 3295–3301.

114. Pezzoli, F.; Giorgioni, A.; Patchett, D.; Myronov, M., Temperature-Dependent Photoluminescence Characteristics of GeSn Epitaxial Layers. *ACS Photonics* **2016,** *3* (11), 2004–2009.

115. Chen, Y.; Vela, J.; Htoon, H.; Casson, J. L.; Werder, D. J.; Bussian, D. A.; Klimov, V. I.; Hollingsworth, J. A., "Giant" Multishell CdSe Nanocrystal Quantum Dots With Suppressed Blinking. *J. Am. Chem. Soc.* **2008,** *130* (15), 5026–5027.

116. Tan, R.; Yuan, Y.; Nagaoka, Y.; Eggert, D.; Wang, X.; Thota, S.; Guo, P.; Yang, H.; Zhao, J.; Chen, O., Monodisperse Hexagonal Pyramidal and Bipyramidal Wurtzite CdSe-CdS Core–Shell Nanocrystals. *Chem. Mater.* **2017,** *29* (9), 4097–4108.

117. Sainz, M.; Pérez-Rontomé, C.; Ramos, J.; Mulet, J. M.; James, E. K.; Bhattacharjee, U.; Petrich, J. W.; Becana, M., Plant Hemoglobins May Be Maintained in Functional Form by Reduced Flavins in the Nuclei, and Confer Differential Tolerance to Nitro-Oxidative Stress. *Plant J.* **2013,** *76*, 875-887.

118. Olesinski, R. W.; Abbaschian, G. J., The Ge–Sn (Germanium–Tin) System. *Bull. Alloy Phase Diagrams* **1984,** *5*, 265–271.

119. Rojas-Lopez, M.; Navarro-Contreras, H.; Desjardins, P.; Gurdal, O.; Taylor, N.; Carlsson, J.; Greene, J., Raman Scattering from Fully Strained $Ge_{1-x}Sn_x$ ($x <= 0.22$) Alloys Grown on Ge (001) 2x1 by Low-Temperature Molecular Beam Epitaxy. *J. Appl. Phys.* **1998,** *84* (4), 2219–2223.

120. Su, S.; Wang, W.; Cheng, B.; Hu, W.; Zhang, G.; Xue, C.; Zuo, Y.; Wang, Q., The Contributions of Composition and Strain to the Phonon Shift in Alloys. *Solid State Commun.* **2011,** *151* (8), 647–650.

121. Gupta, R.; Xiong, Q.; Mahan, G. D.; Eklund, P. C., Surface Optical Phonons in Gallium Phosphide Nanowires. *Nano Lett.* **2003,** *3*, 1745–1750.

122. Tschirner, N.; Lange, H.; Schliwa, A.; Biermann, A.; Thomsen, C.; Lambert, K.; Gomes, R.; Hens, Z., Interfacial Alloying in CdSe/CdS Heteronanocrystals: A Raman Spectroscopy Analysis. *Chem. Mater.* **2012,** *24*, 311–318.

123. Lange, H.; Artemyev, M.; Woggon, U.; Thomsen, C., Geometry Dependence of the Phonon Modes in CdSe Nanorods. *Nanotechnology* **2009,** *20*, 045705-1–045705-5.

124. Micoulaut, M.; Cormier, L.; Henderson, G. S., The Structure of Amorphous, Crystalline and Liquid GeO_2. *J. Phys.: Condens. Matter* **2006,** *18* (45), R753–R784.

125. Li, J. J.; Wang, Y. A.; Guo, W.; Keay, J. C.; Mishima, T. D.; Johnson, M. B.; Peng, X., Large-Scale Synthesis of Nearly Monodisperse CdSe/CdS Core/Shell Nanocrystals Using Air-Stable Reagents via Successive Ion Layer Adsorption and Reaction. *J. Am. Chem. Soc.* **2003,** *125* (41), 12567–12575.

126. Lopez, F. J.; Givan, U.; Connell, J. G.; Lauhon, L. J., Silicon Nanowire Polytypes: Identification by Raman Spectroscopy, Generation Mechanism, and Misfit Strain in Homostructures. *ACS Nano* **2011,** *5* (11), 8958–8966.

127. Mélinon, P.; Masenelli, B.; Tournus, F.; Perez, A., Playing With Carbon and Silicon at the Nanoscale. *Nat. Mater.* **2007,** *6* (7), 479–490.

128. Segarra, C.; Rajadell, F.; Climente, J. I.; Planelles, J., Influence of Polytypism on the Electronic Structure of CdSe/CdS and CdSe/CdSe Core/Shell Nanocrystals. *J. Phys. Chem. C* **2017,** *121* (11), 6386–6392.

129. Bertoni, G.; Grillo, V.; Brescia, R.; Ke, X.; Bals, S.; Catellani, A.; Li, H.; Manna, L., Direct Determination of Polarity, Faceting, and Core Location in Colloidal Core/Shell Wurtzite Semiconductor Nanocrystals. *ACS Nano* **2012,** *6* (7), 6453–6461.

130. McBride, J.; Treadway, J.; Feldman, L. C.; Pennycook, S. J.; Rosenthal, S. J., Structural Basis for Near Unity Quantum Yield Core/Shell Nanostructures. *Nano Lett.* **2006,** *6* (7), 1496–1501.

131. Rosenthal, S. J.; McBride, J.; Pennycook, S. J.; Feldman, L. C., Synthesis, Surface Studies, Composition and Structural Characterization of CdSe, Core/Shell and Biologically Active Nanocrystals. *Surf. Sci. Rep.* **2007,** *62* (4), 111–157.

132. Guo, Y.; Marchuk, K.; Sampat, S.; Abraham, R.; Fang, N.; Malko, A. V.; Vela, J., Unique Challenges Accompany Thick-Shell CdSe/nCdS (n> 10) Nanocrystal Synthesis. *J. Phys. Chem. C* **2012,** *116*, 2791–2800.

133. Chandrasekhar, H. R.; Humphreys, R. G.; Zwick, U.; Cardona, M., Infrared and Raman Spectra of the IV-VI Compounds SnS and SnSe. *Phys. Rev. B* **1977,** *15* (4), 2177–2183.

134. Gou, X.-L.; Chen, J.; Shen, P.-W., Synthesis, Characterization and Application of SnS_X (x=1, 2) Nanoparticles. *Materials Chemistry and Physics* **2005,** *93*, 557–566.

Supplemental Information

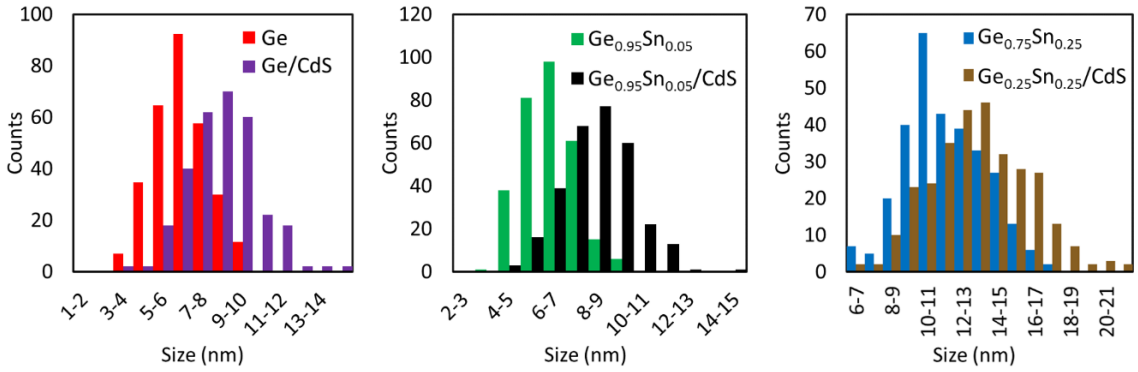

Figure S1. TEM size distribution plots for Ge and $Ge_{1-x}Sn_x$ nanocrystals and core/shell nanocrystals made via overlaying with CdS.

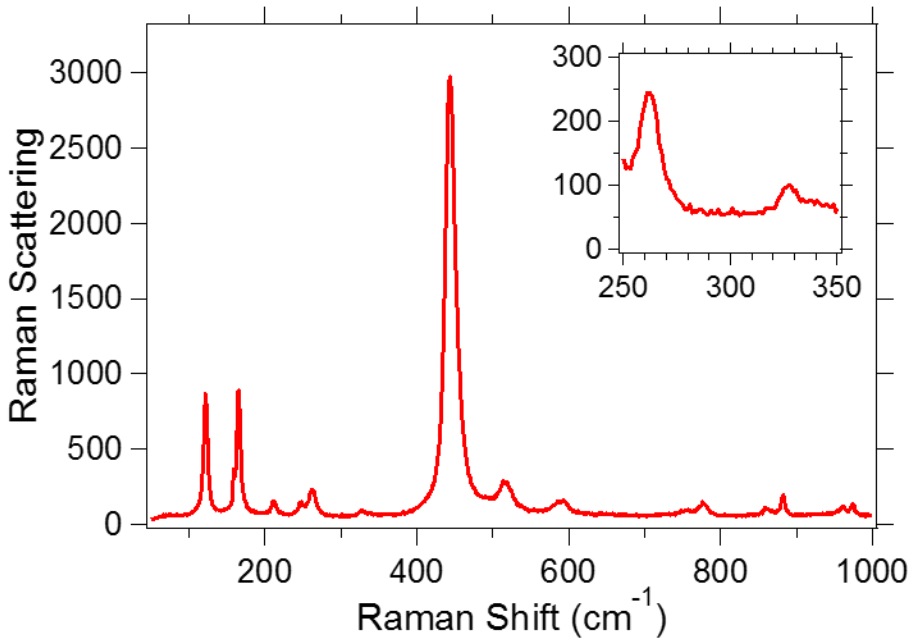

Figure S2. Raman spectrum of solid GeO_2.

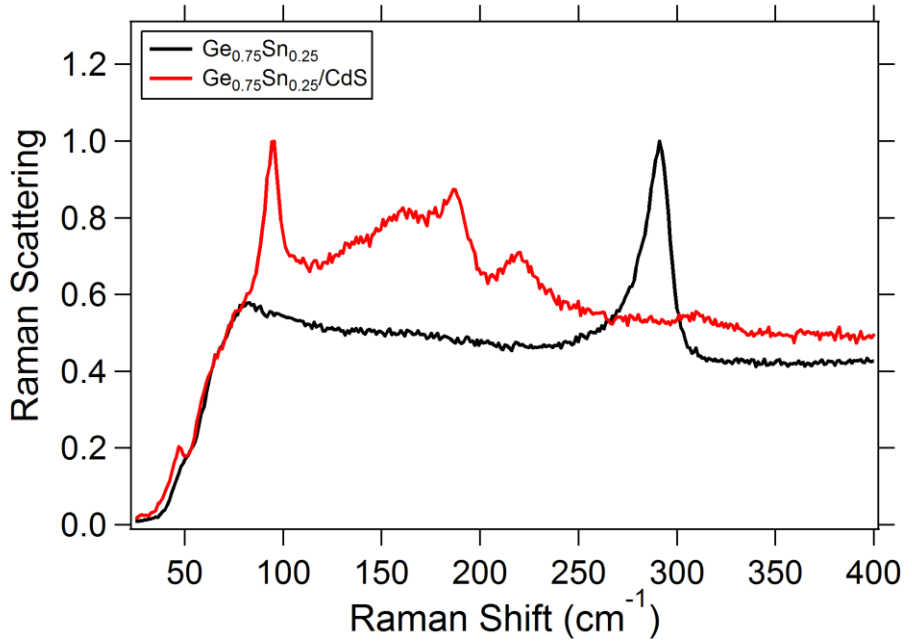

Figure S3. Raman spectrum of the $Ge_{0.75}Sn_{0.25}$ and $Ge_{0.75}Sn_{0.25}$/CdS core/shell nanocrystals made with crude core solution. The core/shell sample show bands that correlate to reported Raman peaks of SnS at ~95, 190, and 220 cm^{-1}.[133-134] The Raman spectra of the $Ge_{0.95}Sn_{0.05}$/CdS sample prepared with a crude core solution was variable across the nanocrystals analyzed, with some showing evidence of SnS.

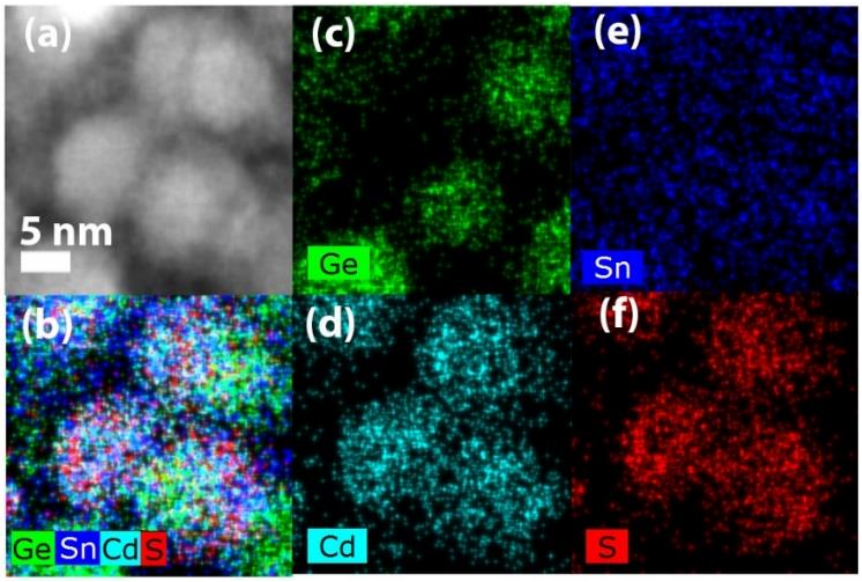
(a)
5 nm
(c)
Ge
(e)
Sn
(b)
Ge Sn Cd S
(d)
Cd
(f)
S

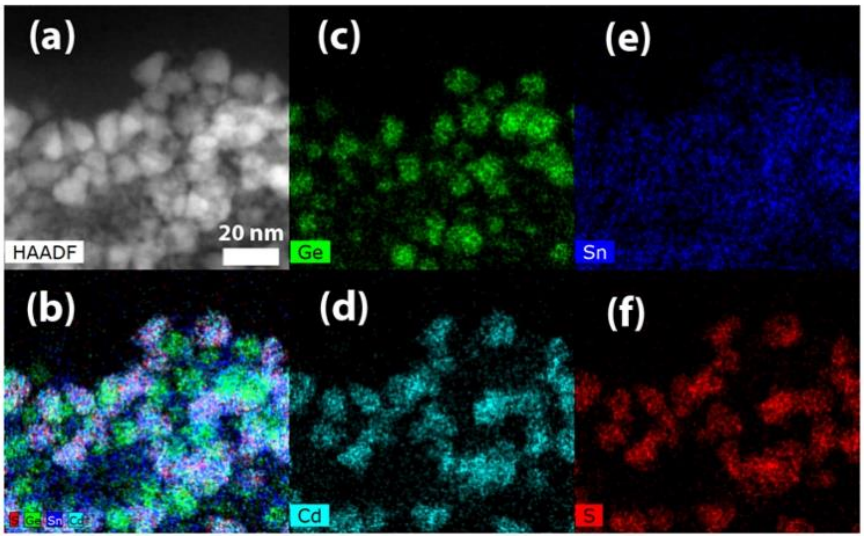
(a)
HAADF
20 nm
(c)
Ge
(e)
Sn
(b)
(d)
Cd
(f)
S

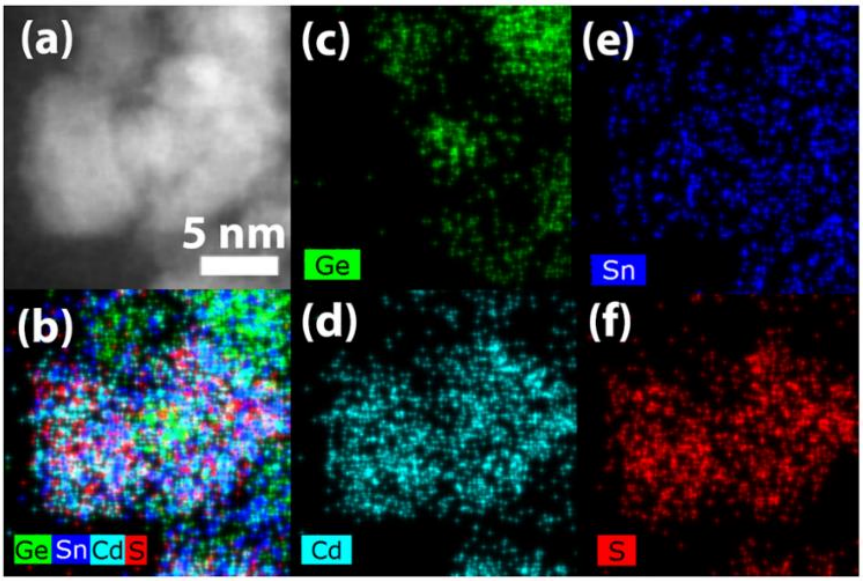

Figure S4. Three representative sets of (a) high-resolution HAADF STEM images of $Ge_{0.75}Sn_{0.25}$/CdS nanocrystals with registered EDX elemental mapping for (b) Ge, Sn, Cd, and S, (c) Ge, (d) Cd, (e) Sn, and (f) S.

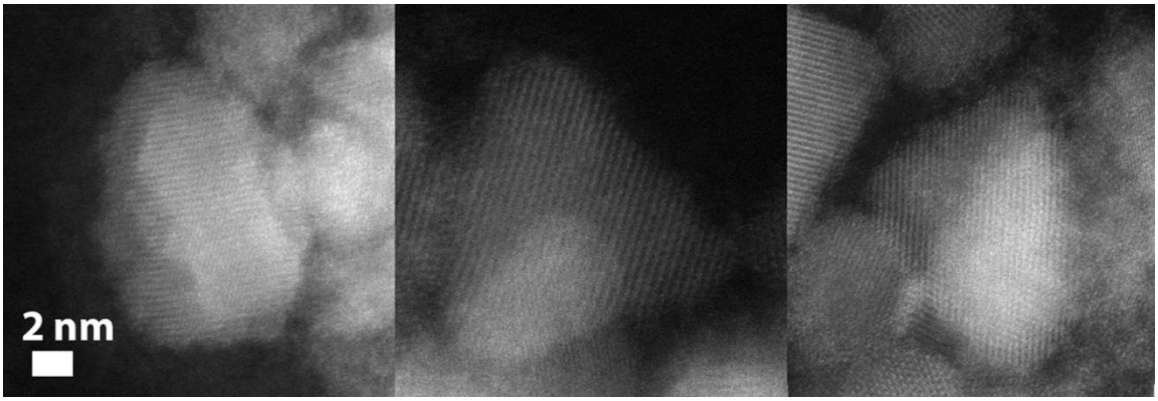

Figure S5. Three sample high resolution high-angle annular dark-field (HAADF) STEM images of a $Ge_{0.75}Sn_{0.25}$/CdS nanocrystals. The average atomic number (Z) of the CdS shell, 32, is similar to that of the Ge core material, 32, making contrast comparisons difficult. However, the presence of continuous lattice fringes throughout each particle is an indication of crystallinity across these core/shell particles.

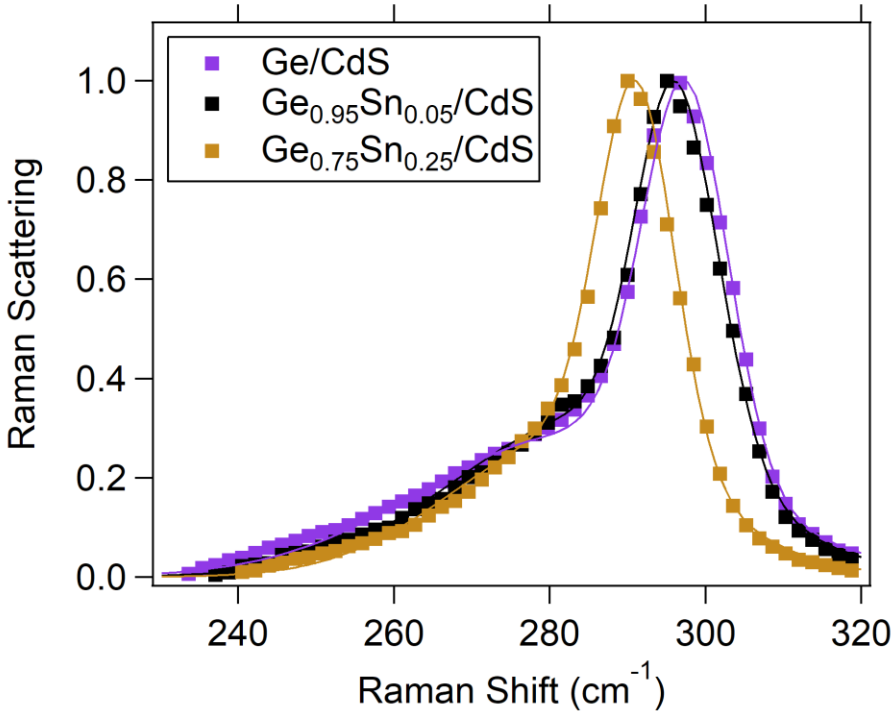

Figure S6. Raman spectra of the $Ge_{1-x}Sn_x$/CdS core/shell nanocrystals.

Table S1. Summary of Raman peak locations of the Ge-Ge LO and SO phonon modes for the Ge and $Ge_{1-x}Sn_x$ nanocrystals and core/shell nanocrystals. Each value is an average of 5 replicate measurements. All 5 replicate spectra were fit to 2-peak Gaussian curves to account for asymmetry due to the SO phonon appearing at lower wavenumbers, and the values were subsequently averaged to produce these data.

Sample	Longitudinal Optical Phonon Mode		Surface Optical Phonon Mode	
	Location (cm^{-1})	FWHM (cm^{-1})	Location (cm^{-1})	FWHM (cm^{-1})
Ge cores	296.4 ± 0.4	11.4 ± 0.6	283.0 ± 0.6	47 ± 4
$Ge_{0.95}Sn_{0.05}$	295.2 ± 0.5	13 ± 3	283 ± 2	60 ± 10
$Ge_{0.75}Sn_{0.25}$	292 ± 1	19 ± 3	280 ± 10	60 ± 10
Ge/CdS	297.5 ± 0.5	12.7 ± 0.5	283 ± 1	47 ± 2
$Ge_{0.95}Sn_{0.05}$/CdS	295 ± 1	10.6 ± 0.9	286 ± 1	36.9 ± 0.6
$Ge_{0.75}Sn_{0.25}$/CdS	291.1 ± 0.5	11.5 ± 0.6	282.8 ± 0.6	36.4 ± 0.7

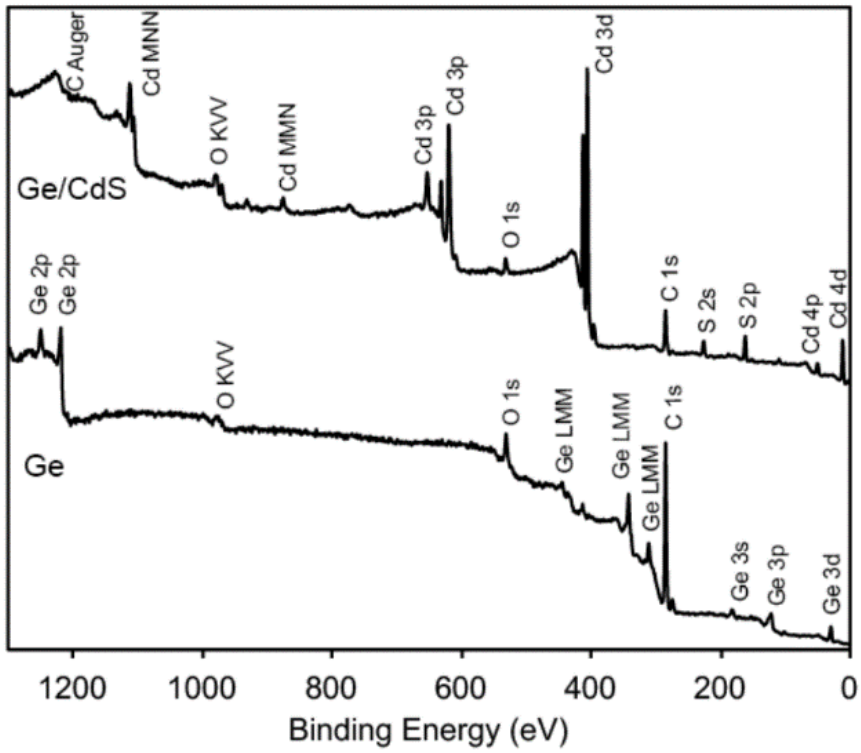
C Auger
Cd MNN
O KVV
Cd MMN
Cd 3p
Cd 3p
Cd 3d
O 1s
C 1s
S 2s
S 2p
Cd 4p
Cd 4d
Ge/CdS
Ge 2p
Ge 2p
O KVV
O 1s
Ge LMM
Ge LMM
Ge LMM
C 1s
Ge 3s
Ge 3p
Ge 3d
Ge
1200
1000
800
600
400
200
0
Binding Energy (eV)

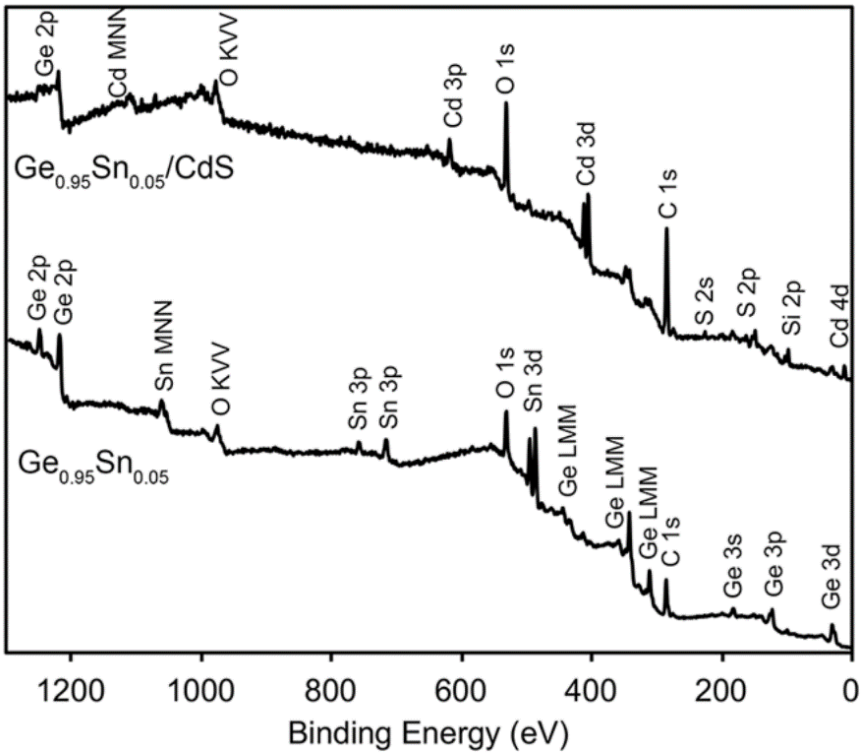
Ge 2p
Cd MNN
O KVV
Cd 3p
O 1s
Cd 3d
C 1s
S 2s
S 2p
Si 2p
Cd 4d
Ge0.95Sn0.05/CdS
Ge 2p
Ge 2p
Sn MNN
O KVV
Sn 3p
Sn 3p
O 1s
Sn 3d
Ge LMM
Ge LMM
Ge LMM
C 1s
Ge 3s
Ge 3p
Ge 3d
Ge0.95Sn0.05
1200
1000
800
600
400
200
0
Binding Energy (eV)

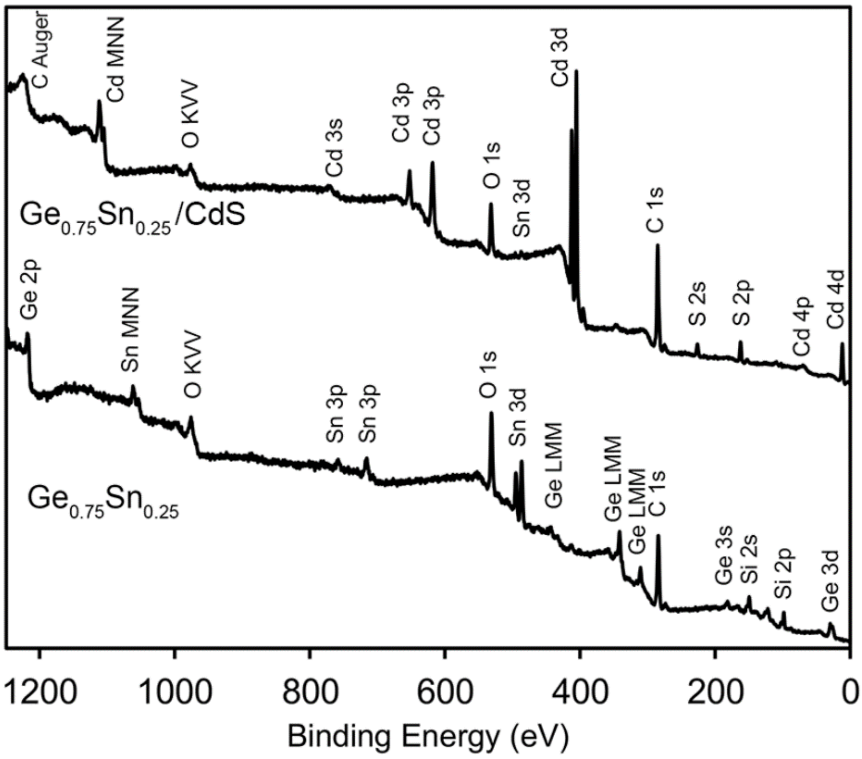

Figure S7. XPS survey spectra for Ge and $Ge_{1-x}Sn_x$ core and core/shell nanocrystals. Samples indicated at the lower left of each trace.

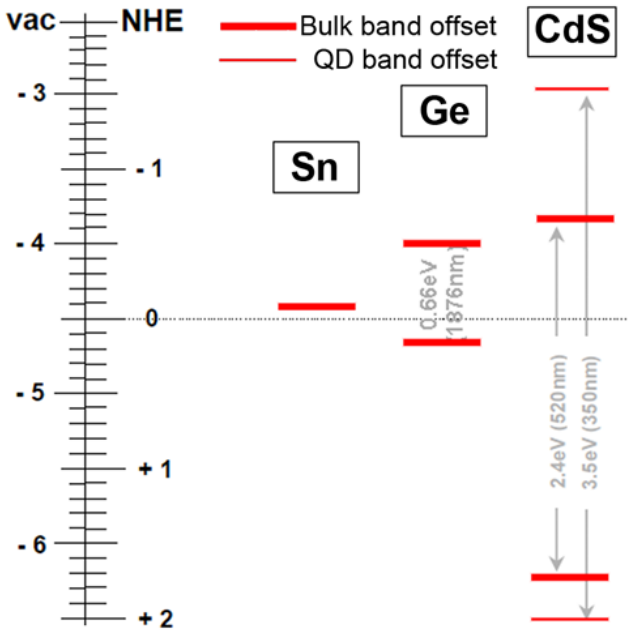

Figure S8. Plot of valence and conduction band offsets for Ge, Sn, and CdS.

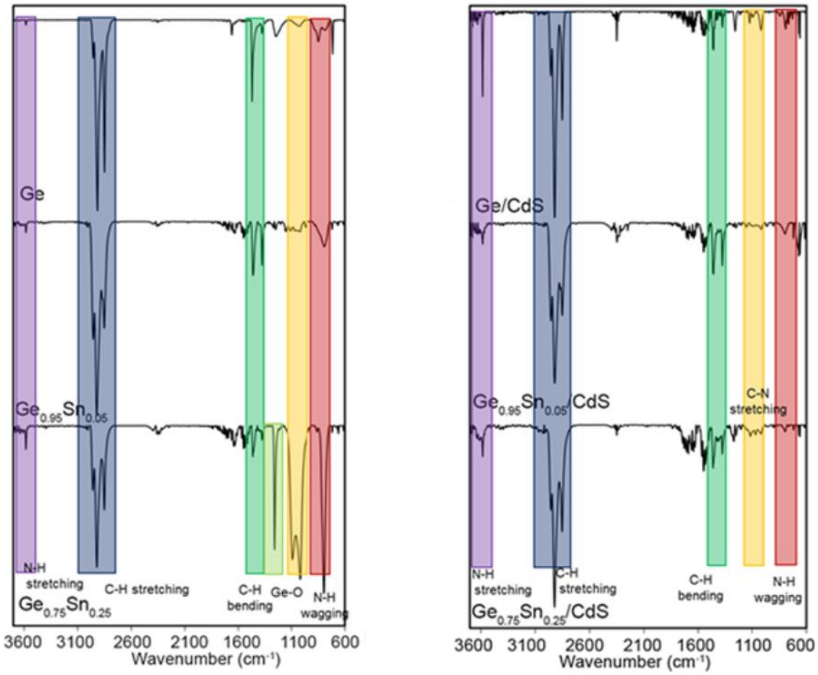

Figure S9. Fourier transform infrared spectra of Ge and $Ge_{1-x}Sn_x$ core (left) and core/shell (right) nanocrystals. Note the intense Ge-O band in the $Ge_{0.75}Sn_{0.25}$ sample, corresponding to increased oxidation in that sample. In another set of experiments no oxidation was measured in the $Ge_{0.75}Sn_{0.25}$ sample as explained in the text.

CHAPTER 3. UNVEILING THE PHOTO- AND THERMAL-STABILITY OF CESIUM LEAD HALIDE PEROVSKITE NANOCRYSTALS

Brett W. Boote, Himashi P. Andaraarachchi, Bryan A. Rosales, Feng Zhu, Malinda D. Reichert, Kalyan Santra, Jingzhe Li, Jacob W. Petrich, Javier Vela, Emily A. Smith*

Modified from a manuscript submitted to *ChemPhysChem*.

Affiliations

The Ames Laboratory, U.S. Department of Energy, and Department of Chemistry, Iowa State University, Ames, Iowa 50011-3111, United States

Abstract

Lead halide perovskites possess unique characteristics that are well-suited for optoelectronic and energy capture devices, however, concerns about their long-term stability remain. Limited stability is often linked to the methylammonium cation, and all-inorganic $CsPbX_3$ (X = Cl, Br, I) perovskite nanocrystals have been reported with improved stability. In this work, the photostability and thermal stability properties of $CsPbX_3$ (X = Cl, Br, I) nanocrystals were investigated via electron microscopy, x-ray diffraction, thermogravimetric analysis coupled with FTIR (TGA-FTIR), ensemble and single particle spectral characterization. $CsPbBr_3$ was found to be stable under 1-sun illumination for 16 h in ambient conditions, although single crystal luminescence analysis after illumination via a solar simulator indicates that the luminescence states are changing over time. $CsPbBr_3$ was also stable to heating to 250 °C. Large $CsPbI_3$ crystals (34 ± 5

nm) were shown to be the least stable composition under the same conditions as both XRD reflections and Raman bands diminish under irradiation; and with heating the γ (black) phase reverts to the non-luminescent δ phase. Smaller $CsPbI_3$ nanocrystals (14 ± 2 nm) purified by a different washing strategy exhibited improved photostability with no evidence of crystal growth but were still thermally unstable. Both $CsPbCl_3$ and $CsPbBr_3$ show crystal growth under irradiation or heat, likely with a preferential orientation based on XRD patterns. TGA-FTIR revealed nanocrystal mass loss was only from liberation and subsequent degradation of surface ligands. Encapsulation or other protective strategies should be employed for long-term stability of these materials under conditions of high irradiance or temperature.

Introduction

The unique photophysical properties and straightforward synthesis of perovskite-based materials make them promising materials for solar energy applications.[5, 20, 135-136] The first-generation methylammonium lead halide ($MAPbX_3$) perovskites have been shown to degrade rapidly when exposed to ambient conditions with moderate humidity,[137] which led to the increased study of new compositions such as the all-inorganic cesium lead halide ($CsPbX_3$) perovskites. $CsPbX_3$ nanocrystals have been incorporated into solar cells achieving a record 13.4% power conversion efficiency (PCE).[7, 138-141] In addition to light absorption or conversion for energy capture, these materials have been reported for possible use in laser media,[142-145] LEDs,[2, 19, 146-147] and photodetectors.[18, 143, 148]

Most reported syntheses of $CsPbX_3$ follow the work of Protesescu *et al*. who demonstrated a simple, solution-based synthesis for nanocrystals with high luminescence.[2] Other syntheses have expanded this general idea by generating multiple nanocrystal morphologies through ligand mediation[149-150] and reaction tuning,[21] by using different surface ligands for improved quantum yields,[8, 151] by increasing surface passivation/repair via salt solutions,[152-155] as well as by generating other cation/anion compositions through doping[12, 16, 22, 146, 156-158] or post-synthetic ion exchange.[13, 18, 150, 159-161] In addition, triple-cation (Cs,formamidinium,methylammonium)PbX_3 materials have been developed with the goal of increasing stability while maintaining bright luminescence.[152, 162]

The photophysics of $MAPbX_3$ nanocrystals have been extensively studied,[163-172] and there are several reports on various luminescence properties of $CsPbX_3$.[17, 173-175] Park *et al*. observed strong photon antibunching as well as blinking behavior ascribed to charge/discharge events triggered by photoionization in $CsPbBr_3$ and $CsPbI_3$.[174] Recently, Becker *et al.* showed the lowest triplet exciton for $CsPbX_3$ is bright, which explains the anomalously fast emission rates for these materials compared to other semiconductors.[176] Pan *et al.* first demonstrated lanthanide doping into $CsPbCl_3$, showing improved quantum yield and luminescence bands across the visible and even into the near-IR region.[177] Both transition metals[12, 178] and rare earth metals[158] have been doped into $CsPbX_3$, achieving quantum yields greater than 60% and 170%, respectively. Beimborn *et al.* studied the effect of pressure-induced deformation on the photoluminescence, which leads to a fully reversible blue shift with decreasing intensity.[179] Raino and coworkers observed suppressed blinking and a fast decay from low-temperature (6 K) photoluminescence

measurements of $CsPbCl_xBr_{3-x}$ nanocrystals.[17] In contrast, Diroll *et al.* studied high temperature photoluminescence of $CsPbX_3$ nanocrystals (up to 550 K), showing reversible photoluminescence loss below 450 K for $CsPbBr_3$ (the highest threshold among the compositions studied).[173]

Since $CsPbX_3$ materials have considerable potential for use in functional devices, the stability of their nanocrystals is of utmost importance. $CsPbCl_3$ and $CsPbBr_3$ nanocrystals are reported to be stable in the cubic phase, while $CsPbI_3$ slowly reverts to the thermodynamically-favored δ-phase, which is yellow.[2] This phase change is accelerated with harsh washing reagents and, with a more gentle washing strategy—using methyl acetate or MeOAc—$CsPbI_3$, is stable in the γ (black) phase for over 2 months.[180] Importantly, the δ phase for $CsPbI_3$ is non-luminescent, rendering the material unusable for most applications. Park *et al.* observe a 16-nm blue shift and eventual degradation in $CsPbI_3$ nanocrystals that were caused by the irreversible generation of surface defects during photoluminescence measurements.[174] Liu and coworkers compare $CsPbI_3$ nanocrystals stabilized with trioctylphosphine (TOP) to those stabilized with oleic acid and oleylamine.[151] They found the TOP-stabilized nanocrystals show improved quantum yield, and are stable for at least one month under ambient conditions. When dry films of the nanocrystals are prepared, however, the common δ-$CsPbI_3$ phase transition is observed after 3 days. Yuan *et al.* demonstrated that $CsPbI_3$ nanocrystals undergo irreversible photodegradation that quenches the photoluminescence under light irradiation.[175] For films in air, photobrightening followed by photodegradation was observed under illumination, and degradation is also observed for films in dark, ambient conditions. Additionally, several groups have been developing methods of protecting the

perovskite structure from moisture, including overlaying silicone resins,[181] preparing polymer or related composites,[182-184] and coating with zwitterion[185] or metal complexes.[146, 186]

A recent report by Liao *et al.* describes the thermal stability of cesium lead halide perovskites from -190 to 500 °C using Raman spectroscopy and XRD.[187] They found that $CsPbCl_3$ nanocrystals were the most thermally stable among (X=Cl, Br, I) compositions, as $CsPbBr_3$ and $CsPbI_3$ nanocrystals decomposed at ~400 and 200 °C, respectively. Though several stability studies have been performed on $CsPbX_3$ nanocrystals, as well as their derived devices,[188] to the best of our knowledge a fundamental study describing how the halide composition of the perovskites affects the photostability and photophysical states of the nanocrystals has not yet been performed. With this work, we set out to understand the connection between the photophysical properties of the $CsPbX_3$ perovskite materials and their stability under conditions likely encountered in many applications, namely light irradiance and thermal stress.

Results and Discussion

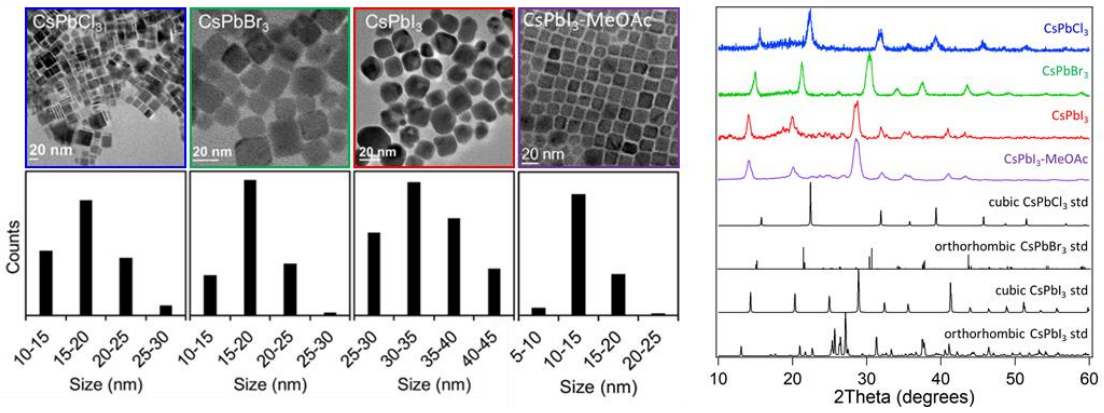

Figure 1. TEM images, size histograms, and XRD patterns for cesium lead perovskite nanocrystals.

General Characterization and Photophysical Properties of $CsPbX_3$ Nanocrystals

Cesium lead halide perovskite nanocrystals were prepared via a modified literature method[2] with the goal of understanding their photophysical properties as well as their photostabilty and thermal stability. **Figure 1** shows electron microscopy images, size histograms, and XRD patterns for the cesium lead halide nanocrystals. In general, the nanocrystals exhibit cubic morphology, although the $CsPbCl_3$ sample also showed evidence of platelets/stacking. When using identical synthetic conditions, the $CsPbI_3$ sample always formed larger nanocrystals than the other compositions after washing with acetone/methanol. The sizes of the nanocrystals washed with acetone/methanol were 17 ± 3 nm for $CsPbCl_3$, 17 ± 4 nm for $CsPbBr_3$, and 34 ± 5 nm for $CsPbI_3$. The size difference should not have a pronounced effect on the nanocrystal photophysics as all of these sizes are above the Bohr radii for $CsPbX_3$ nanocrystals. In an effort, however, to isolate $CsPbI_3$ nanocrystals of a smaller size, another sample of crystals was washed with methyl acetate. The methyl acetate washed $CsPbI_3$ nanocrystals had a size of 14 ± 2 nm, similar to the acetone/methanol washed $CsPbCl_3$ and $CsPbBr_3$ nanocrystals.[180] While the size of the nanocrystals are similar, the surface chemistry can vary due to the different wash procedures, thus becoming another variable that may affect the photophysics and stability. For clarity, the methyl acetate washed sample will be labeled $CsPbI_3$-MeOAc. The TEM images of $CsPbI_3$-MeOAc show nearly ideal cubic morphologies, which is consistent with highly crystalline surfaces. The XRD patterns of the nanocrystals are consistent with cubic standard patterns, although previous work on $CsPbX_3$ nanocrystals using Rietveld refinement has shown the PbX_6 octahedra can undergo dynamic distortions and rotations that lead to disorder and a resultant orthorhombic γ-phase for both $CsPbBr_3$ and $CsPbI_3$.[189-190]

Solution absorption and photoluminescence spectra for the nanocrystals are shown in **Figure 2**. The photoluminescence λ_{max} data are consistent with literature values for these materials and are 413, 523, 698, and 687 nm for $CsPbCl_3$, $CsPbBr_3$, $CsPbI_3$, and $CsPbI_3$-MeOAc, respectively.[2] Photoluminescence decay curves (**Figure S1**) yield average lifetimes for $CsPbCl_3$, $CsPbBr_3$, and $CsPbI_3$ of 1.2, 2.3, and 41.5 ns, respectively (the $CsPbI_3$-MeOAc sample was not measured). These values are consistent with previous reports,[2] although the $CsPbI_3$ sample showed a slightly longer lifetime, which is likely due to a larger average crystal size for the $CsPbI_3$ nanocrystals.

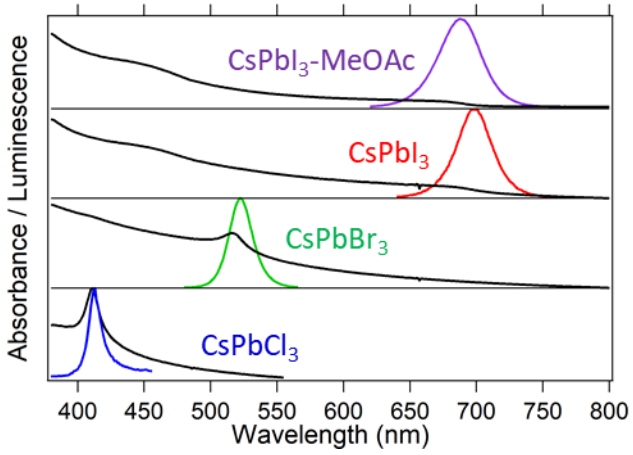

Figure 2. Solution absorption (black) and photoluminescence (color) spectra of the $CsPbX_3$ nanocrystals. The full width at half maximum values were 13, 22, 33, and 40 nm for $CsPbCl_3$, $CsPbBr_3$, $CsPbI_3$, and $CsPbI_3$-MeOAc, respectively.

To assess the photophysics of the perovskite nanocrystals further, single particle luminescence data were recorded for individual $CsPbBr_3$, $CsPbI_3$, and $CsPbI_3$-MeOAc nanocrystals. For the $CsPbCl_3$ sample, the signal-to-noise ratio (SNR) was too low for quantification of the luminescence from single crystals, as shown by representative images from luminescence movies (**Figure S2**). This could be due to the presence of platelets in this sample, which has been shown to lead to more defects within the material due to a high surface area, and thus lower luminescence intensity.[191] The

photoluminescence traces for $CsPbBr_3$, $CsPbI_3$ and $CsPbI_3$-MeOAc nanocrystals were categorized into constant- (intensity not significantly changing), photobleaching- (decreasing intensity), photobrightening- (increasing intensity), and bimodal- (two distinct intensity levels) luminescence types. Full information on the categories and mathematical treatment is available in Supporting Information, with resultsshown in **Figure S3**. In general, the nanocrystals from each halide composition spend the majority of the time in the ON state, regardless of luminescence type. The $CsPbBr_3$, $CsPbI_3$, and $CsPbI_3$-MeOAc nanocrystals were on for 87%, 97%, and 99% of the total analysis time, respectively. However, the populations of constant-, photobleaching-, photobrightening-, and bimodal-PL nanocrystals for the same compositions were approximately 4:2:1:1 (Br), 2:2:2:1 (I), and 5:18:1:1 (I-MeOAc) as shown in **Table S1**. Thus, while the $CsPbBr_3$ nanocrystals spend, on average, less total time in the ON state, there is a higher population of nanocrystals with stable luminescence when compared to the iodide-containing samples. $CsPbI_3$ nanocrystals showed similar populations of constant-, photobleaching-, and photobrightening-PL, whereas the $CsPbI_3$-MeOAc nanocrystals showed the highest tendency for photobleaching and had smaller populations with photobrightening- or bimodal-PL behavior. In a previous study on $CH_3NH_3PbI_3$ nanocrystals, photobleaching was the most common luminescence type observed, and this was attributed to increased non-radiative recombination events as a result of the breakdown of the crystal lattice at the surface.[164]

From the single crystal luminescence data, ON-OFF event histograms were extracted and fit to a power law decay and to a 3-exponential decay, using a maximum likelihood method. Maximum likelihood method was used because it has been shown to

provide more accurate fit values when compared to residual minimization in sparse data sets.[192] The results of the ON-OFF fitting are shown in **Figure 3**, and the fit parameters are listed in **Table S1.** Tabulating histograms for single nanocrystals (267 for $CsPbBr_3$, 233 for $CsPbI_3$, and 250 for $CsPbI_3$-MeOAc), the most ON/OFF events were recorded for $CsPbBr_3$ nanocrystals, which had approximately 8× and 50× more total events than those recorded for $CsPbI_3$ and $CsPbI_3$-MeOAc, respectively. This indicates a higher probability of non-radiative recombination centers as a result of surface defects in the $CsPbBr_3$ sample. Interestingly, $CsPbI_3$-MeOAc nanocrystals have the longest lived ON state, and very few recorded OFF events. This is likely due to high crystallinity and reduced surface defects (as shown by near ideal cubic morphologies in TEM images). Comparing the

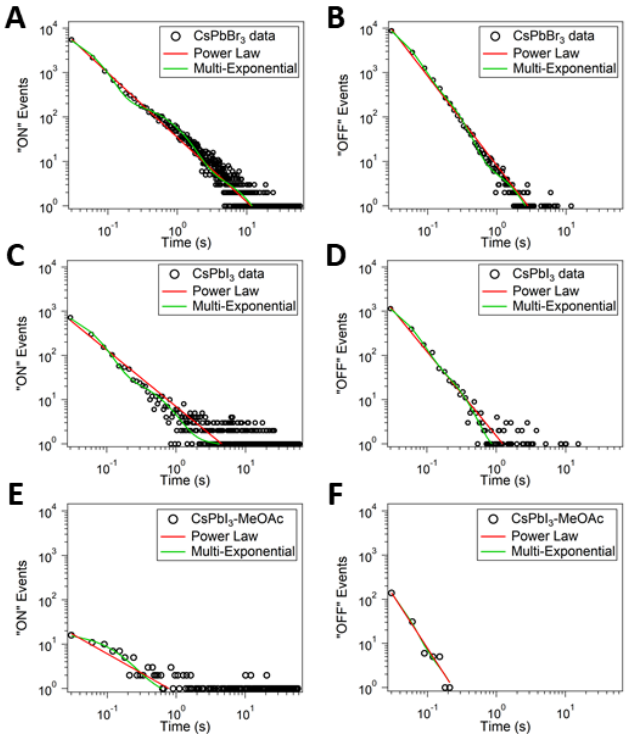

Figure 3. ON-OFF histogram plots of (A, B) $CsPbBr_3$, (C, D) $CsPbI_3$, and (E,F) $CsPbI_3$-MeOAc nanocrystals, based on analysis of 267, 233, and 250 nanocrystals, respectively. The data were fit using maximum likelihood estimation to a power law and a 3-exponential to better fit the non-Gaussian distributions of states.

power law and multi-exponential fits, the power law did not produce a good fit for the $CsPbI_3$ and $CsPbI_3$-MeOAc ON events, whereas the multi-exponential fit shows the tailing (to shorter durations) of the longer lived events. This observation is reminiscent of previous work showing events with longer ON times deviate from power law fits for $CsPbI_3$ nanocrystals.[174] Also, $CsPbI_3$ ON events are longer lived than $CsPbBr_3$, while the OFF states have a similar average duration.

Photostability of $CsPbX_3$ Nanocrystals

To assess nanocrystal photostability, a solar simulator was used to illuminate drop cast nanocrystal films under ambient conditions. XRD patterns of the samples after 2, 4, and 16 h of illumination are shown in **Figure 4**. Also, as a control experiment, a set of samples of each halide composition was kept in the dark under ambient conditions (**Figure S4**), which showed no structural changes over 16 h. $CsPbBr_3$ and $CsPbCl_3$

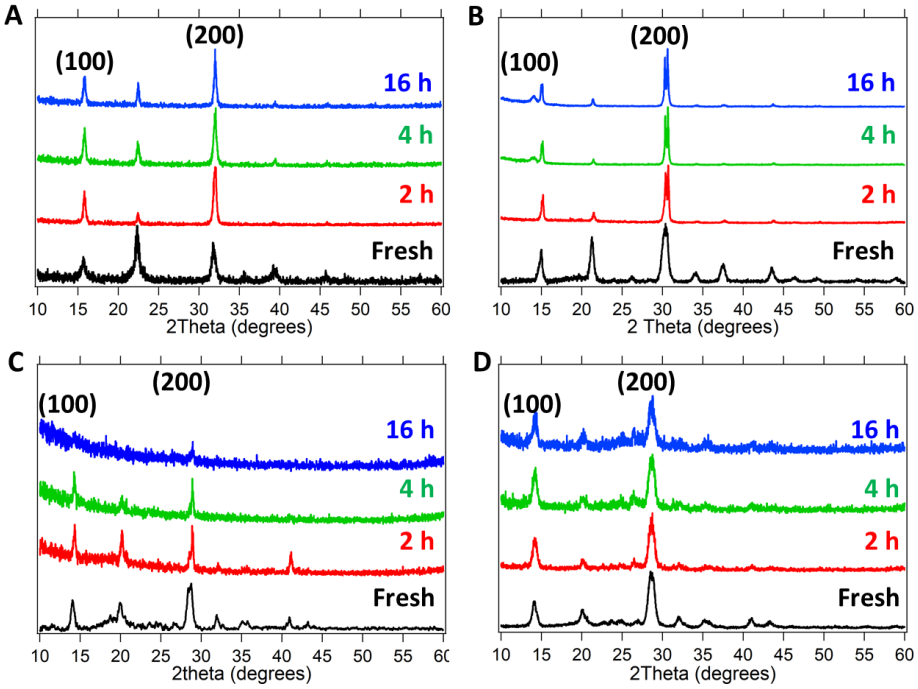

Figure 4. XRD patterns of A) $CsPbCl_3$, B) $CsPbBr_3$, C) $CsPbI_3$, and D) $CsPbI_3$-MeOAc nanocrystals before (fresh) and after exposure to a solar simulator from 2-16 h.

nanocrystals showed enhancement of the (100) and (200) planes, indicating possible orientation effects or anisotropic crystal growth under illumination. Crystal growth is also supported by a decrease in the width of the reflections, which is most evident for the $CsPbBr_3$ sample after 2 h of illumination. The apparent increase in crystal size is enough to elucidate the orthorhombic character of the nanocrystals as seen in the resolved peaks at 15 and 15.2° 2θ, and at 30.4 and 30.7° 2θ. The $CsPbI_3$ nanocrystals showed significant loss of nearly all reflections after 16 h illumination, indicative of sample degradation into non-crystalline products. Interestingly, the $CsPbI_3$-MeOAc sample does not show signs of crystal growth and retains all major reflections of the γ-phase. This indicates that their more ideal crystalline surface improves the photostability of the nanocrystals.

The XRD results are supported by Raman measurements of samples after solar simulator exposure (**Figure S5**). The nanocrystals of different halide compositions have similar Raman spectra, with one main band between 50 and 120 cm^{-1} and a broad response extending to ~200 cm^{-1}. This single broad band (as opposed to sharp, well-defined bands commonly observed in Raman spectra) is likely due to dynamic disorder within the nanocrystals at room temperature.[193] The Raman band intensity increases for both $CsPbCl_3$ and $CsPbBr_3$ up to 120 min of solar simulator exposure, which is consistent with the XRD patterns indicating crystal growth. $CsPbI_3$ is the only sample that degrades over time with solar simulator exposure based on the Raman spectrum.

To monitor the effect of illumination on the photophysical states of the nanocrystals, single crystal luminescence movies were collected on diluted samples after 2 and 4 h of illumination by the solar simulator. The histograms are shown in **Figure 5**, with fit statistics shown in **Table S2**. The $CsPbBr_3$ sample showed the most significant

change after light exposure; ON events were both fewer in number and much shorter in duration. Likewise, OFF events for this sample trended toward longer times while also decreasing in number of occurrences. For the $CsPbI_3$ sample, the ON-OFF histograms after 2 and 4 h solar simulator exposure show very similar characteristics in both number of events and trends for fit parameters, with only slight increases in longer lived states.

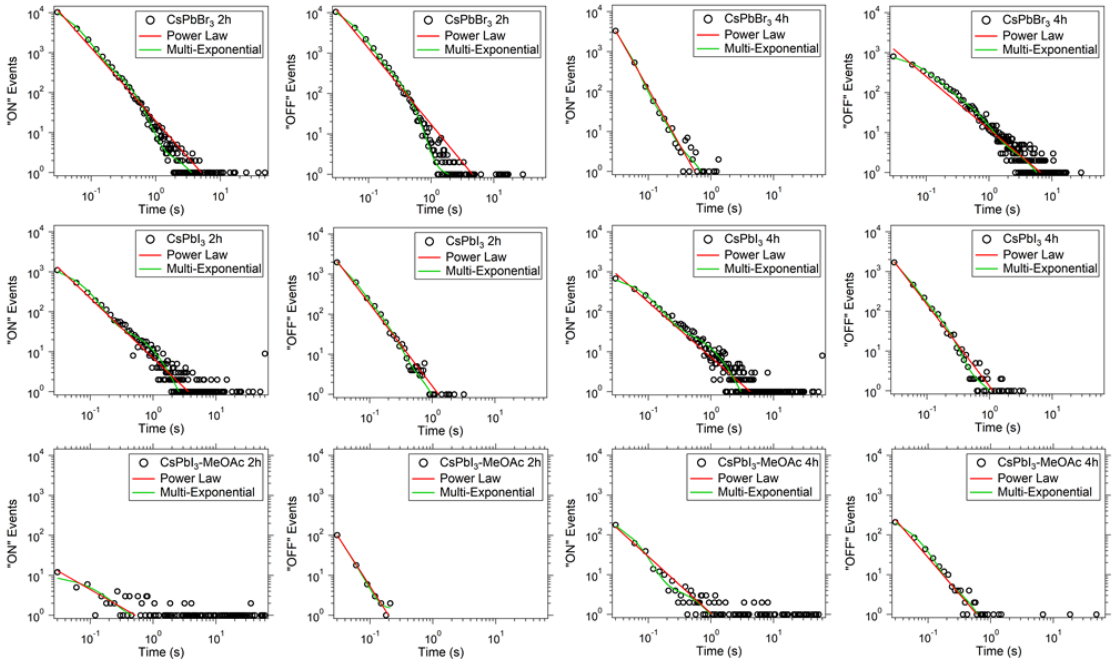

Figure 5. ON-OFF histograms of $CsPbBr_3$, $CsPbI_3$, and $CsPbI_3$-MeOAc nanocrystals following solar simulator exposure for 2 and 4 h. In all samples a minimum of 40 nanocrystals were analyzed to generate the histograms.

Thus, while XRD shows the material eventually degraded after 16 h, the photophysical states do not appear to change over the first 4 h. For the $CsPbI_3$-MeOAc sample, which exhibited few ON-OFF events prior to illumination, the ON-OFF histograms after 2 and 4 h solar simulator exposure show steadily increasing numbers of ON-OFF events, especially OFF events with longer durations. Combining the results from all photostability experiments, the $CsPbBr_3$ and $CsPbI_3$-MeOAc nanocrystals both undergo changes in their luminescence states over time, which is one measure of photo-instability.

Thermal Stability of $CsPbX_3$ Nanocrystals

Even though the photostability is critically important for these materials in downstream applications, for many applications the thermal stability is important as well. In an effort to elucidate the thermal stability and compare to the photostability data of these nanocrystals, thermal stability measurements were performed. A temperature-controlled stage was used to expose drop-cast samples of nanocrystals to elevated temperatures after purging with nitrogen, and then XRD patterns were collected. The XRD patterns for the $CsPbX_3$ perovskite nanocrystals after heating are shown in **Figure 6**. For the three halide compositions, there are three different outcomes as a result of elevated temperatures. $CsPbCl_3$ nanocrystals initially show crystal growth up to 100 °C but show signs of degradation at 250 °C based on the SNR of the XRD pattern. While the cubic phase appears to be degrading, the identity of the degradation product(s) is not revealed by XRD. $CsPbBr_3$ nanocrystals show similar behavior to the photostability measurements upon heating, that is crystal growth leads to a decrease in the width of the reflections and a clear orthorhombic pattern emerges. The crystal structure persisted even up to 250 °C. On the other hand, $CsPbI_3$ nanocrystals undergo a structural change beginning at 50 °C showing a transition from the luminescent γ-phase to a combination of PbI_2 and δ-phase $CsPbI_3$ (which is yellow in color, non-luminescent and thus not viable for devices). By 250 °C, the phase change is essentially complete, and there is a loss of all γ-phase reflections. It is known that the δ-phase is thermodynamically favored,[194] so this result makes sense at the elevated temperature. The $CsPbI_3$-MeOAc sample undergoes a very similar structural change from the γ-phase to the δ-phase above 100 °C. Both $CsPbI_3$ samples show reflections from PbI_2. Dastidar *et al.* showed $CsPbI_3$

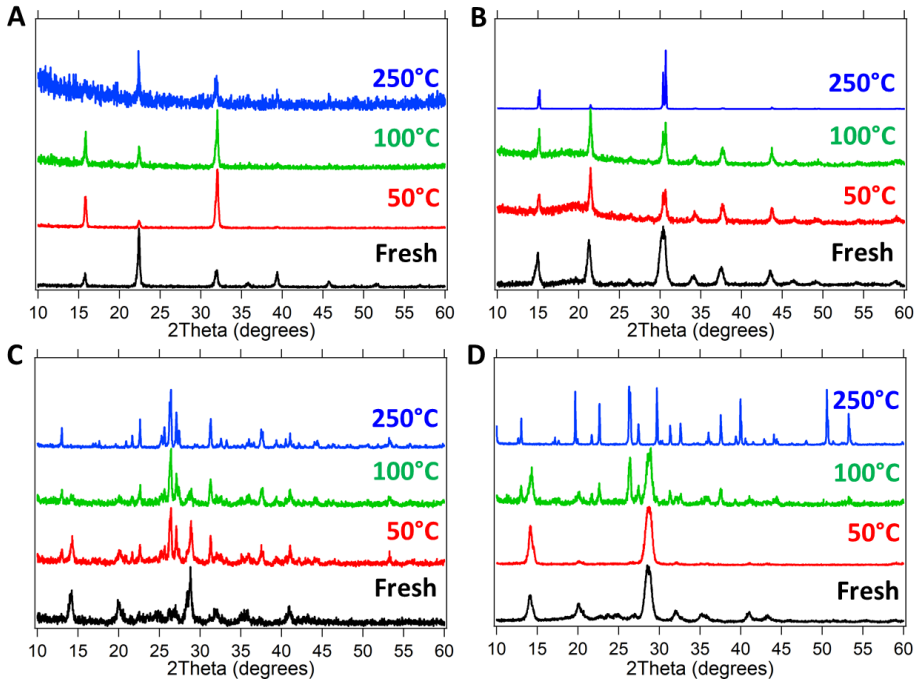

Figure 6. XRD patterns of A) $CsPbCl_3$ B) $CsPbBr_3$ and C) $CsPbI_3$ and D) $CsPbI_3$-MeOAc nanocrystals following exposure to the elevated temperatures shown.

is stable in the cubic phase up to 100 °C in a dry environment, thus our results confirm atmospheric moisture combined with heating accelerate the δ-phase transition.[195] Compared to the samples studied by Liao *et al.* wherein no crystal growth was reported, our $CsPbI_3$ and $CsPbI_3$-MeOAc samples underwent phase changes at lower temperatures and exhibited crystal growth. With the exception of $CsPbI_3$, no clear degradation products are observed in the XRD patterns, so other complementary analysis techniques were employed to explore the possible products of thermal stress.

Raman spectra were acquired for each halide composition at room temperature (21 °C) and then after heating to 250 °C and cooling back to room temperature (**Figure 7**). The high temperature spectra are not shown as the high kinetic energy produces a high background that obscures the Raman signal for all samples. Importantly, $CsPbI_3$ is the only sample that does not recover the original band structure, which would be consistent

with XRD results if the δ-phase has a lower Raman cross section than the γ-phase. The other halides show similar spectra before and after heating, with a slight increase in the band around ~120 cm^{-1} for $CsPbBr_3$. For $CsPbCl_3$, it is curious that the Raman spectrum is retained after heating but the sample appears to be partially degraded in the XRD results. This could be due to the difference in sampling between these techniques: XRD probes a large sample area, whereas Raman spectroscopy is collected on small aggregates that are visible in the microscope image. If the sample degradation starts with single crystals (and there is minimal degradation of aggregates), the Raman spectrum would remain relatively unchanged while the XRD pattern would decrease, as shown in our results.

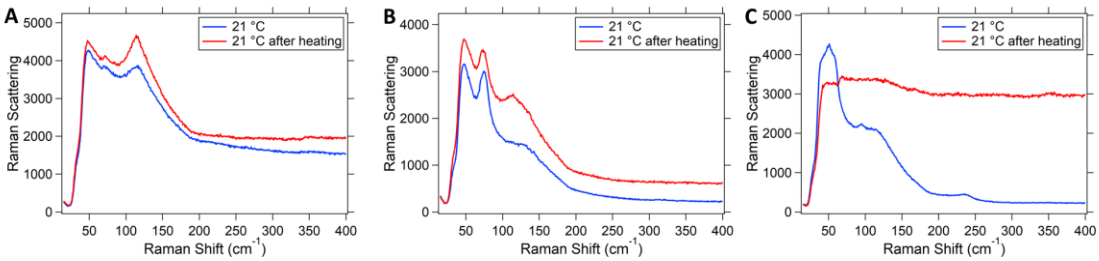

Figure 7. Raman spectra of A) $CsPbCl_3$, B) $CsPbBr_3$, and C) $CsPbI_3$ nanocrystals before and after heating to 250 °C and allowing the samples to cool.

Single crystal luminescence movies could not be collected during heating cycles due to instrument limitations, so solution-phase fluorescence spectra were acquired to observe the effect of temperature on the luminescence band for $CsPbX_3$ nanocrystals (**Figure S6**). In general, an increase in temperature leads to luminescence quenching when the thermal (*kT*) energy approaches the trap state energy.[173] We observe this as well (by comparing the SNR of normalized spectra), along with slight shifts in the luminescence maximum. The $CsPbCl_3$ sample shows a slight red shift as temperature is increased, which appears to be partially reversible after cooling back to room

temperature. For $CsPbBr_3$ and $CsPbI_3$, slight blue shifts are observed with heating, however, $CsPbBr_3$ does not shift back upon cooling, indicating an irreversible process occurred. In contrast, $CsPbI_3$ completely recovers the original luminescence maximum. Irreversible processes typically involve changes within the material, while reversible processes involve changes to surface states.[173]

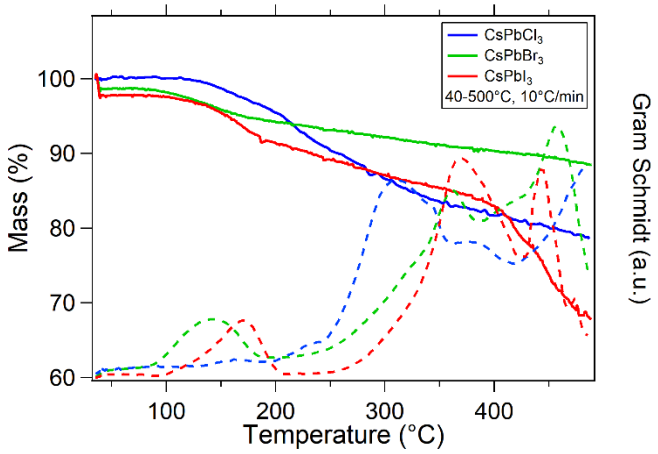

Figure 8. TGA-FTIR Mass loss and Gram-Schmidt curves for $CsPbX_3$ nanocrystals from 40-500 °C. The Gram-Schmidt curves monitor the total change in FTIR signal over time, indicating FTIR detection of mass loss products.

The thermal decomposition products were further analyzed with TGA-FTIR measurements and the results are shown in **Figure 8**. In addition to mass loss plots, the Gram-Schmidt curves for each sample are shown as well, which represent the total change in the FTIR signal based on successive measurements. In all samples, the mass loss from roughly 100-200 °C corresponded with oleylamine and oleic acid surface ligands, while the rest of the mass loss above 250 °C is due to CO_2, which can be from reaction and breakdown of the surface ligands with the O_2 from the 80% N_2 and 20% O_2 gas flow used in these measurements. Though octadecene is present in the reaction as well, it has been shown that oleic acid and oleylamine are the binding surface ligands, and the chemistry at the surface of these crystals is dynamic and cooperative.[196-197] These

results are similar to recent reports showing TGA measurements of $CsPbI_3$,[195] $CsPbBr_3$,[198] and Mn^{2+}-doped $CsPbCl_3$.[16] In the case of $CsPbI_3$, the previous report indicates the bulk material begins to degrade above 400 °C, which helps explain the rapid mass loss we observed for nanocrystals of the same composition. Representative FTIR spectra (**Figure S7)** show the surface ligands and CO_2 signal measured at selected temperatures. In all cases, no gaseous loss products are detected that contain cesium, lead, or the halide species.

Conclusions

The halide composition of the $CsPbX_3$ nanocrystals has a significant effect on their stability. While exhibiting bright luminescence and good photostability, $CsPbI_3$-MeOAc nanocrystals are the most prone to degradation under heating. $CsPbI_3$ nanocrystals exhibit the most stable photophysical states by single crystal luminescence analysis, but eventually degrade under light and readily degrade under heating. $CsPbBr_3$ nanocrystals are the most resilient to degradation, though the photophysical states appear to change based on single crystal luminescence analysis during illumination in ambient conditions, which does represent photo-instability. $CsPbCl_3$ showed good stability under illumination and at elevated temperature, with possible crystal growth or orientation effects observed during illumination. While the smaller $CsPbI_3$-MeOAc nanocrystals show improved photostability compared to larger $CsPbI_3$ nanocrystals, it is also possible that surface chemistry differences in these two samples produce some or all of this effect. Additional experiments will be informative in unravelling which has the more dominant effect. Substituting Cs^+ in place of the methylammonium cation improves the stability for all compositions based on a comparison to published data,[139] although surface protection

or encapsulation is still necessary for long-term downstream applications of $CsPbX_3$ nanocrystals in high-light-irradiance or elevated temperature environments.

Experimental Section

Materials

Lead chloride ($PbCl_2$, 99%), lead bromide ($PbBr_2$, 99%), lead iodide (PbI_2, 99%), 1-octadecene (ODE, 90%), oleic acid (OA, 90%), oleylamine (OLA, 80-90%), and cesium carbonate (Cs_2CO_3, 99.9%) were purchased from Sigma Aldrich.

Preparation of the Nanocrystals

$CsPbX_3$ nanocrystals were synthesized using a modified literature procedure.[2] Briefly, PbX_2 (0.188 mol), $PbCl_2$ (0.087 g), $PbBr_2$ (0.069 g), PbI_2 (0.052 g), was added to an oven-dry three-neck 250 mL flask containing ODE (5 mL), oleic acid (0.5 mL), and oleylamine (0.5 mL). The contents were degassed at 80 °C for 1 h and the flask was refilled with Ar and heated to 150 °C. A Cs-oleate solution (0.4 mL, 0.125 M in ODE) prepared by dissolving Cs_2CO_3 (2.49 mmol, 0.814g) in 40 mL of ODE was quickly injected, and 5 s later the reaction mixture was cooled by an ice-water bath. The nanocrystals were purified by crashing two times with 1:1 (v/v) acetone/methanol solution and centrifugation at 4500 rpm for 5 min followed by redispersion in 5 mL of toluene. In the case of $CsPbI_3$, purification was also carried out using methyl acetate in order to generate smaller nanocrystals, following the work of Swarnkar *et al*,[180] subsequently referred to as $CsPbI_3$-MeOAc.

Transmission electron microscopy (TEM) was performed using a Tecnai G2 F20 field emission TEM instrument (FEI, Hillsboro, OR) operating at ≤200 kV. Samples were prepared by placing 1 or 2 drops of concentrated toluene solutions onto carbon-coated

copper grids. Powder X-ray diffraction (XRD) was measured using Cu Kα radiation on an Ultima IV diffractometer (Rigaku, The Woodlands, TX). The scanning range was 10-60° 2θ, with a step size of 0.02°.

Optical Characterization

Solution extinction (absorption plus scattering) spectra were measured using a photodiode array 8453 UV-Vis spectrophotometer (Agilent, Santa Clara, CA). Steady-state photoluminescence (PL) spectra were measured using a Nanolog scanning spectrofluorometer (HORIBA Scientific, Edison, NJ) equipped with a liquid nitrogen-cooled InGaAs photodiode array. The excitation wavelength was 350 nm for $CsPbCl_3$ and $CsPbBr_3$, and 500 nm for $CsPbI_3$.

Single crystal photoluminescence movies were recorded on an Eclipse 80*i* upright microscope (Nikon Instruments, Melville, NY) fitted with a 100× (1.49 NA) oil immersion objective. An Xcite 120 PC mercury lamp was used for excitation (EXPO Photonic Solutions, Quebec City, Quebec, Canada). The nanocrystals were diluted 1:100 and sonicated for 60 min prior to drop casting onto glass microscope coverslips (Electron Microscopy Sciences, Hatfield, PA). 500 ± 10 nm excitation and 535 ± 15 nm emission filters were used for $CsPbBr_3$, and 510 ± 10 nm excitation and 731 ± 70 nm emission filters were used for $CsPbI_3$. The epi-luminescence was detected by an Evolve EMCCD camera (Photometrics, Tuscon, AZ). PL movies were collected with an acquisition time of 20 ms and a length of 2000 frames, and factoring in readout time the total analysis time was 60 s. The EM gain settings for each sample type were 20× ($CsPbBr_3$), and 1× ($CsPbI_3$), and 5 movies of each sample type were recorded.

Raman microspectroscopy was performed on nanocrystals using an XploRA Plus confocal Raman microscope (HORIBA Scientific, Edison, NJ) fitted with a 100× (0.90

NA) objective. The samples were drop cast onto glass slides and dried under ambient conditions. A 785-nm laser operating at 0.8 mW (~2×10^4 W/cm^2) was used for excitation with an edge filter, allowing for data collection down to 40 cm^{-1}. Two accumulations of 60 s each were acquired to exclude cosmic rays. The data were plotted using IGOR 6.37 (WaveMetrics, Portland, OR).

Photostability Study

To assess the photostability of the nanocrystals, a model 10500 compact solar simulator lamp (Abet Technologies, Milford, CT) was used to illuminate drop cast nanocrystal samples. At intervals, Raman spectra and XRD patterns were collected on full-concentration samples, while single crystal luminescence movies and luminescence spectra were collected on 1:100 diluted samples to observe signs of degradation. All measurements were carried out using conditions outlined above.

Thermal Stability Study

For thermal stability measurements, 10 μL of the nanocrystal samples was drop cast onto cover glass and was allowed to dry for 30 min. A THMS600 temperature stage equipped with a LNP95 liquid nitrogen pump (Linkam Scientific Instruments, Tadworth, UK) was used to heat the samples after purging with nitrogen, using a ramp rate of 40 °C/min and allowing 30 min stabilization time for temperature changes. For Raman spectra, a 50× (0.5 NA) long working distance objective was used, acquiring spectra at room temperature, then 250 °C, then after cooling back to room temperature. XRD patterns were collected for samples heated to 50, 100, and 250 °C with stabilization periods of 5 min after being resuspended in toluene and drop casted onto a silicon XRD sample holder.

Thermogravimetric analysis coupled with FTIR (TGA-FTIR) was performed on an STA449F1 TGA/DSC System (Netzsch, Selb, Germany) using Al_2O_3 crucibles. The temperature program was an isothermal step at 40 °C for 5 min followed by a 10 °C/min ramp from 40-500 °C. The purge gases were set to 10 mL/min high purity N_2, 10 mL/min high-purity O_2, and 30 mL/min high-purity N_2 on the protective line to simulate air while maintaining low residual H_2O in the furnace. The system was coupled to a Tensor 10 FTIR (Bruker, Billerica, MA) equipped with a TGA-IR temperature controlled 10 cm lightpipe sample stage set to 200 °C, and transfer lines were also kept at 200 °C. 1-2 mg of nanocrystals were deposited in the crucibles for analysis.

Acknowledgements

This research is supported by the U.S. Department of Energy, Office of Basic Energy Sciences, Division of Chemical Sciences, Geosciences, and Biosciences through the Ames Laboratory. Electron microscopy characterization was performed at Ames Laboratory's Sensitive Instrument Facility. Ames Laboratory is operated for the U.S. Department of Energy by Iowa State University under contract # DE-AC02-07CH11358.

References

2. Protesescu, L.; Yakunin, S.; Bodnarchuk, M. I.; Krieg, F.; Caputo, R.; Hendon, C. H.; Yang, R. X.; Walsh, A.; Kovalenko, M. V., Nanocrystals of Cesium Lead Halide Perovskites ($CsPbX_3$, X= Cl, Br, and I): Novel Optoelectronic Materials Showing Bright Emission with Wide Color Gamut. *Nano Letters* **2015,** *15* (6), 3692-3696.

5. Akkerman, Q. A.; Rainò, G.; Kovalenko, M. V.; Manna, L., Genesis, Challenges and Opportunities for Colloidal Lead Halide Perovskite Nanocrystals. *Nature Materials* **2018,** *17*, 394-405.

7. Sanehira, E. M.; Marshall, A. R.; Christians, J. A.; Harvey, S. P.; Ciesielski, P. N.; Wheeler, L. M.; Schulz, P.; Lin, L. Y.; Beard, M. C.; Luther, J. M., Enhanced Mobility $CsPbI_3$ Quantum Dot Arrays for Record-Efficiency, High-Voltage Photovoltaic Cells. *Science Advances* **2017,** *3* (10), eaao4204.

8. Lu, C.; Li, H.; Kolodziejski, K.; Dun, C.; Huang, W.; Carroll, D.; Geyer, S. M., Enhanced stabilization of inorganic cesium lead triiodide (CsPbI 3) perovskite quantum dots with tri-octylphosphine. *Nano Research* **2018,** *11* (2), 762-768.

12. Bi, C.; Wang, S.; Li, Q.; Kershaw, S. V.; Tian, J.; Rogach, A. L., Thermally Stable Copper (II) Doped Cesium Lead Halide Perovskite Quantum Dots with a Strong Blue Emission. *The journal of physical chemistry letters* **2019**.

13. Chen, Y.-C.; Chou, H.-L.; Lin, J.-C.; Lee, Y.-C.; Pao, C.-W.; Chen, J.-L.; Chang, C.-C.; Chi, R.-Y.; Kuo, T.-R.; Lu, C.-W., Enhanced Luminescence and Stability of Cesium Lead Halide Perovskite CsPbX3 Nanocrystals by Cu2+-Assisted Anion Exchange Reactions. *The Journal of Physical Chemistry C* **2019,** *123* (4), 2353-2360.

16. Mir, W. J.; Jagadeeswararao, M.; Das, S.; Nag, A., Colloidal Mn-doped Cesium Lead Halide Perovskite Nanoplatelets. *ACS Energy Letters* **2017,** *2* (3), 537-543.

17. Rainò, G.; Nedelcu, G.; Protesescu, L.; Bodnarchuk, M. I.; Kovalenko, M. V.; Mahrt, R. F.; Stöferle, T., Single Cesium Lead Halide Perovskite Nanocrystals at Low Temperature: Fast Single-Photon Emission, Reduced Blinking, and Exciton Fine Structure. *ACS Nano* **2016,** *10* (2), 2485-2490.

18. Ramasamy, P.; Lim, D.-H.; Kim, B.; Lee, S.-H.; Lee, M.-S.; Lee, J.-S., All-Inorganic Cesium Lead Halide Perovskite Nanocrystals for Photodetector Applications. *Chemical Communications* **2016,** *52* (10), 2067-2070.

19. Song, J.; Li, J.; Li, X.; Xu, L.; Dong, Y.; Zeng, H., Quantum Dot Light-Emitting Diodes Based on Inorganic Perovskite Cesium Lead Halides ($CsPbX_3$). *Advanced Materials* **2015,** *27* (44), 7162-7167.

20. Yang, D.; Cao, M.; Zhong, Q.; Li, P.; Zhang, X.; Zhang, Q., All-inorganic cesium lead halide perovskite nanocrystals: synthesis, surface engineering and applications. *Journal of Materials Chemistry C* **2019,** *7* (4), 757-789.

21. Zhang, D.; Eaton, S. W.; Yu, Y.; Dou, L.; Yang, P., Solution-Phase Synthesis of Cesium Lead Halide Perovskite Nanowires. *Journal of the American Chemical Society* **2015,** *137* (29), 9230-9233.

22. Zhu, J.; Yang, X.; Zhu, Y.; Wang, Y.; Cai, J.; Shen, J.; Sun, L.; Li, C., Room-Temperature Synthesis of Mn-Doped Cesium Lead Halide Quantum Dots with High Mn Substitution Ratio. *The Journal of Physical Chemistry Letters* **2017,** *8* (17), 4167-4171.

135. Correa-Baena, J.-P.; Abate, A.; Saliba, M.; Tress, W.; Jacobsson, T. J.; Grätzel, M.; Hagfeldt, A., The Rapid Evolution of Highly Efficient Perovskite Solar Cells. *Energy & Environmental Science* **2017,** *10* (3), 710-727.

136. Swarnkar, A.; Ravi, V. K.; Nag, A., Beyond Colloidal Cesium Lead Halide Perovskite Nanocrystals: Analogous Metal Halides and Doping. *ACS Energy Letters* **2017,** *2* (5), 1089-1098.

137. Bryant, D.; Aristidou, N.; Pont, S.; Sanchez-Molina, I.; Chotchunangatchaval, T.; Wheeler, S.; Durrant, J. R.; Haque, S. A., Light and Oxygen Induced Degradation Limits the Operational Stability of Methylammonium Lead Triiodide Perovskite Solar Cells. *Energy & Environmental Science* **2016,** *9* (5), 1655-1660.

138. Beal, R. E.; Slotcavage, D. J.; Leijtens, T.; Bowring, A. R.; Belisle, R. A.; Nguyen, W. H.; Burkhard, G. F.; Hoke, E. T.; McGehee, M. D., Cesium Lead Halide Perovskites With Improved Stability for Tandem Solar Cells. *The Journal of Physical Chemistry Letters* **2016,** *7* (5), 746-751.

139. Kulbak, M.; Gupta, S.; Kedem, N.; Levine, I.; Bendikov, T.; Hodes, G.; Cahen, D., Cesium Enhances Long-term Stability of Lead Bromide Perovskite-based Solar Cells. *The Journal of Physical Chemistry Letters* **2015,** *7* (1), 167-172.

140. Sutton, R. J.; Eperon, G. E.; Miranda, L.; Parrott, E. S.; Kamino, B. A.; Patel, J. B.; Hörantner, M. T.; Johnston, M. B.; Haghighirad, A. A.; Moore, D. T., Bandgap-Tunable Cesium Lead Halide Perovskites with High Thermal Stability for Efficient Solar Cells. *Advanced Energy Materials* **2016,** *6* (8), 1502458.

141. Wang, K.; Jin, Z.; Liang, L.; Bian, H.; Bai, D.; Wang, H.; Zhang, J.; Wang, Q.; Liu, S., All-inorganic cesium lead iodide perovskite solar cells with stabilized efficiency beyond 15%. *Nature Communications* **2018,** *9* (1), 4544.

142. Eaton, S. W.; Lai, M.; Gibson, N. A.; Wong, A. B.; Dou, L.; Ma, J.; Wang, L.-W.; Leone, S. R.; Yang, P., Lasing in Robust Cesium Lead Halide Perovskite Nanowires. *Proceedings of the National Academy of Sciences* **2016,** *113* (8), 1993-1998.

143. Wang, S.; Wang, K.; Gu, Z.; Wang, Y.; Huang, C.; Yi, N.; Xiao, S.; Song, Q., Solution-Phase Synthesis of Cesium Lead Halide Perovskite Microrods for High-Quality Microlasers and Photodetectors. *Advanced Optical Materials* **2017,** *5* (11), 1700023.

144. Wang, X.; Shoaib, M.; Wang, X.; Zhang, X.; He, M.; Luo, Z.; Zheng, W.; Li, H.; Yang, T.; Zhu, X., High-Quality In-Plane Aligned $CsPbX_3$ Perovskite Nanowire Lasers with Composition Dependent Strong Exciton-Photon Coupling. *ACS Nano* **2018,** *12* (6), 6170–6178.

145. Evans, T. J.; Schlaus, A.; Fu, Y.; Zhong, X.; Atallah, T. L.; Spencer, M. S.; Brus, L. E.; Jin, S.; Zhu, X. Y., Continuous-Wave Lasing in Cesium Lead Bromide Perovskite Nanowires. *Advanced Optical Materials* **2018,** *6* (2), 1700982.

146. Lu, M.; Zhang, X.; Bai, X.; Wu, H.; Shen, X.; Zhang, Y.; Zhang, W.; Zheng, W.; Song, H.; Yu, W. W., Spontaneous Silver Doping and Surface Passivation of $CsPbI_3$ Perovskite Active Layer Enable Light-Emitting Devices with an External Quantum Efficiency of 11.2%. *ACS Energy Letters* **2018,** *3*, 1571-1577.

147. Sheng, X.; Chen, G.; Wang, C.; Wang, W.; Hui, J.; Zhang, Q.; Yu, K.; Wei, W.; Yi, M.; Zhang, M., Polarized Optoelectronics of $CsPbX_3$ (X= Cl, Br, I) Perovskite Nanoplates with Tunable Size and Thickness. *Advanced Functional Materials* **2018,** *28* (19), 1800283.

148. Lv, L.; Xu, Y.; Fang, H.; Luo, W.; Xu, F.; Liu, L.; Wang, B.; Zhang, X.; Yang, D.; Hu, W., Generalized Colloidal Synthesis of High-quality, Two-dimensional Cesium Lead Halide Perovskite Nanosheets and Their Applications in Photodetectors. *Nanoscale* **2016,** *8* (28), 13589-13596.

149. Sun, S.; Yuan, D.; Xu, Y.; Wang, A.; Deng, Z., Ligand-Mediated Synthesis of Shape-Controlled Cesium Lead Halide Perovskite Nanocrystals via Reprecipitation Process at Room Temperature. *ACS Nano* **2016,** *10* (3), 3648-3657.

150. Ye, S.; Zhao, M.; Song, J.; Qu, J., Controllable Emission Bands and Morphologies of High-Quality $CsPbX_3$ Perovskite Nanocrystals Prepared in Octane. *Nano Research* **2018,** *11* (9), 4654-4663.

151. Liu, F.; Zhang, Y.; Ding, C.; Kobayashi, S.; Izuishi, T.; Nakazawa, N.; Toyoda, T.; Ohta, T.; Hayase, S.; Minemoto, T., Highly Luminescent Phase-Stable $CsPbI_3$ Perovskite Quantum Dots Achieving Near 100% Absolute Photoluminescence Quantum Yield. *ACS Nano* **2017,** *11* (10), 10373-10383.

152. Abdi-Jalebi, M.; Andaji-Garmaroudi, Z.; Cacovich, S.; Stavrakas, C.; Philippe, B.; Richter, J. M.; Alsari, M.; Booker, E. P.; Hutter, E. M.; Pearson, A. J., Maximizing and stabilizing luminescence from halide perovskites with potassium passivation. *Nature* **2018,** *555* (7697), 497.

153. Ahmed, T.; Seth, S.; Samanta, A., Boosting the Photoluminescence of CsPbX3 (X= Cl, Br, I) Perovskite Nanocrystals Covering a Wide Wavelength Range by Postsynthetic Treatment with Tetrafluoroborate Salts. *Chemistry of Materials* **2018,** *30* (11), 3633-3637.

154. Wang, S.; Wang, Y.; Zhang, Y.; Zhang, X.; Shen, X.; Zhuang, X.; Lu, P.; Yu, W. W.; Kershaw, S. V.; Rogach, A. L., Cesium Lead Chloride/Bromide Perovskite Quantum Dots with Strong Blue Emission Realized via a Nitrate-Induced Selective Surface Defect Elimination Process. *The journal of physical chemistry letters* **2018,** *10* (1), 90-96.

155. Bohn, B. J.; Tong, Y.; Gramlich, M.; Lai, M. L.; Döblinger, M.; Wang, K.; Hoye, R. L.; Müller-Buschbaum, P.; Stranks, S. D.; Urban, A. S., Boosting tunable blue luminescence of halide perovskite nanoplatelets through postsynthetic surface trap repair. *Nano letters* **2018,** *18* (8), 5231-5238.

156. Parobek, D.; Dong, Y.; Qiao, T.; Rossi, D.; Son, D. H., Photoinduced Anion Exchange in Cesium Lead Halide Perovskite Nanocrystals. *Journal of the American Chemical Society* **2017,** *139* (12), 4358-4361.

157. Parobek, D.; Roman, B. J.; Dong, Y.; Jin, H.; Lee, E.; Sheldon, M.; Son, D. H., Exciton-to-dopant Energy Transfer in Mn-doped Cesium Lead Halide Perovskite Nanocrystals. *Nano Letters* **2016,** *16* (12), 7376-7380.

158. Milstein, T.; Kroupa, D.; Gamelin, D. R., Picosecond Quantum Cutting Generates Photoluminescence Quantum Yields Over 100% in Ytterbium-Doped $CsPbCl_3$ Nanocrystals. *Nano Letters* **2018,** *18* (6), 3792–3799.

159. Akkerman, Q. A.; D'Innocenzo, V.; Accornero, S.; Scarpellini, A.; Petrozza, A.; Prato, M.; Manna, L., Tuning the Optical Properties of Cesium Lead Halide Perovskite Nanocrystals by Anion Exchange Reactions. *Journal of the American Chemical Society* **2015,** *137* (32), 10276-10281.

160. Creutz, S. E.; Crites, E. N.; De Siena, M. C.; Gamelin, D. R., Colloidal Nanocrystals of Lead-Free Double-Perovskite (Elpasolite) Semiconductors: Synthesis and Anion Exchange to Access New Materials. *Nano Letters* **2018,** *18* (2), 1118-1123.

161. Nedelcu, G.; Protesescu, L.; Yakunin, S.; Bodnarchuk, M. I.; Grotevent, M. J.; Kovalenko, M. V., Fast Anion-exchange in Highly Luminescent Nanocrystals of Cesium Lead Halide Perovskites ($CsPbX_3$, X= Cl, Br, I). *Nano Letters* **2015,** *15* (8), 5635-5640.

162. Chen, L.; Tan, Y.-Y.; Chen, Z.-X.; Wang, T.; Hu, S.; Nan, Z.-A.; Xie, L.-Q.; Hui, Y.; Huang, J.-X.; Zhan, C., Toward Long-Term Stability: Single-Crystal Alloys of Cesium-Containing Mixed Cation and Mixed Halide Perovskite. *Journal of the American Chemical Society* **2019,** *141* (4), 1665-1671.

163. Sum, T. C.; Mathews, N., Advancements in Perovskite Solar Cells: Photophysics Behind the Photovoltaics. *Energy & Environmental Science* **2014,** *7* (8), 2518-2534.

164. Freppon, D. J.; Men, L.; Burkhow, S. J.; Petrich, J. W.; Vela, J.; Smith, E. A., Photophysical properties of wavelength-tunable methylammonium lead halide perovskite nanocrystals. *Journal of Materials Chemistry C* **2017,** *5* (1), 118-126.

165. Zhu, F.; Men, L.; Guo, Y.; Zhu, Q.; Bhattacharjee, U.; Goodwin, P. M.; Petrich, J. W.; Smith, E. A.; Vela, J., Shape Evolution and Single Particle Luminescence of Organometal Halide Perovskite Nanocrystals. *ACS Nano* **2015,** *9* (3), 2948-2959.

166. Luo, L.; Men, L.; Liu, Z.; Mudryk, Y.; Zhao, X.; Yao, Y.; Park, J. M.; Shinar, R.; Shinar, J.; Ho, K.-M., Ultrafast Terahertz Snapshots of Excitonic Rydberg States and Electronic Coherence in an Organometal Halide Perovskite. *Nature Communications* **2017,** *8*, 15565.

167. Yuan, H.; Debroye, E.; Caliandro, G.; Janssen, K. P.; Van Loon, J.; Kirschhock, C. E.; Martens, J. A.; Hofkens, J.; Roeffaers, M. B., Photoluminescence Blinking of Single-Crystal Methylammonium Lead Iodide Perovskite Nanorods Induced by Surface Traps. *ACS Omega* **2016,** *1* (1), 148-159.

168. Tian, Y.; Merdasa, A.; Peter, M.; Abdellah, M.; Zheng, K.; Ponseca, C. S., Jr.; Pullerits, T.; Yartsev, A.; Sundstrom, V.; Scheblykin, I. G., Giant photoluminescence blinking of perovskite nanocrystals reveals single-trap control of luminescence. *Nano Lett* **2015,** *15* (3), 1603-8.

169. Galland, C.; Ghosh, Y.; Steinbruck, A.; Sykora, M.; Hollingsworth, J. A.; Klimov, V. I.; Htoon, H., Two types of luminescence blinking revealed by spectroelectrochemistry of single quantum dots. *Nature* **2011,** *479* (7372), 203-7.

170. Srimath Kandada, A. R.; Petrozza, A., Photophysics of Hybrid Lead Halide Perovskites: The Role of Microstructure. *Acc Chem Res* **2016,** *49* (3), 536-44.

171. Zhao, P.; Xu, J.; Dong, X.; Wang, L.; Ren, W.; Bian, L.; Chang, A., Large-Size CH3NH3PbBr3 Single Crystal: Growth and In Situ Characterization of the Photophysics Properties. *J Phys Chem Lett* **2015,** *6* (13), 2622-8.

172. Fang, H.-H.; Raissa, R.; Abdu-Aguye, M.; Adjokatse, S.; Blake, G. R.; Even, J.; Loi, M. A., Photophysics of Organic-Inorganic Hybrid Lead Iodide Perovskite Single Crystals. *Advanced Functional Materials* **2015,** *25* (16), 2378-2385.

173. Diroll, B. T.; Nedelcu, G.; Kovalenko, M. V.; Schaller, R. D., High-Temperature Photoluminescence of $CsPbX_3$ (X= Cl, Br, I) Nanocrystals. *Advanced Functional Materials* **2017,** *27* (21).

174. Park, Y.-S.; Guo, S.; Makarov, N. S.; Klimov, V. I., Room Temperature Single-Photon Emission From Individual Perovskite Quantum Dots. *ACS Nano* **2015,** *9* (10), 10386-10393.

175. Yuan, G. c.; Ritchie, C.; Ritter, M.; Murphy, S.; Gómez, D. E.; Mulvaney, P., The Degradation and Blinking of Single Perovskite Quantum Dots. *The Journal of Physical Chemistry C* **2018,** *122* (25), 13407–13415.

176. Becker, M. A.; Vaxenburg, R.; Nedelcu, G.; Sercel, P. C.; Shabaev, A.; Mehl, M. J.; Michopoulos, J. G.; Lambrakos, S. G.; Bernstein, N.; Lyons, J. L., Bright triplet excitons in caesium lead halide perovskites. *Nature* **2018,** *553* (7687), 189.

177. Pan, G.; Bai, X.; Yang, D.; Chen, X.; Jing, P.; Qu, S.; Zhang, L.; Zhou, D.; Zhu, J.; Xu, W., Doping Lanthanide into Perovskite Nanocrystals: Highly Improved and Expanded Optical Properties. *Nano Letters* **2017,** *17* (12), 8005-8011.

178. Yuan, X.; Ji, S.; De Siena, M. C.; Fei, L.; Zhao, Z.; Wang, Y.; Li, H.; Zhao, J.; Gamelin, D. R., Photoluminescence Temperature Dependence, Dynamics, and Quantum Efficiencies in Mn^{2+}-Doped $CsPbCl_3$ Perovskite Nanocrystals with Varied Dopant Concentration. *Chemistry of Materials* **2017,** *29* (18), 8003-8011.

179. Beimborn, J. C.; Hall, L. M.; Tongying, P.; Dukovic, G.; Weber, J. M., Pressure Response of Photoluminescence in Cesium Lead Iodide Perovskite Nanocrystals. *The Journal of Physical Chemistry C* **2018,** *122* (20), 11024-11030.

180. Swarnkar, A.; Marshall, A. R.; Sanehira, E. M.; Chernomordik, B. D.; Moore, D. T.; Christians, J. A.; Chakrabarti, T.; Luther, J. M., Quantum Dot–Induced Phase Stabilization of α-CsPbI3 Perovskite for High-Efficiency Photovoltaics. *Science* **2016,** *354* (6308), 92-95.

181. Hai, J.; Li, H.; Zhao, Y.; Chen, F.; Peng, Y.; Wang, B., Designing of Blue, Green, and Red $CsPbX_3$ Perovskite-Codoped Flexible Films with Water Resistant Property and Elimination of Anion-Exchange for Tunable White Light Emission. *Chemical Communications* **2017,** *53* (39), 5400-5403.

182. Demkiv, T.; Myagkota, S.; Malyi, T.; Pushak, A.; Vistovskyy, V.; Yakibchuk, P.; Shapoval, O.; Mitina, N.; Zaichenko, A.; Voloshinovskii, A., Luminescence Properties of $CsPbBr_3$ Nanocrystals Dispersed in a Polymer Matrix. *Journal of Luminescence* **2018,** *198*, 103-107.

183. Pan, A.; Jurow, M. J.; Qiu, F.; Yang, J.; Ren, B.; Urban, J. J.; He, L.; Liu, Y., Nanorod Suprastructures from a Ternary Graphene Oxide–Polymer–$CsPbX_3$ Perovskite Nanocrystal Composite That Display High Environmental Stability. *Nano Letters* **2017,** *17* (11), 6759-6765.

184. Yoon, H. C.; Lee, S.; Song, J. K.; Yang, H.; Do, Y. R., Efficient and Stable $CsPbBr_3$ Quantum-Dot Powders Passivated and Encapsulated with a Mixed Silicon Nitride and Silicon Oxide Inorganic Polymer Matrix. *ACS Applied Materials & Interfaces* **2018,** *10* (14), 11756-11767.

185. Krieg, F.; Ochsenbein, S. T.; Yakunin, S.; Ten Brinck, S.; Aellen, P.; Süess, A.; Clerc, B.; Guggisberg, D.; Nazarenko, O.; Shynkarenko, Y., Colloidal $CsPbX_3$ (X= Cl, Br, I) Nanocrystals 2.0: Zwitterionic Capping Ligands for Improved Durability and Stability. *ACS Energy Letters* **2018,** *3* (3), 641-646.

186. Li, H.; Qian, Y.; Xing, X.; Zhu, J.; Huang, X.; Jing, Q.; Zhang, W.; Zhang, C.; Lu, Z., Enhancing Luminescence and Photostability of $CsPbBr_3$ Nanocrystals via Surface Passivation with Silver Complex. *The Journal of Physical Chemistry C* **2018,** *122* (24), 12994-13000.

187. Liao, M.; Shan, B.; Li, M., In Situ Raman Spectroscopic Studies of Thermal Stability of All-Inorganic Cesium Lead Halide (CsPbX3, X= Cl, Br, I) Perovskite Nanocrystals. *The journal of physical chemistry letters* **2019,** *10*, 1217-1225.

188. Christians, J. A.; Schulz, P.; Tinkham, J. S.; Schloemer, T. H.; Harvey, S. P.; de Villers, B. J. T.; Sellinger, A.; Berry, J. J.; Luther, J. M., Tailored interfaces of unencapsulated perovskite solar cells for> 1,000 hour operational stability. *Nature Energy* **2018,** *3* (1), 68.

189. Bertolotti, F.; Protesescu, L.; Kovalenko, M. V.; Yakunin, S.; Cervellino, A.; Billinge, S. J.; Terban, M. W.; Pedersen, J. S.; Masciocchi, N.; Guagliardi, A., Coherent Nanotwins and Dynamic Disorder in Cesium Lead Halide Perovskite Nanocrystals. *ACS Nano* **2017,** *11* (4), 3819-3831.

190. Cottingham, P.; Brutchey, R. L., On the Crystal Structure of Colloidally Prepared $CsPbBr_3$ Quantum Dots. *Chemical Communications* **2016,** *52* (30), 5246-5249.

191. Bekenstein, Y.; Koscher, B. A.; Eaton, S. W.; Yang, P.; Alivisatos, A. P., Highly Luminescent Colloidal Nanoplates of Perovskite Cesium Lead Halide and Their Oriented Assemblies. *Journal of the American Chemical Society* **2015,** *137* (51), 16008-16011.

192. Santra, K.; Zhan, J.; Song, X.; Smith, E. A.; Vaswani, N.; Petrich, J. W., What Is the Best Method to Fit Time-Resolved Data? A Comparison of the Residual Minimization and the Maximum Likelihood Techniques as Applied to Experimental Time-Correlated, Single-Photon Counting Data. *The Journal of Physical Chemistry B* **2016,** *120* (9), 2484-2490.

193. Yaffe, O.; Guo, Y.; Tan, L. Z.; Egger, D. A.; Hull, T.; Stoumpos, C. C.; Zheng, F.; Heinz, T. F.; Kronik, L.; Kanatzidis, M. G., Local Polar Fluctuations in Lead Halide Perovskite Crystals. *Physical Review Letters* **2017,** *118* (13), 136001.

194. Stoumpos, C. C.; Malliakas, C. D.; Kanatzidis, M. G., Semiconducting Tin and Lead Iodide Perovskites with Organic Cations: Phase Transitions, High Mobilities, and Near-Infrared Photoluminescent Properties. *Inorganic Chemistry* **2013,** *52* (15), 9019-9038.

195. Dastidar, S.; Hawley, C. J.; Dillon, A. D.; Gutierrez-Perez, A. D.; Spanier, J. E.; Fafarman, A. T., Quantitative Phase-Change Thermodynamics and Metastability of Perovskite-Phase Cesium Lead Iodide. *The Journal of Physical Chemistry Letters* **2017,** *8* (6), 1278-1282.

196. De Roo, J.; Ibáñez, M.; Geiregat, P.; Nedelcu, G.; Walravens, W.; Maes, J.; Martins, J. C.; Van Driessche, I.; Kovalenko, M. V.; Hens, Z., Highly Dynamic Ligand Binding and Light Absorption Coefficient of Cesium Lead Bromide Perovskite Nanocrystals. *ACS Nano* **2016,** *10* (2), 2071-2081.

197. Smock, S. R.; Williams, T. J.; Brutchey, R. L., Quantifying the Thermodynamics of Ligand Binding to $CsPbBr_3$ Quantum Dots. *Angewandte Chemie* **2018,** *130* (26), 11885-11889.

198. Hoffman, J. B.; Zaiats, G.; Wappes, I.; Kamat, P. V., $CsPbBr_3$ Solar Cells: Controlled Film Growth through Layer-by-Layer Quantum Dot Deposition. *Chemistry of Materials* **2017,** *29* (22), 9767-9774.

Supplemental Information

Additional Experimental Details

Time-Correlated, Single-Photon Counting Photoluminescence Decay

Time-resolved luminescence data were collected using a home-built, time-correlated, single-photon counting (TCSPC) instrument with a SPC-630 TCSPC module (Becker & Hickl GmbH). A home-built titanium-sapphire laser was frequency doubled at a central wavelength of ~395 nm and the repetition rate was tuned to 2.9 MHz to obtain the excitation source. The excitation beam was vertically polarized. Emission was detected at the "magic angle" (54.7°) with respect to the excitation using a 415-nm, long-pass filter. The instrument response function (IRF) was measured by collecting scattered light at 395 nm (without the emission filter). The full-width at half-maximum (FWHM) of the instrument function was typically ~50 ps. The TCSPC data were collected in 1024 channels (bins), providing a time resolution of 322 ps/channel, and a full-scale time window of 330 ns. The data were analyzed in SPCImage v5.3 software package that uses the nonlinear least square fitting technique.

Single Crystal Fitting Procedure

To study the photophysics of single nanocrystals, the PL movies were analyzed as follows. First, a resultant average image for each movie was generated in ImageJ.

Second, single nanocrystals were highlighted by applying a band-pass intensity threshold followed by an area threshold to the resultant image. The intensity threshold excluded background pixels and bright regions where multiple nanocrystals were located, which are much brighter than single nanocrystals. The area threshold excluded areas where aggregates have formed but may not entirely overlap. The intensity thresholds were ~1300-3700 and ~900-2200 counts for $CsPbBr_3$ and $CsPbI_3$, while the area threshold was set at less than 20 square pixels for both compositions. The Analyze Particles function in ImageJ was used to identify single nanocrystals suitable for analysis. Third, for each single crystal identified, a Z-axis projection of the brightest pixel was plotted along with a local background pixel selected 4 pixels away. To establish frames where the nanocrystal was ON (in a luminescent state) or OFF (in a dark state), the limit of luminescence detection for each single crystal was calculated as the average luminescence intensity plus three times the standard deviation for the background pixel for all 2000 frames. In this way, each crystal analyzed has a unique background pixel and limit of detection. Thus, a single crystal is ON for a frame if the measured intensity was above the limit of detection for that frame. To categorize the luminescence type of the nanocrystals, the luminescence intensity vs. time and histogram of luminescence intensities of each crystal were plotted, and linear regressions were calculated for luminescence intensity vs. time data. Nanocrystals that show 2 distinct distributions of intensities were classified as *Bimodal*. Nanocrystals that show non-significant slopes ($m < 3\sigma_{bkgd}$, 3 times the standard deviation of the background for the total analysis time) were classified as *Constant*. Nanocrystals that show a change in intensity at a significant rate ($|m| > 3\sigma_{bkgd}$) were classified as *Photobleaching* (decreasing intensity) or

Photobrightening (increasing intensity). Nanocrystals that showed extremely intermittent intensity and were in the ON state less than 20% of the time were classified as *Other*.

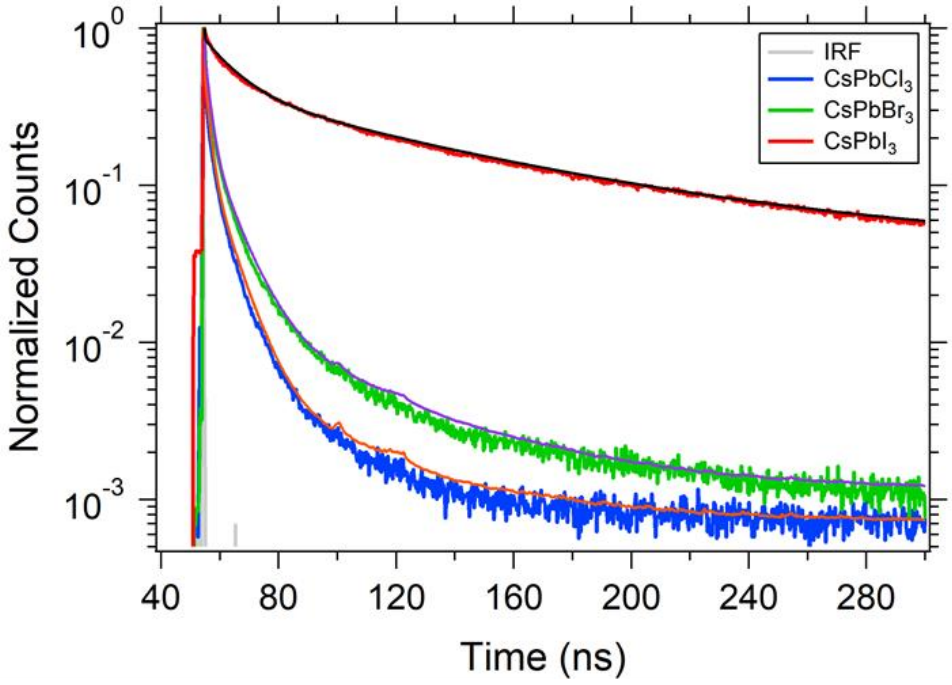

Sample	τ_1 (ns)	τ_2 (ns)	τ_3 (ns)	$\langle\tau\rangle$ (ns)
$CsPbCl_3$	0.3	3.8	18.6	1.2
%	80.6	18.1	1.3	
$CsPbBr_3$	0.7	5.0	26.1	2.3
%	73.2	24.5	2.3	
$CsPbI_3$	8.8	56.2	138.7	41.5
%	54.5	32.0	13.5	

Figure S1. (Top) Time-correlated, single-photon counting photoluminescence data and (bottom) three-exponential fit parameters for $CsPbX_3$ nanocrystals suspended in toluene.

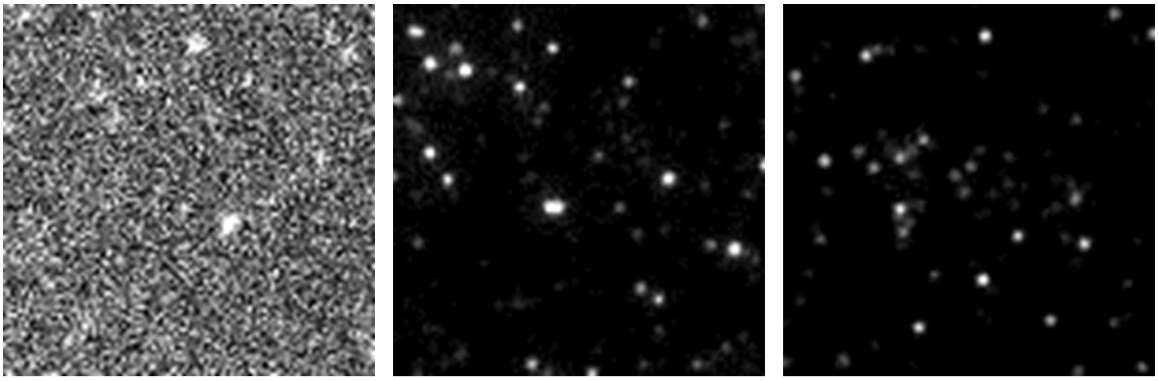

Figure S2. Representative single frame images from single crystal luminescence movies.

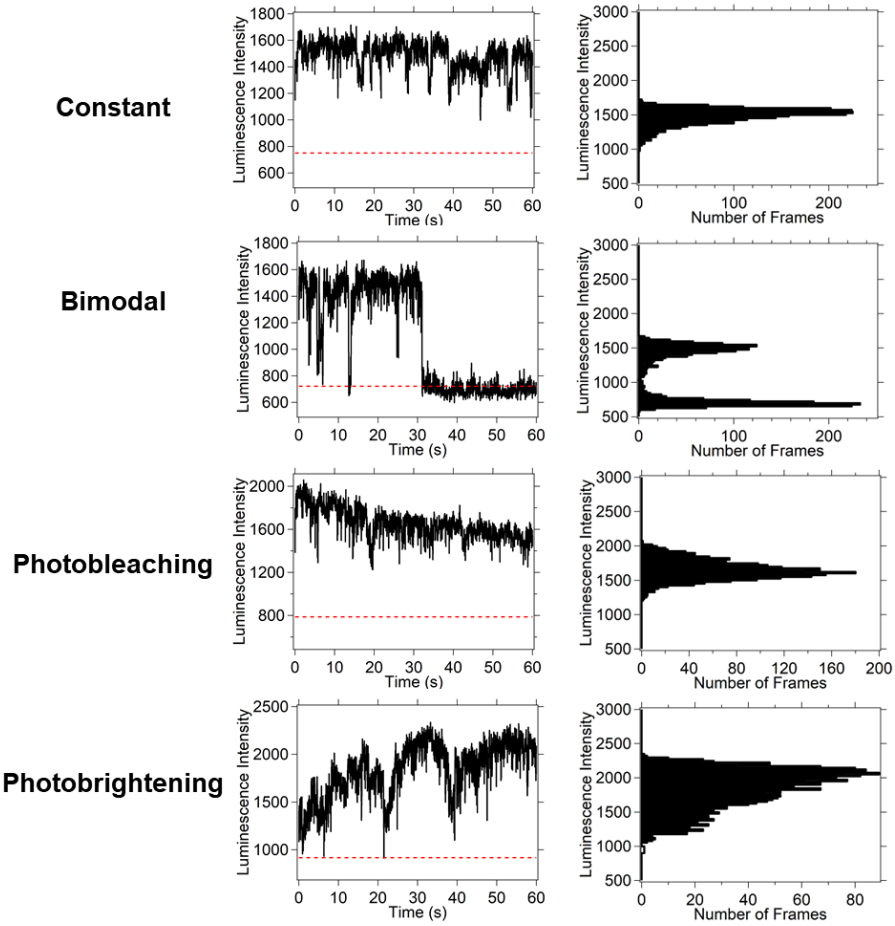

Figure S3. Representative intensity vs. time data for luminescence types of $CsPbX_3$ nanocrystals and count statistics for luminescence types.

Table S1. Count statistics of photoluminescence types for $CsPbBr_3$, $CsPbI_3$, and $CsPbI_3$-MeOAc nanocrystals. Details of the classifications are found above in the text describing the single crystal fitting procedure.

	Constant	Photobleaching	Photobrightening	Bimodal	Other	Total	On%[a]
$CsPbBr_3$	138	62	31	29	7	267	87%
$CsPbI_3$	62	73	66	28	4	233	97%
$CsPbI_3$-MeOAc	50	184	7	9	0	250	99%

[a] = *On% denotes the percentage of ON frames from all nanocrystals over the total analysis time.*

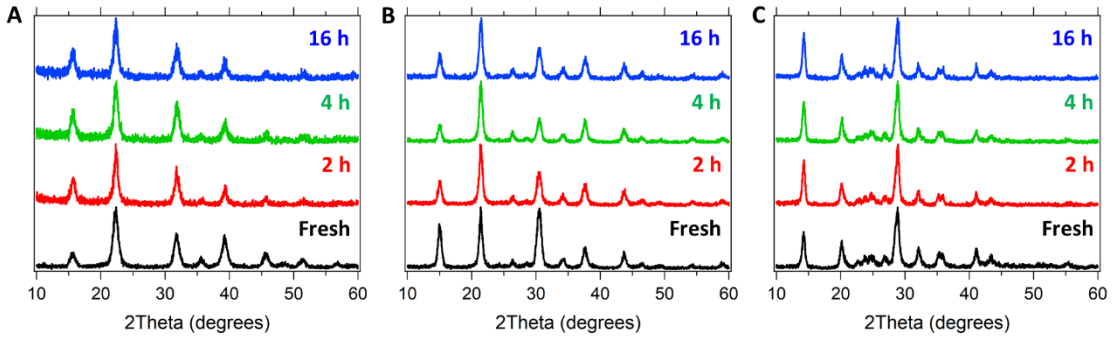

Figure S4. XRD control experiment of A) $CsPbCl_3$, B) $CsPbBr_3$, and C) $CsPbI_3$ nanocrystals kept in dark, ambient conditions.

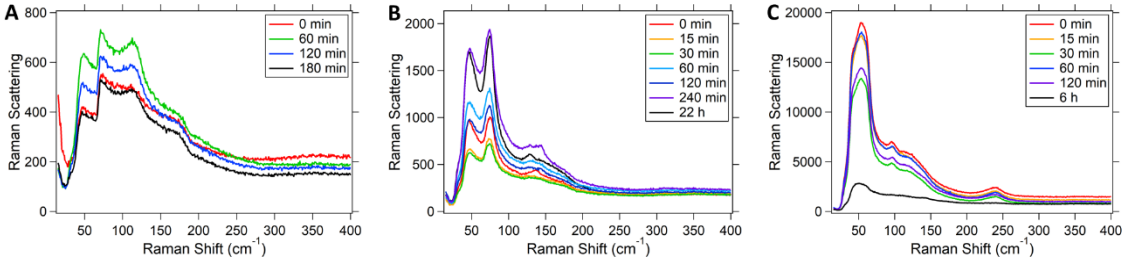

Figure S5. Raman spectra for A) $CsPbCl_3$, B) $CsPbBr_3$, and C) $CsPbI_3$ nanocrystals as a function of illumination time with solar simulator.

Table S2. Fit statistics for power law and multi-exponential fits of ON/OFF data for $CsPbX_3$ nanocrystals. A three-exponential fit was used because of the wide distribution of long-lived states, and because the correlation (based on R^2) was much higher than a biexponential fit, except for the fresh and 2 h OFF series for $CsPbI_3$-MeOAc nanocrystals. The calculated average τ is the weighted average of the multi-exponential terms. Error was estimated by performing 1000 Monte Carlo simulations. In the case of the $CsPbI_3$-MeOAc Fresh and 2 h OFF series, the data was fit to a bi-exponential since there were so few time bins in these series.

$CsPbBr_3$		**ON Events**			**OFF Events**		
Fit	**Parameter**	**Fresh**	**2 h**	**4 h**	**Fresh**	**2 h**	**4 h**
Power Law	α	1.450 ± 0.001	1.827 ± 0.006	2.79 ± 0.03	2.014 ± 0.001	1.876 ± 0.006	1.320 ± 0.008
Multi-Exponential	a_1	0.977 ± 0.003	0.954 ± 0.002	0.982 ± 0.009	0.953 ± 0.004	0.941 ± 0.003	0.85 ± 0.06
	τ_1	0.037 ± 0.003	0.0319 ± 0.0005	0.0145 ± 0.0008	0.0240 ± 0.0006	0.0320 ± 0.0005	0.069 ± 0.005
	a_2	0.022 ± 0.003	0.046 ± 0.002	0.017 ± 0.008	0.047 ± 0.004	0.059 ± 0.003	0.14 ± 0.01
	τ_2	0.6 ± 0.2	0.185 ± 0.004	0.053 ± 0.009	0.110 ± 0.005	0.153 ± 0.004	0.35 ± 0.03
	a_3	0.0007 ± 0.0003	0.00024 ± 0.00003	0.0004 ± 0.0002	0.0005 ± 0.0001	0.00008 ± 0.00001	0.0071 ± 0.0007
	τ_3	5.7 ± 0.9	2.0 ± 0.1	0.31 ± 0.07	0.98 ± 0.07	2.7 ± 0.3	2.8 ± 0.2
Calculated Average	τ	0.0533	0.0393	0.0153	0.0285	0.0392	0.128

$CsPbI_3$		ON Events			OFF Events		
Fit	**Parameter**	**Fresh**	**2 h**	**4 h**	**Fresh**	**2 h**	**4 h**
Power Law	α	1.28 ± 0.01	1.50 ± 0.01	1.38 ± 0.01	1.91 ± 0.02	2.05 ± 0.02	2.06 ± 0.02
Multi-Exponential	a_1	0.970 ± 0.008	0.967 ± 0.002	0.948 ± 0.009	0.958 ± 0.009	0.92 ± 0.02	0.94 ± 0.01
	τ_1	0.039 ± 0.007	0.050 ± 0.002	0.063 ± 0.003	0.027 ± 0.002	0.019 ± 0.002	0.017 ± 0.002
	a_2	0.029 ± 0.008	0.033 ± 0.002	0.051 ± 0.004	0.042 ± 0.009	0.08 ± 0.02	0.06 ± 0.01
	τ_2	0.39 ± 0.04	0.58 ± 0.02	0.68 ± 0.05	0.13 ± 0.01	0.075 ± 0.009	0.078 ± 0.007
	a_3	0.0009 ± 0.0002	0.00024 ± 0.00003	0.00052 ± 0.00005	0.0004 ± 0.0001	0.0018 ± 0.0007	0.0006 ± 0.0002
	τ_3	13.5 ± 0.8	9.9 ± 0.9	10.5 ± 0.9	1.9 ± 0.3	0.37 ± 0.06	0.6 ± 0.1
Calculated Average	τ	0.0613	0.0700	0.0998	0.0321	0.0242	0.0215

$CsPbI_3$-MeOAc		ON Events			OFF Events		
Fit	**Parameter**	**Fresh**	**2 h**	**4 h**	**Fresh**	**2 h**	**4 h**
Power Law	α	0.88 ± 0.03	0.90 ± 0.03	1.42 ± 0.03	2.6 ± 0.1	2.7 ± 0.2	1.83 ± 0.04
Multi-Exponential	a_1	0.91 ± 0.05	0.90 ± 0.04	0.982 ± 0.007	0.94 ± 0.02	0.97 ± 0.02	0.97 ± 0.01
	τ_1	0.10 ± 0.01	0.11 ± 0.01	0.033 ± 0.003	0.014 ± 0.004	0.012 ± 0.004	0.037 ± 0.003
	a_2	0.08 ± 0.01	0.09 ± 0.01	0.017 ± 0.002	0.06 ± 0.02	0.03 ± 0.02	0.028 ± 0.003
	τ_2	0.78 ± 0.09	1.8 ± 0.2	0.46 ± 0.05	0.048 ± 0.009	0.05 ± 0.01	0.24 ± 0.02
	a_3	0.0084 ± 0.0009	0.008 ± 0.001	0.00041 ± 0.00004	-	-	7.1E-6 ± 0.8E-6
	τ_3	25 ± 3	24 ± 3	12 ± 1	-	-	25 ± 3
Calculated Average	τ	0.363	0.453	0.045	0.011	0.013	0.043

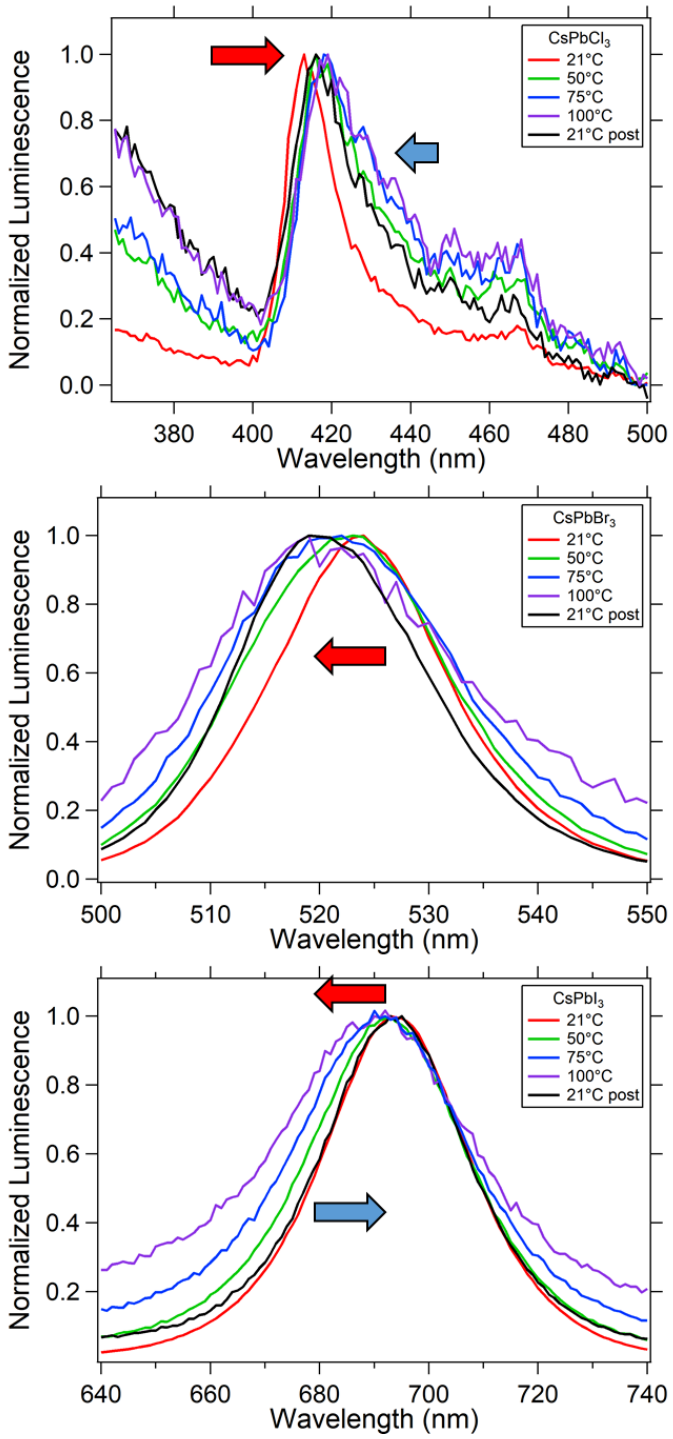

Figure S6. Normalized solution photoluminescence spectra of $CsPbX_3$ nanocrystals at increasing temperatures, followed by cooling back to room temperature.

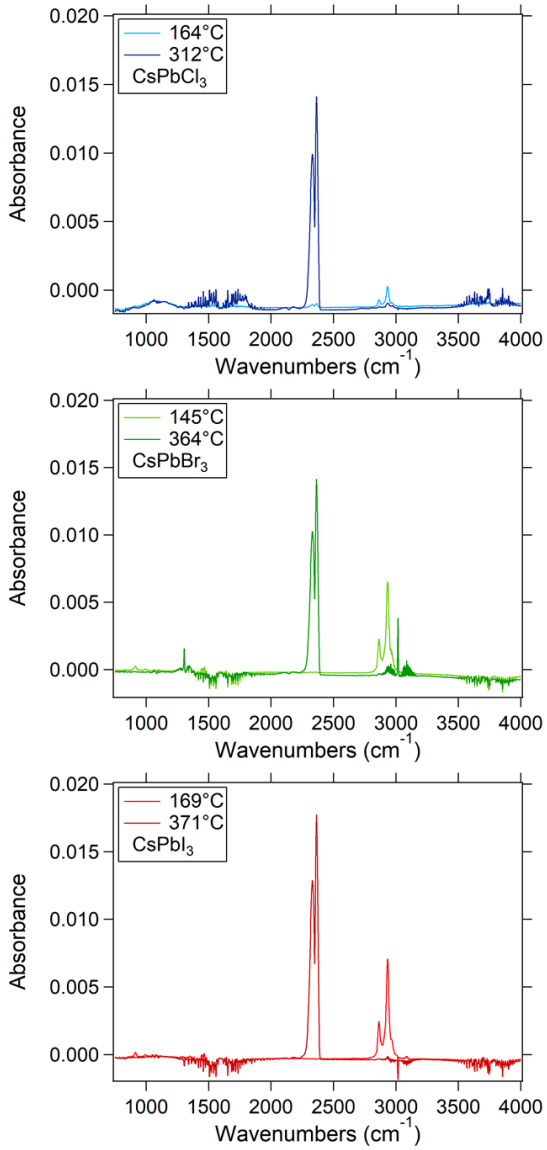

Figure S7. Representative FTIR spectra from TGA-FTIR analysis of $CsPbX_3$ nanocrystals at selected temperatures, showing loss products. The bands from 1300-1700 cm^{-1} and 3600-3900 are from slight water and methane impurities in the instrumental setup. In each plot, the lower temperature spectrum shows bands from oleylamine/oleic acid surface ligands, and the higher temperature spectrum shows CO_2 bands as a result of surface ligand decomposition.

CHAPTER 4. SUBDIFFRACTION MICROSCOPY BY SATURATED LUMINESCENCE OF INORGANIC QUANTUM DOTS

Brett W. Boote, Kalyan Santra, Avinash Singh, Jacob W. Petrich, Emily A. Smith*

Affiliations

Department of Chemistry, Iowa State University, and The Ames Laboratory, U.S. Department of Energy, Ames, Iowa 50011-3111, United States

Abstract

Recent advances in microscopy have enabled subdiffraction imaging, or going beyond the Abbe diffraction limit of light, to investigate fine structures previously only resolvable in electron microscopy. In this work, the concept of saturated excitation microscopy is extended to the photoluminescence of inorganic semiconductor nanocrystals. Demodulation of the luminescence signal at harmonics of the fundamental frequency (2*f*, 3*f*, etc). For QD655 (CdSe/ZnS core/shell) quantum dots, the resolution improvement was found to be 23% when demodulating the signal at the third harmonic. Though the resolution achieved here is not as high as with other subdiffraction techniques such as STED or STORM, saturated luminescence offers a simple approach to resolution improvement. This work could prove beneficial to the characterization of new materials such as quantum dots, thin films, or even functional devices.

Introduction

Subdiffraction microscopy techniques allow for the study of sample features smaller than the Abbe diffraction limit. Generally, one of two strategies are employed for subdiffraction imaging: a spatial or temporal modulation of the excitation light to reduce the point spread function, or the aggregation into a resultant image of numerous two-dimensional localizations of photoswitchable fluorophores.[30] Many of these techniques can push the microscopy resolution well below 100 nm, giving rise to previously unresolvable cellular structural details. In many cases, the extent of resolution improvement correlates to the degree of experimental complexity, either in terms of optical components and alignment, or careful selection of caged/photoswitching fluorophores and imaging conditions followed by extensive post-processing of large data files. Often there is also an exchange for spatial and temporal resolution, both of which can be important based on the sample of interest. Some examples of excitation modulation-based subdiffraction techniques include stimulated emission-depletion (STED) microscopy,[26, 199] structured illumination microscopy (SIM),[25, 43] saturated structured illumination microscopy (SSIM),[44, 200] plasmonic structured illumination microscopy (PSIM),[32, 201] and saturated excitation (SAX)[39, 42, 202] microscopy. Common examples of localization-based subdiffraction techniques are photo-activated localization microscopy (PALM)[23, 203] and stochastic optical reconstruction microscopy (STORM).[29, 204]

Saturated excitation microscopy, pioneered by Katsumasa Fujita, is a simple approach to subdiffraction imaging through temporal modulation of the excitation light.[42] By demodulation at harmonics (*nf*) of the fundamental modulation frequency (*f*), non-linear information can be obtained. The Gaussian intensity profile of the laser spot leads

to the effect that only the high-intensity area (center of the spot) generates saturation, and thus higher order demodulation leads to resolution improvement. The resolution improvement is theoretically unlimited, though finite laser power, sample integrity, and detector efficiency all limit the observable resolution gains. This technique has been demonstrated for several different mechanisms, including fluorescence in biological samples,[33, 39-40, 202] scattering of gold nanoparticles,[205] and coherent anti-Stokes Raman spectroscopy.[206] In general, a qualitative resolution improvement is shown in images collected at higher harmonics (larger n) since the harmonic content comes from a smaller region than the diffraction-limited laser spot.

In this work, we sought to extend the concept of using saturated excitation microscopy to measure luminescence of inorganic semiconductor nanocrystals. To the best of our knowledge, luminescence has not been studied previously as a saturated excitation mechanism. Quantum dots have previously been shown to produce subdiffraction images through second- and third-order photon antibunching, though this is a different mechanism than the modulation method proposed here.[31] The robust material characteristics combined with bright photoluminescence make inorganic quantum dots favorable candidates for resolution improvement through saturated excitation. In addition, information about the photophysics of quantum dot samples may be extracted by similar methods.

Experimental Section

Materials

Ethanol (95%) and Life Technologies QD655 quantum dots were purchased from ThermoFisher. Rhodamine 6G was purchased from Allied Chemical and Dye

Corporation. Poly-L-lysine (0.1% aqueous), *p*-phenylenediamine, and glycerol (99%) were purchased from Sigma-Aldrich and used without further purification.

Saturated Luminescence Instrumentation

The saturated luminescence platform was home built on an air-stabilized optical table (Newport Corporation, Irvine, CA). To modulate the excitation source, a modified Mach-Zehnder interferometer was used. A 250-mW 532-nm GEM (Laser Quantum, Fremont, CA) diode laser was separated into two arms using a 50:50 beam splitter cube, and two acousto-optic modulators (AOMs, IntraAction Corp, Bellwood, IL) operating at 40.00 MHz and 40.01 MHz were used to doppler shift the laser emission by their respective radio frequencies. The first diffracted line of each AOM was selected by an aperture and recombined at a second 50:50 beam splitter cube, which produces a sinusoidal modulation at the difference frequency of the two AOMs (in this case, 10 kHz). One output line from the interferometer was sent through an OD2 neutral density filter to a photodiode (SM1A, Thor Labs, Newton, NJ), which was amplified by a PDA200 amplifier (Thor Labs) and coupled to the reference input of an SR830 lock-in amplifier (Stanford Research Systems, Sunnyvale, CA). A BE03M beam expander (Thor Labs) expanded output from the second output line into the back port of a Ti-U inverted microscope (Nikon Instruments, Melville, NY)equipped with a Plan Apo DC 100× Oil (1.40 NA) objective using a 532 nm BrightLine super-resolution dichroic mirror (IDEX Health & Science, Rochester, NY). Emission from the sample was passed through a 650 ± 100 nm fluorescence filter, a 200 μm pinhole at the back focal plane of the microscope, and an additional 542-nm long-pass filter before detection by an R928P photomultiplier tube (Hamamatsu Photonics, Bridgewater Township, NJ), which was terminated with a 50 Ω load resistor into the lock-in amplifier. A PCI-6032E data acquisition card (National

Instruments, Austin, TX) digitized the data stream from the lock-in amplifier. A 562.3CD PIMars XYZ piezo stage (Physik Instrumente, Auburn, MA) provided precision sample movement to generate images. Custom LabVIEW code controlled stage movement and data acquisition from the lock-in amplifier. The modulation depth was observed and optimized using a 9350AM oscilloscope (Teledyne LeCroy, Chestnut Ridge, NY). In all experiments, the modulation depth was greater than 97%. Data was plotted using MATLAB (Mathworks, Natick, MA) and cross sections were measured using ImageJ. Gaussian fitting was carried out using IGOR 6.36 (Wavemetrics, Portland, OR).

Sample Preparation

A custom-built sample holder was constructed to hold glass coverslips in the aperture of the piezo stage. For rhodamine 6G measurements, wells were constructed from adhesive-backed rubber tape fixed to glass coverslips, and 50 μL of a 10 μM solution was added to the well. For laser spot size determination, citrate-stabilized ~50-nm gold nanoparticles were dropcast on poly-lysine treated glass slides. For luminescence measurements, QD655 quantum dots (Life Technologies) were diluted to ~3 nM and drop cast onto poly-lysine coated glass coverslips. Subsequently 10 μL of an anti-fading solution (consisting of 0.02% p-phenylenediamine in a 10:90 v/v solution of tris buffer, pH = 8.5, and glycerol) and a second coverslip were placed. The samples were then clamped in the sample holder for imaging. Using a combination of ND filters and laser settings, the range of laser powers used was 1.7×10^4 to 5.0×10^6 W/cm^2.

Results and Discussion

Subdiffraction information via saturated luminescence microscopy can be used to study fine structure and surface quality/defects in nanocrystal films, which may be used

to tune these properties. To assess the feasibility of saturated luminescence of inorganic quantum dots for subdiffraction imaging, a home-built instrument was constructed as shown in **Figure 1**. Briefly, a 532-nm laser is sinusoidally modulated at 10 kHz via two

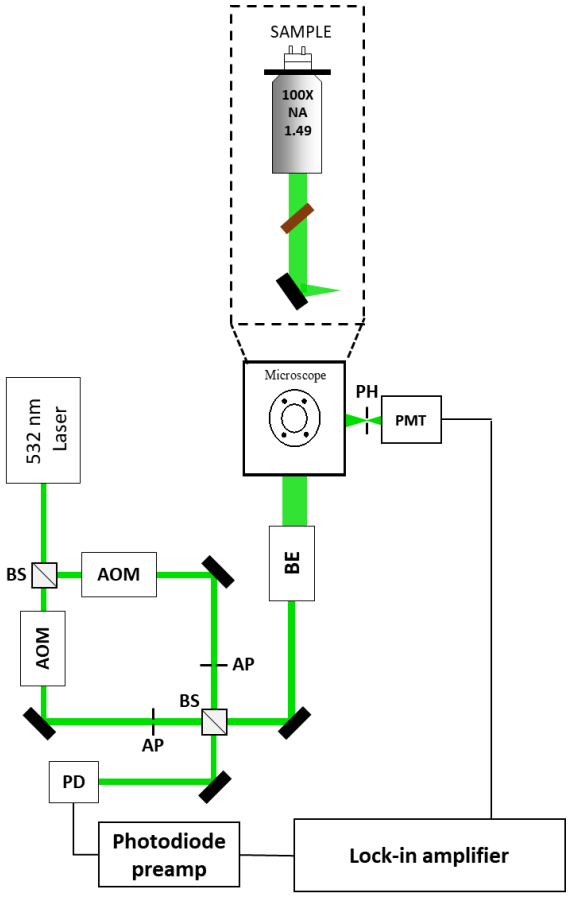

Figure 1. Instrumental schematic for saturated luminescence microscopy. A 532-nm laser is modulated via two AOMs in a Mach-Zehnder configuration and demodulation is carried out by the lock-in amplifier. A photodiode passes the reference signal to the lock-in. Abbreviations: **BS** 50:50 beam splitter cube, **AOM** acousto-optic modulator, **AP** aperture, **PD** photodiode, **BE** beam expander, **PH** pinhole, **PMT** photomultiplier tube.

acousto-optic modulators (set to 40.00 and 40.01 MHz) operating in a Mach-Zehnder configuration. Half the output is detected by a photodiode that passes signal to the reference channel of the lock in amplifier, while the other half is sent to the microscope. The signal is collected through two long pass filters to efficiently block the laser line and passed through a pinhole and detected by a photomultiplier tube, which passes the signal

to the input channel of the lock-in amplifier. An XYZ piezo stage with ±2 nm precision scans the sample over the objective to generate an image.

In order to test the system and demonstrate harmonic detection, fluorescence from a 10 μM solution of rhodamine 6G was measured at several laser irradiances and the results are shown in **Figure 2**. Demodulating at the fundamental (10 kHz) results in a linear signal up to a laser irradiance of ~10^5 W/cm^2 followed by a diminishing increase in signal with no appreciable increase above ~10^6 W/cm^2. This is a result of saturating the excited state and later photobleaching of the available rhodamine 6G molecules in the focal volume. Similar trends were observed for demodulation at 2*f* and 3*f*, although the onsets of measurable signal and the slopes of the linear regions are different for these harmonics. Based on theory, the expected power dependence of the signal demodulated at *f*, 2*f*, and 3*f* in the log-log plot would be 1, 2, and 3, respectively. Fitting the linear regions of these data, our results show exponents of 0.85, 1.33, and 2.00. The discrepancy in these values is likely a result of photobleaching within the sample combined with

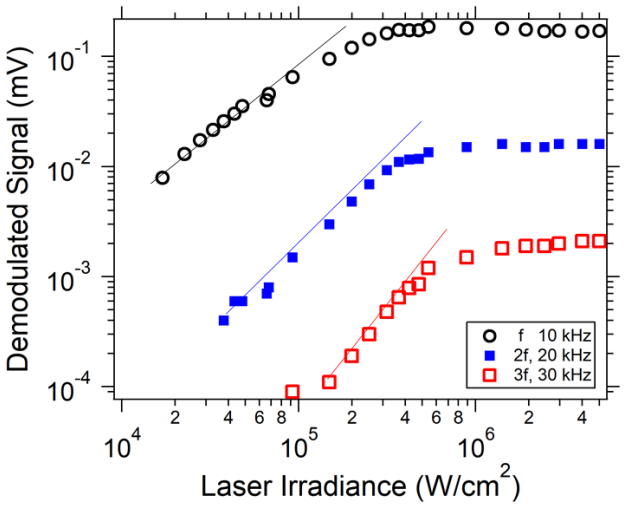

Figure 2. Measured signal for rhodamine 6G demodulated at the frequencies shown. As saturation of the excited state occurs, signals at higher harmonics are observed. The measured power dependence of the linear regions were 0.85, 1.33, and 2.00 for 10, 20, and 30 kHz, respectively. Lines have been drawn on the linear regions of the data series for easier comparison.

saturation of the fluorophore, and compares qualitatively to previous literature reports of saturated detection of rhodamine 6G.[42] This experiment demonstrated the ability to collect signal at harmonics with this setup.

The laser spot size must be known, as it plays a significant role in the spatial resolution and the calculation of laser irradiance. The modulated Rayleigh scattering of 50 nm gold nanoparticles was used to generate an image (demodulated at *f*) and subsequently measure the laser spot size. A representative image is shown in **Figure 3**. The laser spot size is determined as the full width at half-maximum (FWHM) in horizontal and vertical cross sections. The laser spot was determined to be 260 ± 10 nm, which for our system is very nearly the Abbe diffraction limit. Using 532 nm excitation, a typical M^2 value of 1.1, and an objective of 1.40 NA the calculated diffraction limited spot is 253 nm. This shows the system alignment and laser input to the objective are both highly optimized.

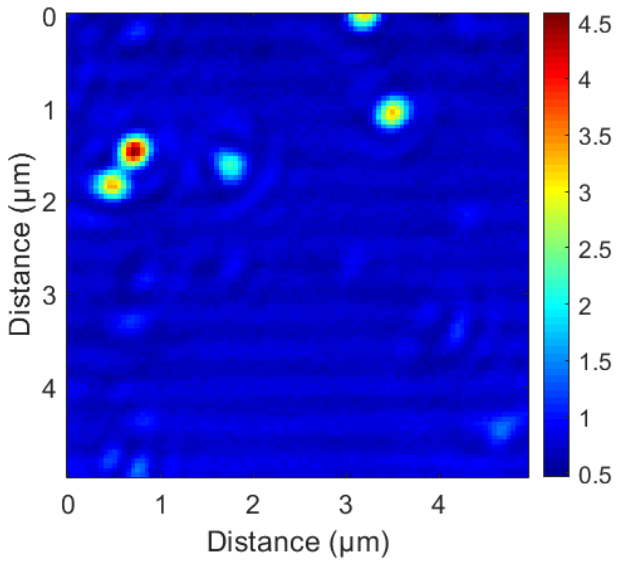

Figure 3. Representative image showing Rayleigh scattering from individual 50-nm gold nanoparticles. The color bar shows voltage of the demodulated signal at *f* from the lock-in amplifier. The step size was 50 nm and the laser irradiance was 2.8×10^4 W/cm^2.

QD655 quantum dots were sparsely coated onto a cover slip and used to demonstrate saturated luminescence. Images of two areas of the sample demodulated at *f* (10 kHz) and 3*f* (30 kHz) with are shown in **Figure 4**. The laser irradiances were 2.7×10^5 W/cm^2 and 2.7×10^6 W/cm^2 for the *f* and 3*f* images, respectively. The 2*f* image was not collected since the highest order harmonic with adequate signal-to-noise ratio (SNR) will provide the best resolution. Comparing the *f* and 3*f* images, areas of overlapping background signal (which generally reduce contrast in images) are decreased significantly. This is likely due to the inability of background signals to be saturated.

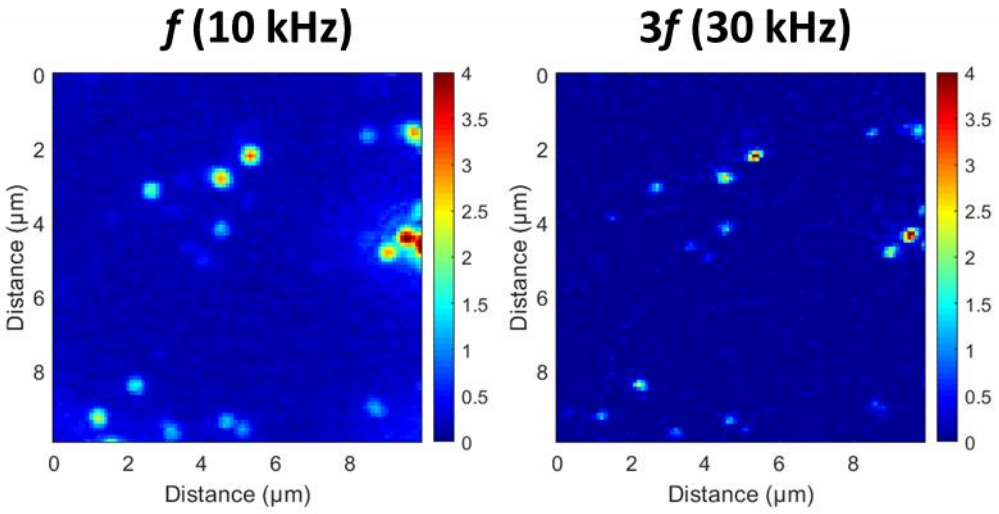

Figure 4. Representative saturated luminescence images demodulated at the fundamental (10 kHz) and the third harmonic (30 kHz). The fundamental images were collected using 2.7×10^5 W/cm^2 while the 3*f* images were collected with 2.7×10^6 W/cm^2. To assess resolution improvement, X and Y cross sections of 12 quantum dots were fit to Gaussian curves. The step size was 100 nm.

To quantitatively assess the resolution improvement of the 3*f* image compared to the fundamental, nanocrystals were fitted to Gaussian curves. The average apparent size of the quantum dots in the fundamental image was 420 ± 40 nm, while the average apparent size of quantum dots in the 3*f* image was 270 ± 30 nm. This represents a 36%

increase in resolution for the same subset of quantum dots. The apparent sizes of the quantum dots in the fundamental image are larger than the apparent sizes of the gold nanoparticles as measured by scattering. The main difference here is the apparent size of the quantum dots is the product of the excitation point spread function and the luminescence point spread function, while scattering only depends on the excitation point spread function.[207] Another possible reason for the observed size difference is the potential inclusion of a few aggregates in the quantum dot sizes measured (note the standard deviation of measured sizes).

Interestingly, the extent of resolution improvement differs from quantum dot to quantum dot. This is likely a consequence of the quantum yield and luminescence lifetime differences among individual quantum dots. A distribution of discrete lifetimes leads to different degrees of saturation of the excited state among individual quantum dots for a given laser irradiance, and thus more (or less) effective resolution improvement. Brighter quantum dots lead to higher SNR, which makes these quantum dots easier to distinguish from background and noise in the images collected at 3*f*. A previous literature report investigating saturated scattering of gold nanoparticles as a mechanism for subdiffraction imaging shows a broad distribution of sizes among ~10 nanoparticles, most notably by demodulating at 3*f*.[205] The authors comment that aggregated particles undergo a shift in their surface plasmon resonance (SPR) band and thus are not saturating the transition to the extent of single nanoparticles, though even among non-aggregated nanoparticles an apparent size difference of approximately 50% is observed within the 3*f* image.

Conclusions

In this work the practicality and feasibility of a subdiffraction imaging technique based on saturated luminescence was investigated. Quantitative Gaussian fits of single quantum dots indicate a 36% resolution improvement for images demodulated at 3*f* when compared to the confocal fundamental image. Interestingly, the extent of resolution improvement varied from quantum dot to quantum dot, which is likely a consequence of the quantum yield and luminescence lifetime varying among single quantum dots, which changes the SNR and degree of saturation (and hence the achievable resolution).

Compared to STED systems the resolution achieved with saturated luminescence in this work is larger, though the cost and complexity of the setup are both lower. In addition, a wider range of luminescence markers can be used since a single excitation wavelength is all that is required, and multiple wavelength capability (e.g. a 405-nm laser and a 532-nm laser) could be readily adapted to cover a larger region of the visible spectrum. Other localization-based subdiffraction techniques such as STORM have also demonstrated higher resolution but require photoswitchable fluorophores and costly CCD or scientific CMOS cameras. Saturated luminescence offers a simple approach to subdiffraction microscopy using inorganic quantum dots.

Future work on this technique involves demonstrating resolution improvement in an imaging application (e.g. biological samples, thin polymer films) where the luminescence will compete with increased background, as well as investigation into the correlation between resolution improvement and luminescence lifetime on a single quantum dot basis. The latter could be undertaken by adapting the system to pulsed laser excitation and single photon counting electronics in order to collect saturated images and lifetime images of the same quantum dots.

Acknowledgements

This research is supported by the U.S. Department of Energy, Office of Science, Office of Biological and Environmental Research (BER) through the Ames Laboratory. The Ames Laboratory is operated for the U.S. Department of Energy by Iowa State University under Contract No. DE-AC02-07CH11358.

References

23. Betzig, E.; Patterson, G. H.; Sougrat, R.; Lindwasser, O. W.; Olenych, S.; Bonifacino, J. S.; Davidson, M. W.; Lippincott-Schwartz, J.; Hess, H. F., Imaging intracellular fluorescent proteins at nanometer resolution. *Science* **2006,** *313* (5793), 1642-1645.

25. Gustafsson, M. G. L.; Shao, L.; Carlton, P. M.; Wang, C. J. R.; Golubovskaya, I. N.; Cande, W. Z.; Agard, D. A.; Sedat, J. W., Three-dimensional resolution doubling in wide-field fluorescence microscopy by structured illumination. *Biophysical journal* **2008,** *94*, 4957-4970.

26. Hell, S. W.; Wichmann, J., Breaking the diffraction resolution limit by stimulated emission: stimulated emission-depletion fluorescence microscopy. *Optics Letters* **1994,** *19* (11), 780-782.

29. Rust, M. J.; Bates, M.; Zhuang, X., Sub-diffraction-limit imaging by stochastic optical reconstruction microscopy (STORM). *Nature methods* **2006,** *3* (10), 793.

30. Schermelleh, L.; Ferrand, A.; Huser, T.; Eggeling, C.; Sauer, M.; Biehlmaier, O.; Drummen, G. P., Super-resolution microscopy demystified. *Nature cell biology* **2019,** *21* (1), 72.

31. Schwartz, O.; Levitt, J. M.; Tenne, R.; Itzhakov, S.; Deutsch, Z.; Oron, D., Superresolution microscopy with quantum emitters. *Nano letters* **2013,** *13* (12), 5832-5836.

32. Wei, F.; Lu, D.; Shen, H.; Wan, W.; Ponsetto, J. L.; Huang, E.; Liu, Z., Wide field super-resolution surface imaging through plasmonic structured illumination microscopy. *Nano letters* **2014,** *14* (8), 4634-4639.

33. Yamanaka, M.; Yonemaru, Y.; Kawano, S.; Uegaki, K.; Smith, N. I.; Kawata, S.; Fujita, K., Saturated excitation microscopy for sub-diffraction-limited imaging of cell clusters. *Journal of biomedical optics* **2013,** *18* (12), 126002-126002.

39. Yonemaru, Y.; Yamanaka, M.; Smith, N. I.; Kawata, S.; Fujita, K., Saturated excitation microscopy with optimized excitation modulation. *ChemPhysChem* **2014,** *15* (4), 743-749.

40. Yamanaka, M.; Saito, K.; Smith, N. I.; Kawata, S.; Nagai, T.; Fujita, K., Saturated excitation of fuorescent proteins for subdiffraction-limited imaging of living cells in three dimensions. *Interface Focus* **2013,** *3*, 1-7.

42. Fujita, K.; Kobayashi, M.; Kawano, S.; Yamanaka, M.; Kawata, S., High-resolution confocal microscopy by saturated excitation of fluorescence. *Physical Review Letters* **2007,** *99*, 228105.

43. Gustafsson, M. G. L., Nonlinear structured-illumination microscopy: wide-field fluorescence imaging with theoretically unlimited resolution. *Proceedings of the National Academy of Sciences* **2005,** *102* (37), 13081-13086.

44. Heintzmann, R.; Jovin, T. M., Saturated patterned excitation microscopy—a concept for optical resolution improvement. *Journal of the Optical Society of America A* **2002,** *19* (8), 1599-1609.

199. Heine, J.; Reuss, M.; Harke, B.; D'Este, E.; Sahl, S. J.; Hell, S. W., Adaptive-illumination STED nanoscopy. *Proceedings of the National Academy of Sciences* **2017,** *114* (37), 9797-9802.

200. Haeberlé, O.; Simon, B., Saturated structured confocal microscopy with theoretically unlimited resolution. *Optics Communications* **2009,** *282*, 3657-3664.

201. Wei, F.; Liu, Z., Plasmonic structured illumination microscopy. *Nano letters* **2010,** *10* (7), 2531-2536.

202. Yamanaka, M.; Kawano, S.; Fujita, K.; Smith, N. I.; Kawata, S., Beyond the diffraction-limit biological imaging by saturated excitation microscopy. *Journal of biomedical optics* **2008,** *13* (5), 050507-050507-3.

203. Manley, S.; Gillette, J. M.; Patterson, G. H.; Shroff, H.; Hess, H. F.; Betzig, E.; Lippincott-Schwartz, J., High-density mapping of single-molecule trajectories with photoactivated localization microscopy. *Nature methods* **2008,** *5* (2), 155.

204. Huang, B.; Wang, W.; Bates, M.; Zhuang, X., Three-dimensional super-resolution imaging by stochastic optical reconstruction microscopy. *Science* **2008,** *319* (5864), 810-813.

205. Chu, S.-W.; Su, T.-Y.; Oketani, R.; Huang, Y.-T.; Wu, H.-Y.; Yonemaru, Y.; Yamanaka, M.; Lee, H.; Zhuo, G.-Y.; Lee, M.-Y., Measurement of a saturated emission of optical radiation from gold nanoparticles: application to an ultrahigh resolution microscope. *Physical review letters* **2014,** *112* (1), 017402.

206. Yonemaru, Y.; Palonpon, A. F.; Kawano, S.; Smith, N. I.; Kawata, S.; Fujita, K., Super-Spatial-and-Spectral-Resolution in Vibrational Imaging via Saturated Coherent Anti-Stokes Raman Scattering. *Physical Review Applied* **2015,** *4* (1), 014010.

207. Zhang, B.; Zerubia, J.; Olivo-Marin, J.-C., Gaussian approximations of fluorescence microscope point-spread function models. *Appl. Opt.* **2007,** *46* (10), 1819-1829.

CHAPTER 5. GENERAL CONCLUSION

In conclusion, two leading nanocrystal compositions for energy applications were prepared and fully characterized. Germanium-tin alloy nanocrystals did not show evidence of more direct band gap character, but tin incorporation combined with a cadmium sulfide shell exhibited up to 15× improvement in photoluminescence intensity. This observation is likely due to improved epitaxy (smaller lattice mismatch) between the core and shell materials. Additionally, samples with the same composition which showed evidence of oxidation in the alloy core resulted in a 100-fold decrease in luminescence intensity. These observations will aid in the intelligent design of increasingly efficient germanium-based materials in applications such as energy storage and photodetectors.

The second project described the effects of solar simulated light illumination and thermal stress on the stability and photophysics of cesium lead halide perovskite nanocrystals. Though the precise degradation products were not always obtained, it was observed that the halide composition dictated the stability of the materials, leading to crystal growth and photoannealing, crystalline phase transformations, and general degradation (loss of crystalline character). In addition, single crystal luminescence movies indicate the photophysics of the ON and OFF states are changing, even among samples which do not appear to degrade. In lieu of all these observations, nanocrystal surface protection via encapsulation or other methods is recommended for long-term use in functional devices.

To aid in the characterization of inorganic nanocrystals, a previously uneplored subdiffraction imaging technique was examined: the use of saturated excitation to collect subdiffraction information of inorganic quantum dot photoluminescence. By modulating

the excitation at the frequency *f* and demodulating the collected luminescence at harmonics of the fundamental (2*f*, 3*f*, etc), resolution improvements are observed. A resolution improvement of 23% was observed for luminescent quantum dots collected at 3*f*. This report showed relatively simple modifications to an inverted microscope coupled with phase-sensitive detection allows for subdiffraction information to be collected, which could be critical in the characterization of defects in nanomaterials, thin films, and even functional devices.